DOI:10.14753/SE.2020.2439

Implementation of In Silico Biomechanical Methods in Spine Surgery Innovations

Ph.D. thesis

Éltes Péter Endre M.D.

Semmelweis University

Doctoral School of Clinical Medicine.

Supervisor: Áron Lazáry, MD.,Ph.D.

Official reviewers:

Lajos Borbás, Ing. Ph.D.

Árpád Viola, MD., Ph.D.

Head of the Final Examination Committee:

László Hangody, D.Sc.

Members of the Final Examination Committee:

Gábor Skaliczki, MD., Ph.D.

István Böröcz, MD., Ph.D.

Budapest
2020

DOI:10.14753/SE.2020.2439

TABLE OF CONTENTS

DOI:10.14753/SE.2020.2439

DOI:10.14753/SE.2020.2439

DOI:10.14753/SE.2020.2439

ABBREVIATIONS

3D	three-dimensional
3DP	three-dimensional printing
ALIF	anterior lumbar interbody fusion
CAD	computer aided design
CT	computer tomography
DICOM	digital imaging and communications in medicine
DLP	digital light processing
DSI	Dice similarity index
FDM	fused deposition modeling
FE	finite element
FEA	finite element analysis
FEM	finite element method
FVM	final vertebra model
HD	Hausdorff distance
HDI	human development index
I	investigator
ICC	intraclass correlation coefficient
IDD	intervertebral disc degeneration
inf	inferior
LBP	low back pain
LLIF	lateral lumbar interbody fusion
LP	leg pain
MRI	magnetic resonance imaging
ODI	Oswestry Disability Index
OLIF	Oblique Lumbar Interbody Fusion
PACS	picture archiving and communication system
PCD	percutaneous cement discoplasty
PDF	portable document format

PMMA	polymethyl methacrylate
Postop	postoperative
Preop	preoperative
QCT	Quantitative Computed Tomography
R&D	research and development
SD	standard deviation
SF:V	surface-volume ratio
SPSS	statistical package for the social sciences
SR	surface roughness
STL	stereolithography file format
sup	superior
T	time
Th	thoracic
U3D	universal three-dimensional file format
VAS	visual analogue scale
XLIF	Extreme Lateral Interbody Fusion
ΔV	change in the spinal dimensions after PCD

DOI:10.14753/SE.2020.2439

1. INTRODUCTION

1.1. Innovation workflow

Innovation can be defined as a new idea, creative thoughts, new method, or a new device [1]. A norther perspective present innovation as the application of better solutions that meet new requirements, unarticulated needs, or existing market needs [2]. In the fields of healthcare and medicine innovation plays an important role. In the past Semmelweis by changing the gynaecologist's handwashing habits saved lives of mothers and opened a new chapter in the field of surgery [3]. Ilizarov's idea for the external fixator system has influenced the orthopaedic surgical field on both side of the Iron Curtain [4]. The technological innovations in the last decades made possible that the state of the art imaging solutions provided by Magnetic resonance imaging (MRI) or Computed tomography (CT) enables a personalised medical care [5]. Innovation is a key element in the economic development, healthcare system and it has major impact on the society as a whole, therefore the process of innovation has to be explored, and the knowledge about the innovation process has to be implemented in the graduate and postgraduate education [6].

Stanford Biodesign is one of the oldest life science programs, which focuses on training young innovators of biomedical technologies, with focus on medical devices **Figure 1**, [7]. A major distinction between the more traditional approaches to innovation and the Stanford Biodesign process is the focus on identifying and characterizing the clinical need, instead of the application of a new promising technology. The core idea of the Stanford Biodesign process is defined as "a well-characterized need is the DNA of a great invention" [8]. In my thesis I am using the workflow's (**Figure 1**) first two phases - IDENTIFY/INVENT with the 2/2 stages NEEDS FINDING-NEEDS SCREENING/ CONCEPT GENERATION-CONCEPT SCREENING - to investigate the possible implementation of the In Silico Medicine offered methods in spine surgery, based on a need defined on a global as well as on an institutional level.

DOI:10.14753/SE.2020.2439

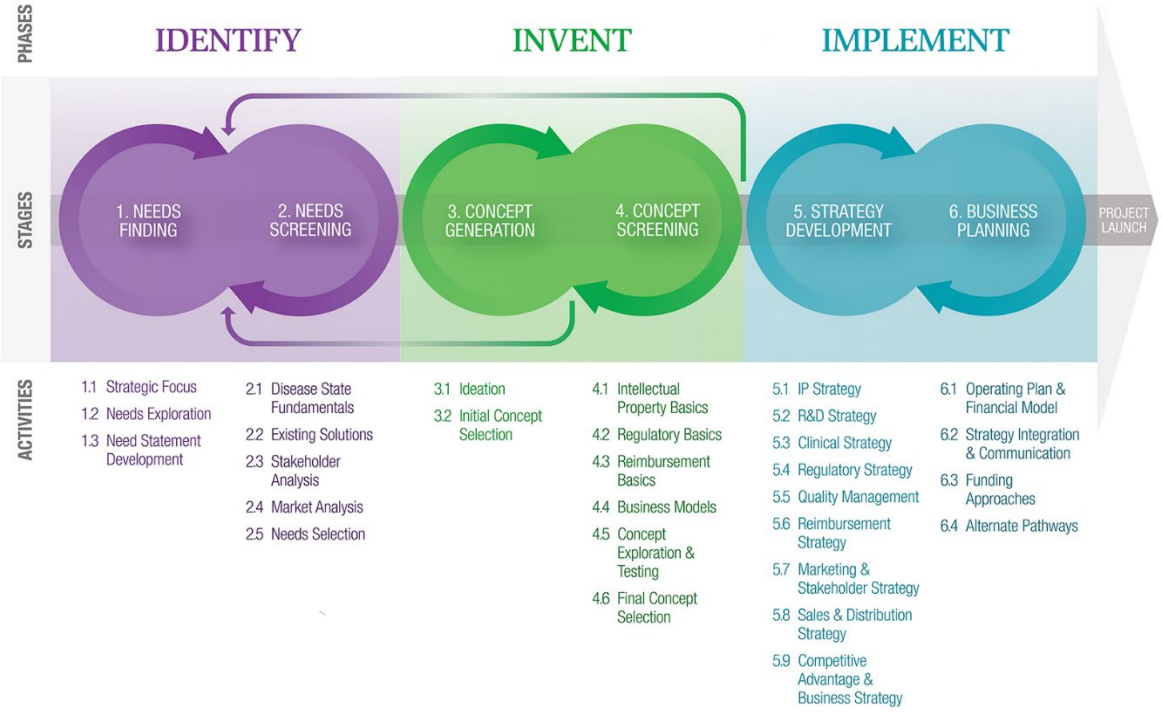

Figure 1. The Stanford Biodesign process of Innovating Medical Technologies. The process has 3 phases; identify, invent, and implement. Every phase has 2 specific stages. The iterative and cyclical process relies on research information, the information's can demand the returning to prior stages and phases. Activities performed at each stage are presented below the steps in the process. Figure from Yock, Paul G., et al. Biodesign: the process of innovating medical technologies. Cambridge University Press, 2015.

1.2. In Silico Medicine

The emergence of patient focused, holistic medicine generated new technological challenges for medicine that resulted in a new discipline, "in silico medicine". This new approach places the studying of the human body, thus the biomechanics of the musculoskeletal system into a new context. In silico medicine, including finite-element analysis (FEA) based simulation technologies and three-dimensional printing (3DP), plays a crucial role in the realization of individualized treatments, surgeries [9],[10],[11]. 3DP allows the fast, relatively cheap and accessible production of unique, complex geometries. The benefit of the patients and clinicians is based on the application of FEA simulations in pre-

surgical planning, and the preparation of surgeons aided by the 3D printed models in case of highly customized procedures [12],[13],[14],[15], [16].

The first, biomechanical application of the FEA was published by Brekelmans et al. in 1972 [17], who demonstrated that this method is suitable for analysis of stresses and strains of complex constructions such as the femur under a variety of load situations. In 2002, Fagan et al. [12] reviewed the FEA contribution to our understanding of the spine and its components and its behaviour in healthy, diseased or damaged conditions. In Fagans' conclusion the method reduces our dependence on animal and cadaveric experiments and is a valuable complement to clinical studies [12]. In 2014, Viceconti discussed the role of contemporary biomechanics in the applications and the development of the so-called Virtual Physiological Human technologies for physiology-based in silico medicine [9]. In Viceconti's vision computer models can reliably predict certain quantitative changes in health status of a given patient, based on the existing biology and physiology knowledge after it is formulated as a quantitative hypothesis, which can be expressed in mathematical terms [9]. The need for In Silico Medicine offered solutions especially 3D technologies (3D printing, virtual models, and modeling technologies such as FEA) in the field of spine surgery in a global scale has not been investigated yet.

1.3. Global perspective on the application of 3D technologies in spine surgery

New scientific and technological results or methods in the medicine cannot be widespread if the knowledge of the "end users"– spine surgeons in this case – is insufficient. So far, no study has been published about the global perspective of the need, knowledge, and acceptance of 3D technologies (3D printing, virtual models, and modeling technologies such as FEA) in spine surgery. To fill this gap, an online survey research has been conducted in the AOSpine community assessing the level of knowledge and attitude of spine surgeons about the 3D printing and modelling technologies. The global context of the results was expressed in context of the Human Development Index (HDI), an indicator of the human well-being [18], which is based on life expectancy, education and per capita income. Countries of the world are categorized into very high HDI, high HDI, medium HDI, low HDI groups, where the higher HDI shows the greater prosperity (**Figure 2**).

DOI:10.14753/SE.2020.2439

Based on our results, we have determined the information gaps and restricting factors of the development of 3D technologies, whereas the effective knowledge transfer may hold the key to widespread approval. This study serves as the NEED FINDING/NEEDS SCREENING stage in the IDENTIFY phase in the Stanford Biodesign process in my attempt to implement the in silico biomechanical methods in spine surgery innovations.

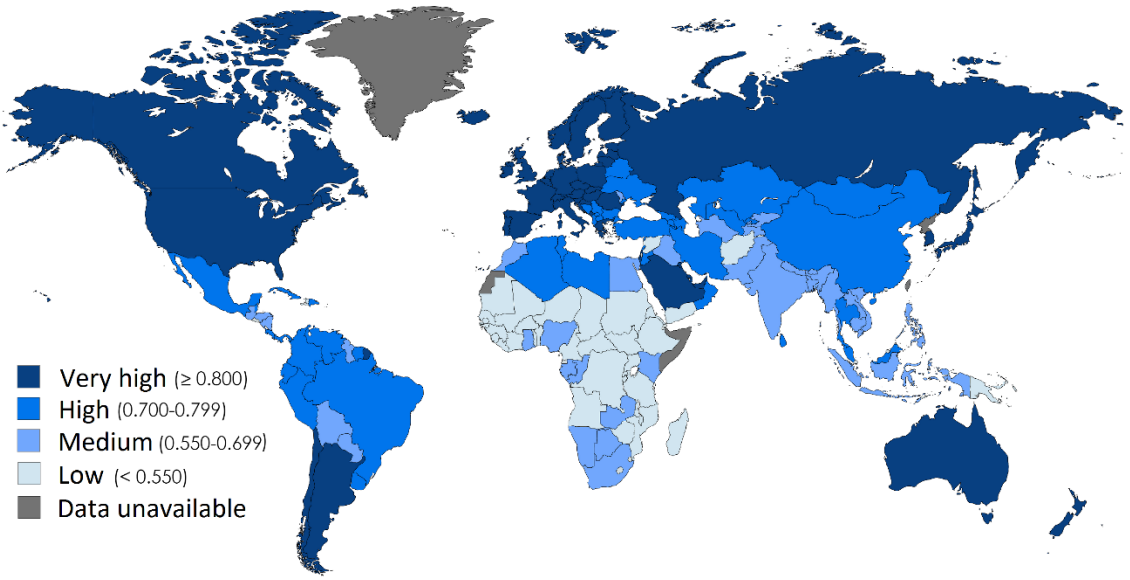

Figure 2. World map illustrates the categories of Human Development Index by country (based on 2015 and 2016 data, published on 21 March 2017 in the Human Development Report produced by the United Nations Development Program.

After the global context is defined regarding the 3D technologies, I have been investigating two surgical methods developed in the National Center for Spinal Disorders (NCSD), Budapest, Hungary, the Percutaneous cement discoplasty and the Closed Loop lumbopelvic reconstruction technic after en-bloc sacrectomy by applying research methods from the field of In Silico Medicine. The global perspective given by the survey study raised the need for strategies to implement 3D printing and FEA in cost effective way.

1.4. Percutaneous cement discoplasty effect on the spinal canal dimensions

Musculoskeletal disorders are the cause of nearly 166 million years lived with disability [19] worldwide, with low back pain and neck pain representing 69.9% of the cases [19],[20]. The incidence of such diseases is likely to increase due to population ageing; therefore, their attendance is becoming a growing burden on the healthcare system [21],[22].

The intervertebral disc degeneration (IDD) is an age-related degenerative process resulting in biomechanical and structural changes of the intervertebral discs [23]. The degree of IDD is defined by the MRI based Pfirrmann grading system [24]. The terminal disc degeneration (Pfirrmann V) is characterised by total disorganisation of the intervertebral tissue, the complete resorption of the nucleus pulposus, resulting in the vacuum phenomenon [25],[26],[27]. Intervertebral discs act as transmitting units and shock absorbers, distributing the load of body weight and muscle activity through the spinal column [28]; therefore, degeneration related structural changes will lead to biomechanical dysfunctions [29], such as segmental instability. The decreasing disc height will result in continuously decreasing spinal canal dimensions which in concert with the cyclic repetitive alternation of the foramen due to movement, lead to the development of chronic radiculopathy via compression of the nerve roots; which in turn will result in local and irradiating pain during axial loading [30]. Curative treatment of the pain requires treatment of the segmental instability; however, in elderly patients' surgical possibilities are limited due to severe comorbidities. Therefore, the minimally invasive procedures have become the preferred surgical option. Percutaneous cement discoplasty (PCD) is such a procedure, where the vacuum space in the intervertebral disc is filled out with percutaneously injected PMMA (Polymethylmethacrylate) **Figure 3**.

PCD provides a segmental stabilizing effect and indirect decompression of the neural elements due to the increase of the spinal canal dimensions. The technical details, the clinical effect and safety issues of the procedure have been previously published and the use of the technique has been also supported by a radiological prospective study [31],[32]. However, the changes in the spinal canal (central canal and neuroforamen) dimensions have not been quantified so far, because of the challenging methodological issues.

Even though the spinal canal is a complex 3D geometry, the common description of its dimensions and the evaluation of the indirect decompression effect have been based on

2D parameters (disc height, foramen height/diameter, foramen cross-sectional area, central canal diameter, central canal cross-sectional area, or segmental lordosis angle) in recent studies [33],[34],[35] which could lead to possible biases. To accurately measure the real, three-dimensional (3D) changes of the spinal canal after PCD procedure, I have aimed to develop a generalisable procedure based on patient-specific 3D computational, volumetric measurements.

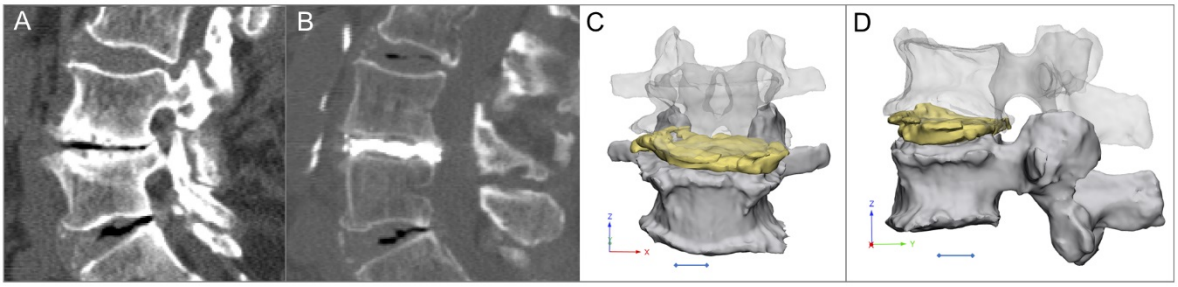

Figure 3. Percutaneous cement discoplasty, **A** Computed Tomography (CT) images (sagittal view) of a patients with advance degenerated disc (vacuum sign) LIV-LV level, **B** postoperative CT images (sagittal view) of the treated LIV-LV segment, the disc space is field with PMMA (Polymethylmethacrylate), **C**, **D** coronal and sagittal view of the LIV-LV motion segment 3D geometry (LIV vertebra transparent) with the injected PMMA geometry, scale bar=1cm

1.5. Lumbopelvic reconstruction after en-bloc sacrectomy

Sacral tumours are rare pathologies, but their management generally creates a complex medical problem [36]. Primary benign and malignant tumors of the sacrum are 2% to 4% of all primary bone neoplasms and 1% to 7% of all primary spinal tumors [37]. Most common primary sacral tumors are chordomas, representing 40% of all primary sacral neoplasms [38]. Chordoma is a malignant mesenchymal tumor with notochordal origin [39]. Surgical treatment is one of the most challenging fields in spine because of the complicated anatomy of the sacral site. In most cases, only radical surgical procedures, such as partial or total sacrectomy, can guarantee optimal local control, but several problems such as bowel, bladder and sexual dysfunction, infection, massive blood loss and spino–pelvic instability can be associated with sacral resections [40],[41]. Beyond the primary goal of the surgery

(eg. wide resection of the tumor mass), the optimal spino-pelvic reconstruction focused on biomechanical stability and soft-tissue restoration is also indispensable [42]. Several different techniques were developed for the lumbopelvic stabilization after sacropelvic tumor resection, however, long-term follow-up data and comparative studies of the different techniques are rare or still missing [43]. There is no gold standard and relatively high complication rates are reported with all reconstruction strategies [43], [44]. The ‘‘en-bloc’’ resection of a sacral chordoma by performing a total sacrectomy with soft tissue and bony reconstruction and lumbopelvic stabilization can be achieved by the ‘‘closed loop’’ technique [36],[43]. The technique uses a ‘‘U’’ shaped rod which is attached to the iliac and transpedicular screws to rebuild the spinopelvic connection (**Figure 4**). During the development of the investigated reconstruction technique the non-rigidity was a key concept in order to allow shock absorption during cyclical loading. However, the hypothesis was not tested if the construct deforms over the time. Here we aimed to develop a generalisable method based on patient-specific 3D geometries derived from CT scans in order to investigate the implant construct deformation over 6-year follow-up (FU) for a reconstruction technique.

1.6. Implementation of 3D printed physical models in spine surgery

Three-dimensional printing technologies transformed product manufacturing fundamentally [45], foreshadowing a new technological revolution [46]. Its medical utilizations, especially surgical application of 3D printed technologies aids the preoperative planning, saves time in the operating room and provides patient-specific solutions for complex cases through personalized implants [47],[48]. Besides surgical planning 3D printed physical models play a crucial role in medical education and patient communication as well, by promoting a better understanding of complex morphological changes [49],[48],[50]. However, the additional costs and time-consuming production of 3D printed physical models with current technologies are hindering its widespread use in hospitals [51].

DOI:10.14753/SE.2020.2439

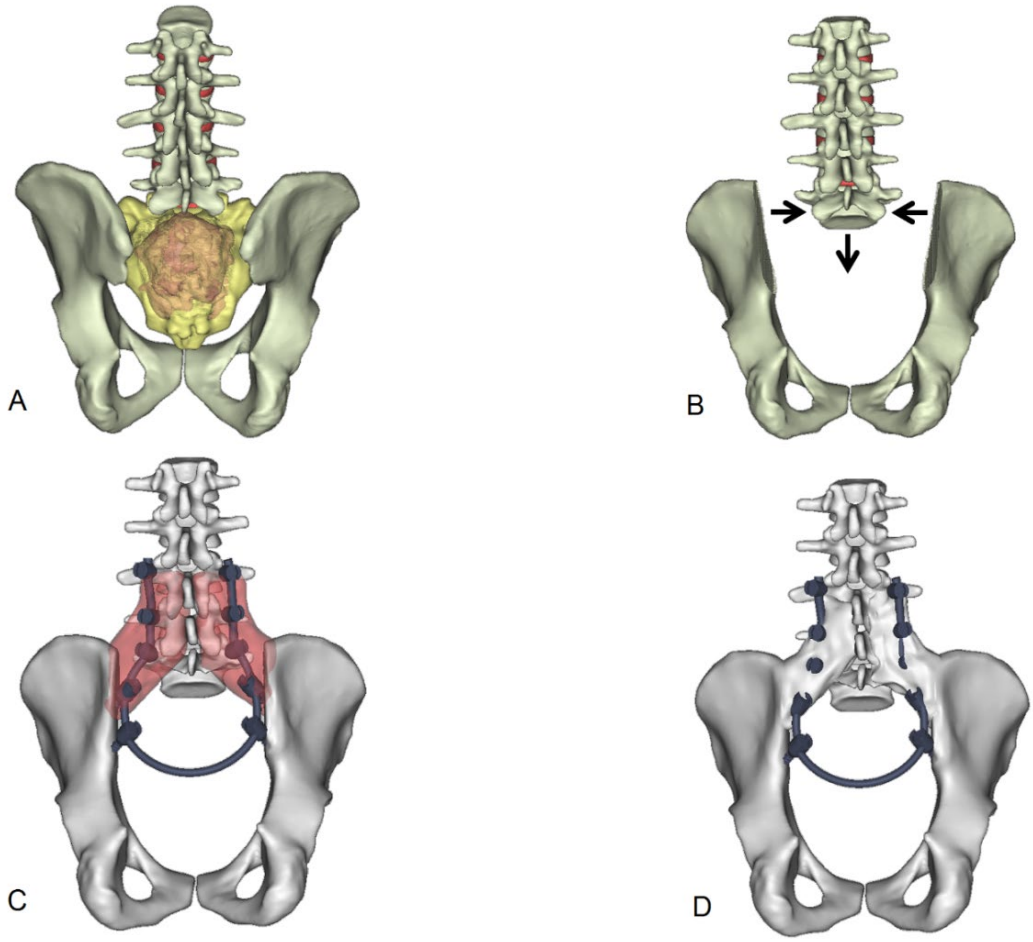

Figure 4. "Closed Loop" lumbo-sacral reconstruction technic after total en-bloc sacrectomy. **A** extended tumor mass affecting the whole sacrum. **B** geometrical change in the 3D geometry of the spino pelvic junction after en-bloc total sacrectomy. The iliac bone is cut by an oscillating saw bilaterally; the medial cortical surface of the iliac bone is left on the specimen. The lumbosacral facet joints with the intervertebral disc are removed. The dural sac (together with the cauda equina) is cut through immediately below the LV. The distance between the LV vertebra and the iliac bone is reduced (direction of the arrows). **C** in the LIII–V vertebral body and bilaterally into the iliac bones screws are inserted and connected with a single 5.5 mm diameter ''U'' form rod according to the patient's reduced (**C**) local dimensions and attached to the screws. The red areas mark the place for the artificial bone substitute, mixed with autologous bone graft. **D** the re-established connection, between the lumbar spine and the pelvis. At the side of the graft (**D**) after two years bony fusion is expected.

Moreover, there is a continuously increasing strain on healthcare providers due to global demographic shifts such as population increase, and societal change such as the rise of life expectancy [52],[53]. Therefore, the development of cost effective, sustainable strategies related to clinical application of 3DP technologies are not only highly desirable but decisive.

Currently, there is an increasing interest in the healthcare market of commercial 3D printing services [54], each providing 3D printers with different technologies and technical parameters at a widely differing price-range. The clinician and the hospital management face the decision of choosing one of these services and are confronted with the task of implementing it with the available resources. However, evidence-based reports which can potentially offer guidance on these issues are absent in the literature.

In my thesis I present a method to compare the geometrical accuracy of two 3D printing technologies for printing spine physical models. Advantages and disadvantages were weight up in an entry level technology (cost effective, most affordable) with a higher category technology (more precise, more expensive). We also reveal an institutional strategy of the application of 3D printed physical models by presenting a clinical case, where a model printed with the entry level technology was used in the preoperative planning.

1.7. 3D printed patient-specific surgical guide for spine surgical navigation

Spinal fixation is a routine procedure for the treatment of unstable spine due to trauma, congenital malformations, degenerative diseases, and tumours [55]. The accurate placement of screws in the spine is challenging, given the risk of damage to neighbouring anatomical structures (spinal cord, nerve roots, arteries, veins) [2], [57]. Computer-assisted surgery (CAS) has been adopted as a safe and accurate guiding system for the placement of pedicle and lateral mass screws in the spine [58]. CAS navigation systems use optical tracking via infrared cameras incorporating 3D geometries from pre-operative CT scans or in combination with fluoroscopy-based imaging [59], [60] or intraoperative CT scans [61]. Optimal registration of the spine geometry to the navigational instruments is crucial for precise screw insertion. During surgery it is often required to perform intraoperative CT scans or to use fluoroscopy to re-register the system [59], [60], [61]. Surgical manipulation after

obtaining the intraoperative CT or fluoroscopy images may cause CAS registration errors, which can result in screw malposition. This phenomenon cannot be completely excluded even with state of the art intraoperative CT technology [61]. 3D printed patient-specific surgical navigation templates are accurate [62], [63], decrease surgical time, reduce intraoperative x-ray exposure [64] and can be more accessible compared to traditional CT or fluoroscopy-based systems [65], [66]. The decline in the costs of 3D printing technology is expected to continue due to its continuous and fast development [67], [68], [69]. However, in less developed areas of the world, where complex spinal deformity is relatively common and advanced CAS technology is not available [64], [70] 3D printed templates are still not as widely implemented in the clinical practice, as it would be desirable.

Revision surgeries are challenging especially if an implant related failure is complicating the clinical situation. The lumbo-sacral area has a special local anatomy. In the S1 segment the convergent bicortical screw trajectory provides a superior anchoring compared to any other directories, but the proper insertion of the new screws in a revision surgery can be impossible without surgical navigation. In my thesis, I am representing a case who has raised the clinical need for the development of a computer-aided design (CAD) and finite-element analysis (FEA) combined method for affordable spine surgical navigation with 3D printed customized drill guide.

DOI:10.14753/SE.2020.2439

2. OBJECTIVES

The general aim of my PhD work is to investigate the implementation of In Silico Biomechanical Methods in Spine Surgery Innovations.

In the first part of my PhD thesis, I pursue to answer the question of what determines the acceptance rate and the factors which stand against the wider spread of the 3D technologies in spine surgery (Eltes et al., 2019). For this purpose, I specifically addressed the following questions in a survey-based study in five thematic chapter:

1. What is the demographic of the respondents (country of residence, details of spine surgical practice, basic knowledge of 3D technologies)?
2. Personal use of 3D printed or virtual 3D models
3. Use and attitude towards 3D technologies in surgical navigation
4. Use and attitude towards the advanced manufactured (3DP) and patient-specific implants
5. What is the future and limitations of the 3D technologies in spine surgery?

Investigation of these problems defined a global context regarding 3D technologies. Therefore, in the second and third part of my PhD work, I have been studied two surgical methods developed in the NCSD the PCD and the Closed Loop lumbopelvic reconstruction technique.

In part two, I aimed to develop a generalizable procedure based on patient-specific 3D computational, volumetric measurements to evaluate the geometrical change of the spinal canal after PCD treatment. For this, the following specific questions have been asked:

1. How can the complex 3D geometry of the spinal canal be defined?
2. How can the geometrical change in the spinal canal due to PCD be measured?
3. How reliable and repeatable is the developed method?
4. What is the relationship between the PCD induced volumetric change in the spinal canal and the PMMA volume, surface and surface-volume ratio?
5. What is the relationship between the PCD induced volumetric change and the clinical outcome of the patients?

In part three, I aimed to develop a generalizable method based on patient-specific 3D geometries derived from CT scans in order to investigate the implant construct deformation over 6-year follow-up (FU) for a patient who underwent sacrectomy and Closed Loop reconstruction. The following specific questions were addressed:

1. How can we define the complex 3D geometry of the implant construct and the pelvic bone?
2. How can we measure the deformation of the implant construct over the FU?
3. How can we map the bony fusion process?
4. How reliable and repeatable is the developed method?
5. What is the relationship between the postoperative days and the implant construct deformation in the three anatomical planes (coronal, sagittal, axial)?

The global perspective on the attitude of the spine surgeons towards the application of 3D technologies given by the survey study raises the need for strategies to implement 3D printing and FEA in the clinical environment in an affordable way. Part four of my thesis addresses the need for the application of affordable 3D printing technology for spine physical models (Eltes et al., 2020). Here, I developed an institutional strategy for application of the 3D printed physical models and I addressed the following specific questions:

1. How can we create an accurate 3D virtual model of the patient-specific spine?
2. How can we evaluate the geometrical accuracy of a 3D printing technology?
3. Can an affordable printing technology provide accurate 3D spine physical model compared to a more expensive, more accurate printing technology?
4. Can we implement the patient specific virtual models in the clinical communication?
5. How can we use a patient-specific physical model in presurgical planning?

Part five of my thesis addresses the clinical need for the development of computer-aided design (CAD) and finite-element analysis (FEA) combined method for affordable spine surgical navigation with a 3D printed customized drill guide to allow safe pedicle screw insertion in challenging situations. For this, I asked the following specific questions:

1. How can we provide a patient-specific surgical guide in the case of revision surgery, where a broken SI screw creates a challenging geometrical situation for a new screw insertion?
2. Can we evaluate and integrate the local bone biomechanical properties for the screw insertion and for the guide design?
3. Can we reduce the finite element model running time and preserve reliable results?
4. How can we manufacture the guide in a cost-efficient way?
5. How can we test the accuracy of the guide before surgery without cadaveric models?

Contributions:

In my thesis in parts I, II, III, IV, V the research design, acquisition of data, analysis and interpretation of data, and writing the manuscripts for publications based on the Parts (I-V) was done by myself under the guidance of Áron Lazáry. However, in the following paragraph I specify the detailed contribution of my co-workers in the different Parts.

In PART II. of my thesis László Kiss was the second investigator (I_2). Máté Turbucz was the second Investigator (I_2) in PART III., and Jennifer Fayad the third investigator (I_3). Jennifer Fayad processed the data of the gait analysis and prepared **Figure 34**. In PART IV. Vivien Leskó was the second investigator (I_2). Tibor Csákány integrated the 3DPDF files containing the virtual patient-specific models in the internal institutional database. Benjámin Hajnal in PART V., created the visualization for the proposed surgical technique summarized in **Figure 48**.

DOI:10.14753/SE.2020.2439

3. MATERIALS AND METHODS

3.1. PART I. Clinical needs finding for 3D technologies, a survey of AOSpine members

In October 2016, an online survey (**Table 1**.) was sent out a single time to all AOSpine members on the mailing list.

Table 1. Survey about the attitude of AOSpine members towards 3D technologies in spine surgery

Chapter I. Demographics of survey respondents
1. Years of experience in spine surgery
0-3y
3-10y
10-20y
more than 20y
2. Country of residence
3. Your common practice in spine surgery*
degenerative
deformity
tumor
trauma
4. What percentage of your cases are complex, challenging surgeries?
0-20%
20-40%
40-60%
more than 60%
5. Practice where you do spine surgeries
public
private
both
6. Are you familiar with the concept and the benefits of 3D printing/modelling technologies?
I don't have any specific knowledge
I have some general information from news, advertisements
I have read scientific papers/conference talks in the topic
I have already used some of these technologies
Chapter II. 3D simulation and printing options (3D models of the different pathologies and treatments) can help education, surgical planning and development of new surgical methods.
1. Have you ever used any 3D technology for education (or demonstration) for medical students, residents, colleagues?
never

occasionally, 3D virtual models
occasionally, 3D printed models
frequently, 3D virtual or printed models
2. Have you ever used 3D virtual models or printed models for surgical planning or for the development of a surgical technique (e.g. by demonstrating the difficult anatomical situation or the challenging surgical steps)?
never
occasionally
frequently
other (please specify)
3. What is the main barrier of the frequent use of such techniques in your clinical/educational practice? *
no or limited knowledge about the possibilities and requirements
no or limited access to 3D modelling software
no or limited access to 3D printing
costs of 3D modelling/printing
I am not interested in these technologies
Chapter III. 3D modelling/printing can be used to produce patient- and condition specific surgical navigation guides, particular instruments to improve the safety and efficacy of challenging procedures (resections, osteotomies, difficult screw insertion etc).
1. Intraoperative 3D navigation systems can reduce the complications and the morbidity of spinal surgeries. Do you use any 3D navigation system or tool in your clinical practice?*
not at all
occasionally (CT or fluoro based system)
regularly (CT or fluoro based system)
occasionally (3D printed surgical guide)
regularly (3D printed surgical guide)
2. If not what is the reason?*
lack of knowledge
high purchasing price
high maintaining costs
too complicated use (longer surgery, need of a technician, etc)
lack of confidence
I do not see its necessity in my practice
other:
3. If you use any 3D navigation or if you would have the possibility of use, how many percentages of your surgeries would you use the technology in?
<10%
10-25%
25-50%
>50%

4. Have you ever experienced or felt that a specific, unique surgical instrument (e.g. a particular chisel, courette or screwdriver) would have helped the surgery?
no
occasionally
frequently
5. What do you think about the acceptable cost of a unique, 3D printed surgical instrument in your country and clinical setting?
less than 10% of the direct cost of the surgery
no more than twice of a similar, but traditional product
comparable to the cost of a pedicle screw
significant extra cost is acceptable
Chapter IV. 3D modelling and printing technologies can help to develop the next generations of spinal implants. Advanced manufactured general (eg. porous) and patient-specific implants can have a significant role in the future personalized medicine.
1. Have you ever used any advanced manufactured (3D printed) implant?
never
occasionally
frequently
2. Where do you see the possible advantage of the use of advanced manufactured implants?
all implanted surgeries because a general or patient-specific advanced manufactured implant can provide better
clinical outcome even in case of a standard pathology
challenging surgeries (e.g. tumor resection) and compromised anatomy or biology
only in complex cases where patient-specific implant would be required
none of the spinal surgeries
3. What do you think how many of your cases could benefit from the use of advanced manufactured (3D printed general or patient-specific) implants?
<10%
10-25%
25-50%
>50%
other (please specify)
4. How do you see what is the main barrier of the spreading of advanced manufactured (3D printed) implants?*
limited knowledge about the possibilities among the surgeons
limited access to 3D modelling and/or printing solutions
high cost of modelling/printing
unclear regulations
lack of confidence, limited evidence

5. What do you think about the acceptable cost of an advanced manufactured implant in your country and clinical setting?
same as a traditional implant
no more than twice of traditional implants
high cost is acceptable because of the personalized approach
a significant extra cost is acceptable because a 3D printed implant can provide better clinical outcome
an advanced manufactured implant can reduce the total cost of the surgery at least in selected cases
Chapter V. General impression
1. What do you think about the role of 3D printing/modelling technologies in spinal surgery?
no real future – too complicated and expensive
an option only for very limited applications, individual cases
a promising, feasible option for the near future
revolutionary
other (please specify)
2. What do you think what are the main barriers of the spreading of 3D printing/modelling technologies?*
"distance" between engineers and surgeons
"distance" between the hospital and the printing/designing facility
surgeons are not aware of the possibilities provided by 3D printing/modelling
expensive technology
market are full with traditional solutions
surgeons are not motivated to use advanced manufactured implants
process of a patient-specific surgery is time-consuming
3. Other specific comments:

*Note: multiple choice

The survey was open for two months and a single answer was permitted per email address. The questionnaire included 21 multiple choice or ordinal scale questions, being divided on thematic chapters (one page each) as follows: (I.) question I/1-6 we collected demographic data of the respondents (country of residence, details of spine surgical practice, basic knowledge of 3D technologies); (II.) questions II/1-3 focused on the personal use of 3D printed or virtual 3D models; (III.) questions III/1-5 focused on the use and attitude towards 3D technologies in surgical navigation; (IV.) questions IV/1-5 investigated the advanced manufactured (3DP) and patient-specific implants; in chapter (V.) we raise questions V/1-2 about the future and limitations of 3D technologies. Answers to ordinal scale questions (I/6, II/1, II/2, III/1, III/4, IV/1, IV/2, V/1) have been scored with the summed score (range: 0-28)

representing the plausible level of acceptance (acceptance score) of 3D technologies in spine surgery. The influence of geographical location (AOSpine region), spine surgical practice, experience, etc. on the acceptance score was analyzed statistically. Participants of our survey were grouped based on the HDI of their country of residence and survey results were analyzed in the context of this parameter too.

3.1.2 Statistical analysis

For statistical analyses, Spearman correlation, non-parametric tests, and Chi-square tests were applied depending on the distribution of the variables. Statistical tests were performed using SPSS and $p<0.05$ was considered as significant.

3.2. PART II. A novel method for patient-specific computational analysis of three-dimensional changes in spinal canal dimensions after percutaneous cement discoplasty

3.2.1. Clinical cohort and CT scan acquisition

We performed a retrospective analysis of prospectively collected data. The study was approved by the National Ethics Committee of Hungary, the National Institute of Pharmacy and Nutrition (reference number: OGYÉI/163-4/2019). Informed consent was obtained from all participants.

The cohort consisted of 10 patients (74 ± 7.7 years old), who underwent primary single or multilevel PCD (16 motion segments in total) at a tertiary care spine referral centre (**Table 2**). All presented operative procedures were performed by a single surgeon (GJ). Preoperative (preop), and postoperative (postop) 6-month follow-up results were collected and analysed using the patient- reported outcome questionnaire Oswestry Disability Index (ODI) and with visual analogue scale (VAS) for leg pain (LP) and low back pain (LBP).
Quantitative Computed Tomography (QCT) scans were performed pre- and postoperatively, with a Hitachi Presto CT machine using an in-line calibration phantom, and a protocol previously defined in the MySpine project (ICT-2009.5.3 VPH, Project ID: 269909) with an intensity of 225mA and voltage of 120kV [71], [72]. Images were reconstructed with a voxel size of 0.6x0.6x0.6 mm^3. Based on the QCT images, Hounsfield Units can be converted into bone mineral density (BMD) equivalent values, necessary for creating finite element (FE)

models. In this study the QCT images were used as conventional CT images without any conversion.

The data were exported from the hospital PACS in DICOM file format. To comply with the ethical approval the patient data protection, anonymization of the DICOM data was performed using the freely available Clinical Trial Processor software (Radiological Society of North America, https://www.rsna.org/ctp.aspx) [73].

Table 2: Clinical cohort

N=10	Patient ID	Age (years)	Gender	Treated segment
	P01	83	M	L4-L5
	P02	59	F	L2-L3 L3-L4 L4-L5
	P03	67	M	L5-S1
	P04	78	F	L3-L4
	P05	79	M	L5-S1
	P06	76	F	L1-L2
	P07	75	F	L2-L3 L3-L4 L4-L5
	P08	66	M	L3-L4 L4-L5
	P09	77	F	Th12-L1 L1-L2
	P10	82	F	L1-L2

3.2.2. Definition of pre- and postop motion segments' 3D geometry

In order to establish the 3D vertebral geometry of the pre- and postop motion segments and the injected polymethyl methacrylate (PMMA) geometry, a segmentation process was performed on the 2D CT images [74]. For this, the thresholding algorithm and manual segmentation tools (erase, paint, fill etc.) in Mimics® image analysis software

(Mimics Research, Mimics Innovation Suite v21.0, Materialise, Leuven, Belgium) were used. (**Figure 5**).

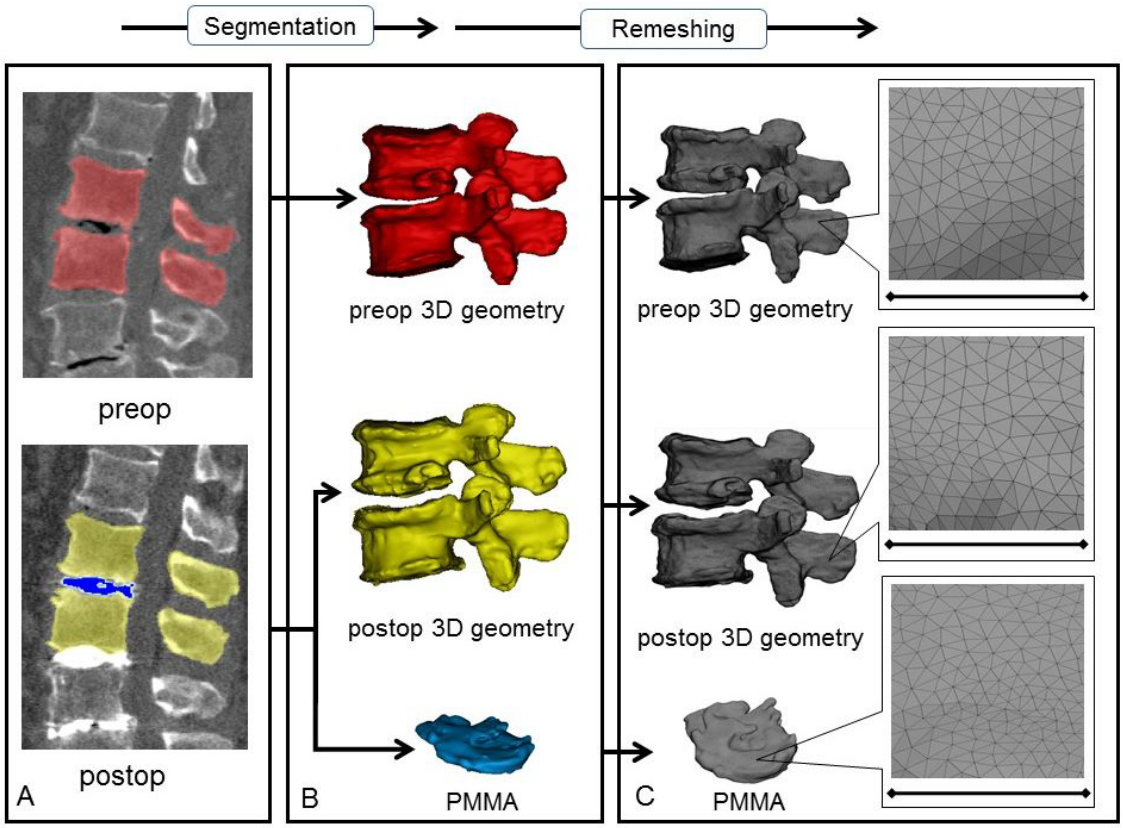

Figure 5. 3D geometry definition of pre- and postop motion segment geometries and of the injected PMMA geometry. **A** during the segmentation process the bone volume is first separated from the surrounding soft tissue by thresholding of the Hounsfield units' levels of the 2D CT images (sagittal view). The resulting colored mask (preop, red; postop, yellow) voxels represent the 3D volume of the vertebra, and the blue voxels the PMMA, respectively. **B** from the mask, a triangulated surface mesh is generated, and a smoothing is applied (iteration: 6, smooth factor: 0.7, with shrinkage compensation). **C** uniform remeshing process was applied (target triangle edge length 0.6 mm, sharp edge preservation, sharp edge angle 60°). Scale bar length 5mm.

During the segmentation process the bone volume was first separated from the surrounding soft tissue by thresholding of the Hounsfield units' levels. The resulting masks (group of voxels) where homogenously filled by preserving the outer contour of the geometrical border in 2D. From the mask, a triangulated surface mesh was automatically generated. On the 3D geometries surface smoothing was applied (iteration: 6, smooth factor: 0,7, with shrinkage compensation). Furthermore, uniform remeshing process was applied (target triangle edge length 0.6 mm, sharp edge preservation, sharp edge angle 60°) for all the vertebra and PMMA geometries. To evaluate the accuracy of the segmentation process, we calculated the Dice Similarity Index (DSI) [75, 76]. The DSI quantifies the relative volume overlap between two segmentation procedures as follows: $DSI=(2\cdot V(I_1 \cap I_2))/(V(I_1)+V(I_2))$, V is the volume of the voxels inside the binary mask (number of voxels multiplied with the voxel size; in mm^3), and I_1 and I_2 are the binary masks from two segmentation processes (performed by two investigators (I), 1 and 2). The DSI values range between 0 ± 1, one denoting a perfect match. The vertebral geometry segmentation accuracy was evaluated by random selection of 6 preoperative and 6 postoperative vertebral geometries (Microsoft Office Professional Plus 2016, Excel, RANDBETWEEN function). All 12 vertebras were segmented by a second investigator (I_2) and the second segmentation was compared to I_1 after which the DSI was defined. The PMMA segmentation evaluation was done by repeating all the 16 measurements by I_2 and then the DSI was calculated.

3.2.3. Alignment of the motion segments' geometry

To detect the PCD induced changes in the postop motion segment, the pre- and postop vertebral geometries were aligned in the same coordinate system. For this, preop 3D data sets were transposed into the same coordinate system with the postoperative data. Pre- and postop caudal vertebra surface mesh models of the treated motion segments were used as reference geometry (**Figure 6**).

DOI:10.14753/SE.2020.2439

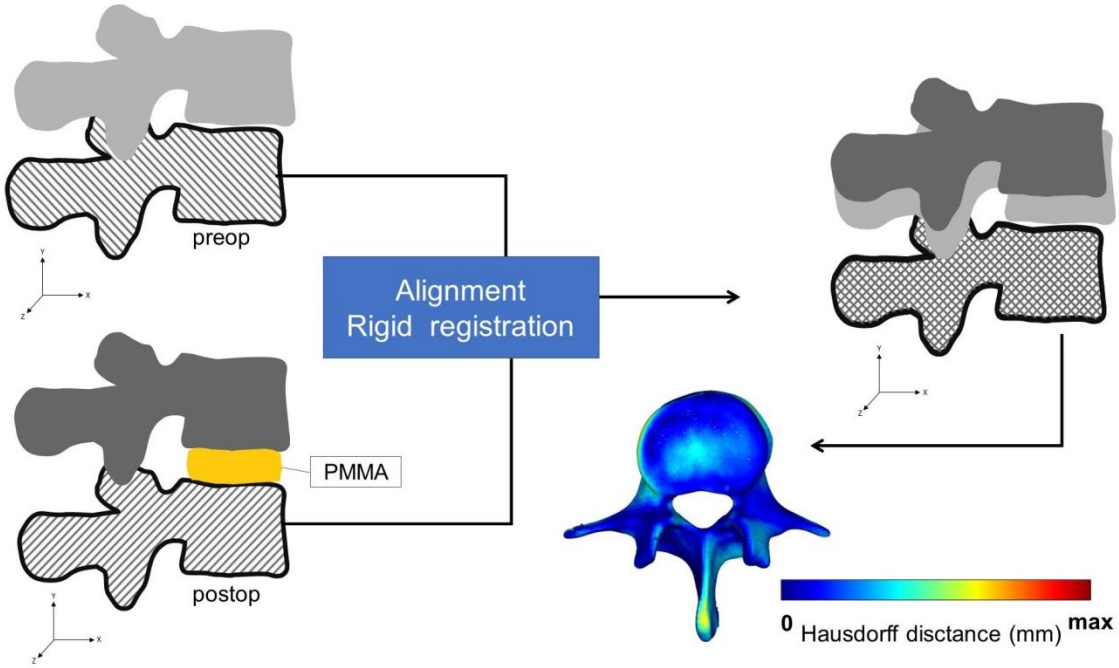

Figure 6. Alignment of the preop motion segment vertebral geometry to the postop geometry. The alignment of the caudal vertebra was performed using control points (as shown in **Figure 7**) and rigid surface registration algorithms were applied. The process created a common coordinate system for the preop and postop motion segments with nearly identical boundaries for the caudal vertebras. The Hausdorff Distance was used as a quality measure for the alignment process at the caudal vertebra.

A control points based rigid registration algorithm was used via Mimics® software. The 18 control points corresponded to easily identifiable anatomical landmarks at the caudal vertebra or sacrum (**Figure 7**).

To evaluate the accuracy of the registration and alignment procedure the Hausdorff Distance (HD) was measured with the MeshLab1.3.2 software [77] (an open source free software: http://www.meshlab.net) Metro tool [78] (**Figure 6**) at the level of the aligned caudal preop and postop vertebras. The HD represents the maximum distance between two points (triangle vertex) of two sets, both from corresponding sections of the meshes (i.e.: the HD is expected to be equal to zero in case of a perfect alignment of absolute symmetrical geometries, whereas values >0 provide the actual distance between the two surfaces).

DOI:10.14753/SE.2020.2439

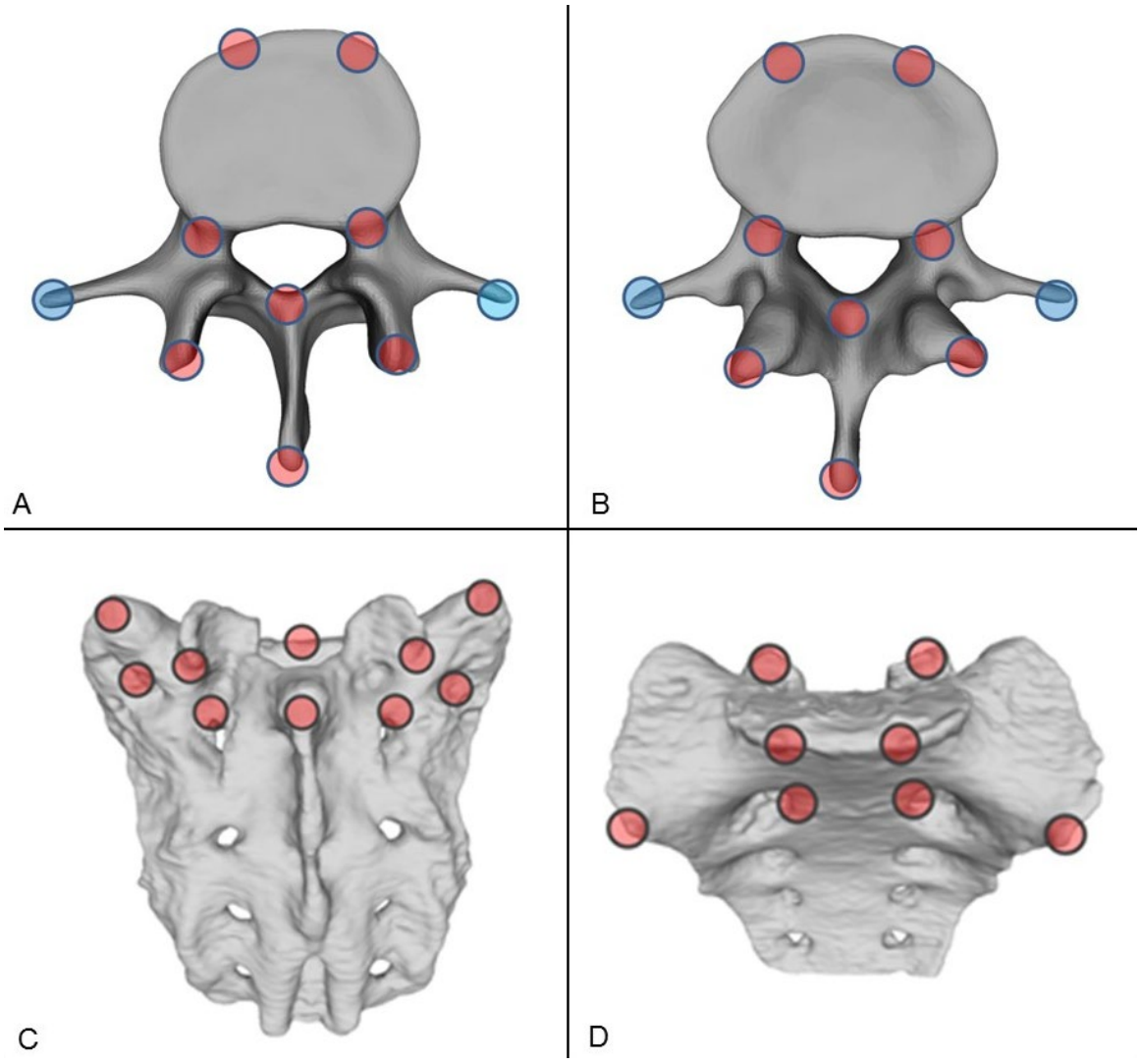

Figure 7. Selection of control points for rigid surface registration. Ten control points were selected from the superior (**A**) and eight from the inferior (**B**) reference regions of the vertebra and from the aligned geometry, respectively. For the sacrum ten control points were selected from the superior-dorsal (**C**) and eight from the superior-ventral (**D**) regions of the reference and from the aligned geometry, respectively. The filled red circles represent the selection areas of the registration points, the filled blue circles represent common selection areas for two different regions.

The HD values were calculated at the vertices of the triangulated surface meshes as follows: $h(A,B) = max_{a\epsilon A}\{min_{b\epsilon B}\{d(a,b)\}\}$; where *A* is the postop mesh; *B* is the preop reference mesh; *a* and *b* are points of sets *A* and *B* respectively, and *d(a, b)* is the Euclidean metric between these points. The alignment of the pre and postop motion segments was performed by two investigators (I_1, I_2) and two aligned datasets were created with 16-16 motion segments each. The HD measurements where performed for all the 16 registered motion segments for both investigators.

3.2.4. Measurement of the neuroforaminal 3D geometry

After alignment, the change in spinal canal geometry, induced by the injected PMMA in the intervertebral space during the PCD procedure, was defined for the two datasets (aligned by I_1, I_2). A measurement cylinder was created using Mimics® software analyse module. The cylinder was inserted in the virtual coronal axis of the neuroforamens (coronal plane). Its length was defined at 90 mm, while the radius of the cylinder was set by the investigators uniquely in each patient and segment (**Table 4**) in a way to fill the neuroforamens' volumes and the central canal in pre- and postop 3D geometries of the motion segments (**Figure 8**).

The overlapping volumes between the cylinder and the motion segment 3D geometry were subtracted (Boolean operation/Minus). The change in the subtracted cylinder volumes represents the spinal canal dimension Vpreop= 3D Cylinder– (3D Cylinder- Preop 3D motion segment), and Vpostop= 3D Cylinder– (3D Cylinder- Postop 3D motion segment). The change in the subtracted cylinder volumes represents the indirect decompression effect of the surgical procedure and it is defined as ΔV (ΔV = Vpostop - Vpreop) (**Figure 8**). To determine the repeatability and accuracy of the measurements, intra an inter-rather reliability analysis of the two Investigators (I_1, I_2) at two different time points (T_1, T_2) was determined (see Statistical analysis).

DOI:10.14753/SE.2020.2439

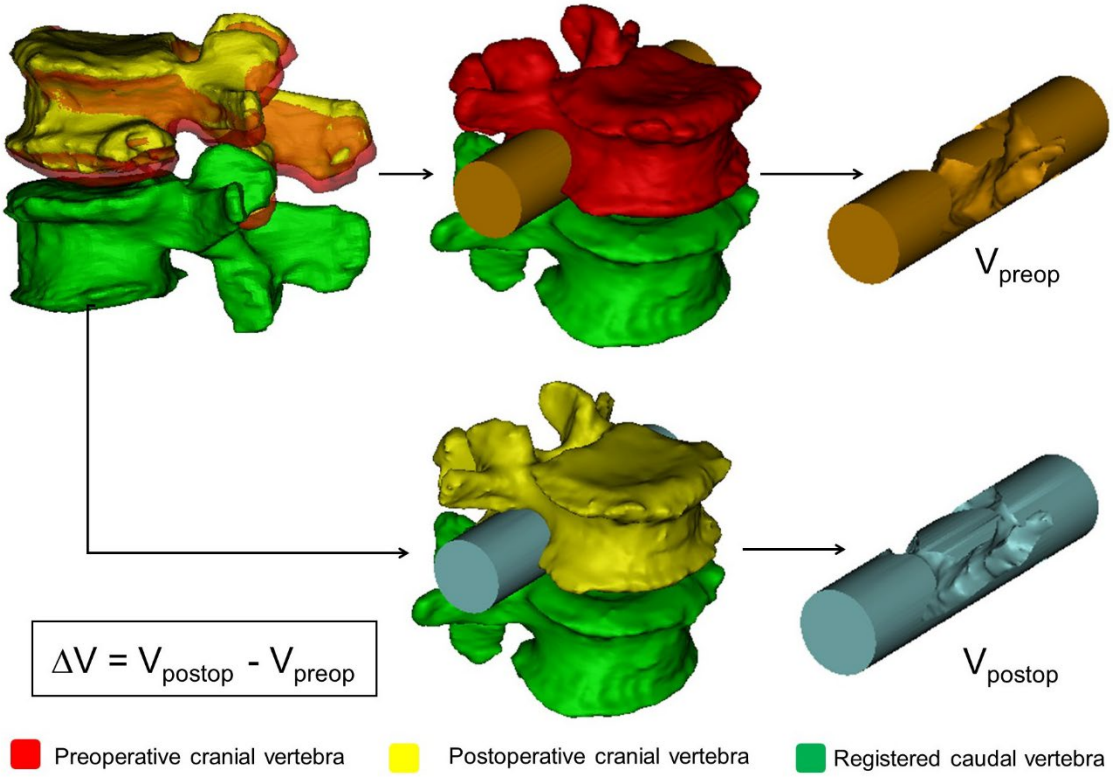

Figure 8. Measurement of the change in the neuroforaminal geometry induced by the PCD. After alignment, the pre- and postoperative motion segments shared a common caudal vertebra. The cranial vertebra geometrical position has changed due to the lifting effect of the PMMA. Two identical cylinders were introduced in the neuroforaminal and central canal regions of the pre- and postop. motion segments. Vpreop and Vpostop represent the subtraction of the overlapping vertebral geometry from the initial cylinder geometry. The indirect decompression effect of the PCD is defined as ΔV (ΔV = Vpostop - Vpreop).

3.2.5. PMMA geometry visualisation and thickness measurement

The 3D geometry of the intervertebral PMMA for the 16 treated motion segments were defined during the segmentation process by a uniformly remeshed triangulated surface mesh (**Figure 5**). The surface mesh defines the geometry and determines the surface and the volume of the object. In 3-matic® software (Mimics Innovation Suite v21.0, Materialise, Leuven, Belgium) thickness measurement was performed and visualised using contour plots.

The thickness was defined at the level of every triangle element of the surface mesh as the perpendicular distance from the element midpoint to the other wall (surface) off the geometry.

3.2.6. Statistical analysis

The data management was performed in Microsoft Office Professional Plus 2016 (Microsoft, Redmond, Washington, United States). All statistical tests were performed with SPSS statistical package version 23 (SPSS Inc, Chicago, IL). Due to small sample size, normality test of the data is expected to have little power, thus we opted to apply non-parametric tests. The HD measurements cumulative probability plots (Supplementary Fig.2) were created with SigmaPlot 12 (SSI, San Jose, California, United States). Inter-rater (I_1 vs I_2) reliability was determined by Intraclass Correlation Coefficient (ICC) estimates and their 95% confident intervals (CI) were calculated based on a mean-rating (k = 2), absolute-agreement, 2-way mixed-effects model. Intra-rater (I_1T_1 vs I_1T_2, I_2T_1 vs I_2T_2) reliability was determined by ICC estimates and their 95% confident intervals were calculated based on a single measurement, absolute-agreement, 2-way mixed-effects model. The statistical difference in the change of spinal canal volume, ODI, LP and LBP pre-, and postop was assessed by Paired Sample Wilcoxon signed ranked test ($p \leq 0.05$, **Figure 32**). The relationships between the PMMA and the mean volumetric change (ΔV); PMMA surface and ΔV; PMMA surface-volume ratio and ΔV were defined using the Spearman's rank correlation (**Figure 33**). The relationships between the ΔODI (preop – postop) and the ΔV; ΔLP (preop – postop) and the ΔV, ΔLBP (preop – postop) and the ΔV were defined using the Spearman's rank correlation (**Figure 33**).

3.3. PART III. A novel computational method to assess implant deformation and to map bony fusion in a lumbopelvic reconstruction after en-bloc sacrectomy

3.3.1. Clinical Case

The patient (**Figure 9)** case and surgery was presented at the European Spine Journal, *Open Operating Theatre* (OOT) platform [79], [80]. The 42-year-old male patient had mild and non-specific low back pain for 4–5 years. He had experienced minor problems with

defecation and urination for 1 year and a palpable lump had been observed for some months in the sacral region. The neurological examination showed normal motor and sphincter function but a mild hypaesthesia in the perianal region. Radiological examinations revealed an extended tumor mass affecting the whole sacrum with significant soft tissue extension to the retroperitoneum and cranially involving the paravertebral muscles as far as the LIII spinal level on the right side (**Figure 9**). Open biopsy procedure based Histological examination reweld the diagnosis of chordoma. Total ‘‘en-bloc’’ sacrectomy combined with soft tissue and bony reconstruction together with lumbopelvic stabilization (‘‘closed loop’’ technique) was performed to remove the tumor. Artificial bone substitute (ACTIFUSE®) was placed between the LV body and the iliac crest bilaterally after refreshing and preparing well bleeding spongious bony host surfaces (**Figure 4C**). The large defect of the body wall between the LV vertebral body and the coccygeal ligamentous complex was covered by Dacron mesh (anchored to the bony landmarks: LV vertebral body, tuber ossis ischii and iliac bone). Finally, the wound closure was performed by creating bilaterally m. gluteus maximus rotatory flaps.

3.3.2. Postoperative Computed Tomography scan acquisition

We performed a retrospective analysis of retrospectively collected postoperative (postop) Computed Tomography (CT) data. The study was approved by the National Ethics Committee of Hungary, the National Institute of Pharmacy and Nutrition (reference number: OGYÉI/163-4/2019). Informed consent was obtained from the participant. The data set consisted of 12 CT covering a 6-year follow-up period (FU) (**Table 3)**. The CT scans were performed with the same CT machine (Hitachi Presto, Hitachi Medical Corporation, Tokyo, Japan) with an intensity of 225mA and voltage of 120kV. The data were exported from the hospital PACS in DICOM file format. To comply with the ethical approval the patient data protection, deidentification of the DICOM data was performed using the freely available Clinical Trial Processor software (Radiological Society of North America, https://www.rsna.org/ctp.aspx) [73].

DOI:10.14753/SE.2020.2439

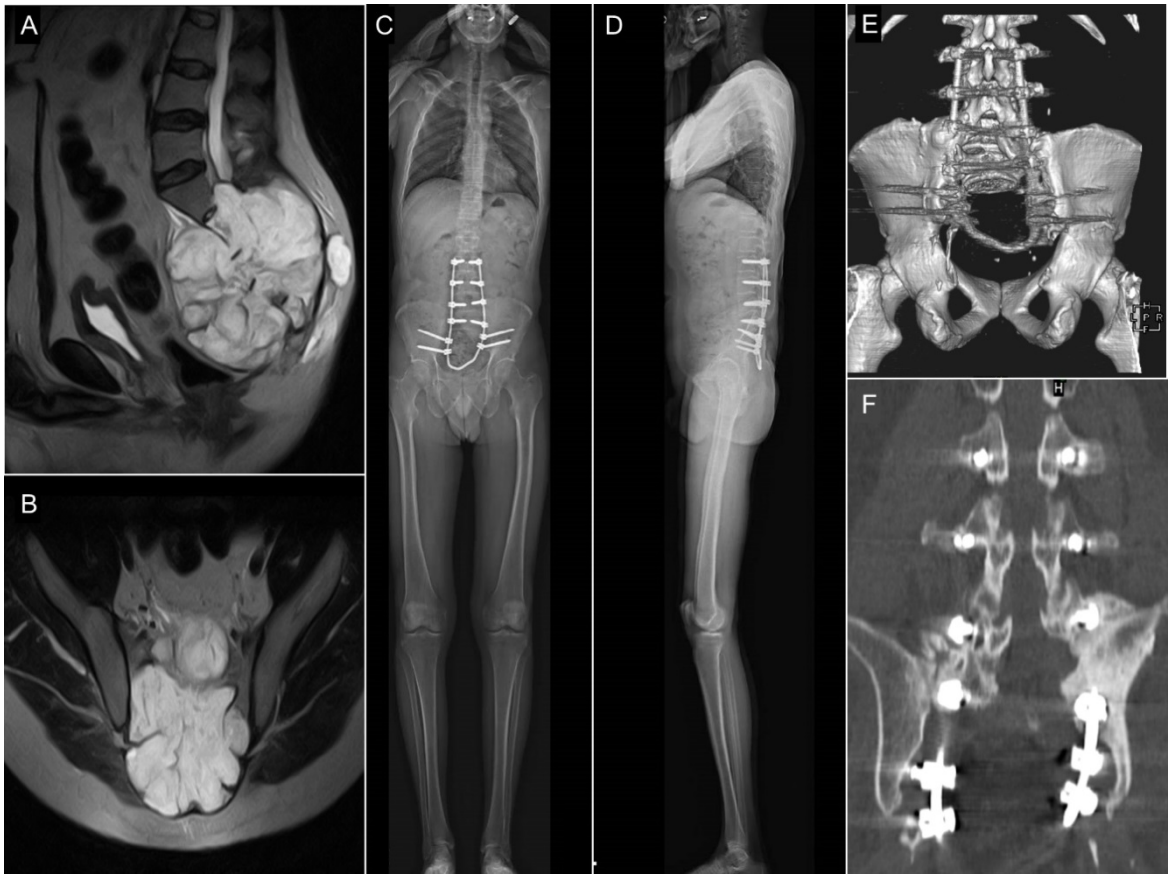

Figure 9. Pre- and postop imaging of a 42 years old male patient how underwent total en-block sacrectomy and received a Closed Loop spinopelvic reconstruction. **A, B** preop T2, MRI images of a large sacral chordoma (**A** sagittal, **B** axial plane) The extended tumor mass effected the whole sacrum with significant soft tissue extension to the retroperitoneum and cranially involving the paravertebral muscles. **C, D** Standing X-ray images of the patient at 6 month FU (**C** sagittal, **B** coronal plane). **E**, **F** CT scan at 24 month CT images, signs of bony fusion are visible between the L.IV,V vertebra and the iliac bone (**E** posterior view of the 3D rendered CT images, **F** coronal view at the fusion site)

Table 3. Retrospectively collected CT scans

postop years	number of CT scans	days after surgery	current (mA)	voltage (kV)	pixel rows/columns	slice distance (mm)
I.	1	7	225	120	512/512	3.75
	2	34	225	120	512/512	3.75
	3	83	225	120	512/512	3.75
	4	138	225	120	512/512	3.75
	5	250	225	120	512/512	3.75
II.	6	446	225	120	512/512	3.75
	7	656	225	120	512/512	3.75
III.	8	1027	225	120	512/512	3.75
IV.	9	1384	225	120	512/512	3.75
V.	10	1734	225	120	512/512	3.75
VI.	11	1937	225	120	512/512	3.75
	12	2112	225	120	512/512	3.75

CT (Computer Tomography)

3.3.3. Gait evaluation after total sacrectomy

During the surgery the lumbosacral intervertebral disc was resected, and the dural sac (together with the cauda equina) was cut through immediately below the L.5 origins. Bilaterally the cranial and ventral ligaments of the S.I joints and the nerve roots (bilaterally below the S.1) were both cut through at the lateral aspect of the tumour [80]. However, the patient was able to walk with crutches at 3-month (m) FU, and without any assisting device at 12m FU. In order quantify and evaluate the gait of the patient at 6-year FU a gait analysis was performed. Gait data was acquired while the patient walked along a straight path at a self-selected speed. The subject was fitted with a full body VICON plug-in-gait marker setup. Three-dimensional kinematic data was recorded using a 6-camera system (MXT40, VICON, UK). Kinetic data was acquired using one force platform (AMTI OR6, USA) mounted halfway along the path. Lower limb kinematics and kinetics were calculated using NEXUS (VICON, UK) and compared to normative data.

DOI:10.14753/SE.2020.2439

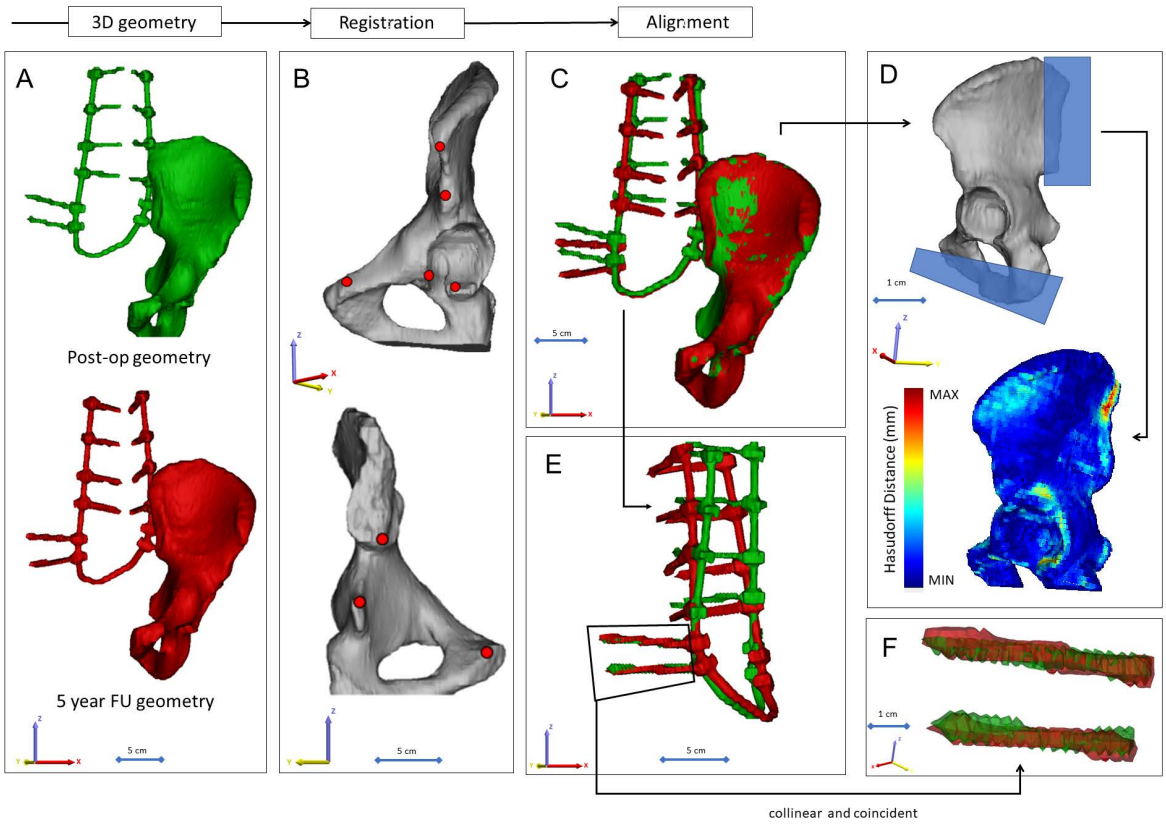

Figure 10. Postop CT scan-based geometry definition and alignment. **A** Thresholding based segmentation was performed on the postop CT scan in order to define the left iliac bone and the implant construct. **B** 8 landmarks corresponding to anatomical landmarks where used for the simultaneous registration of the iliac bone and implant construct geometry. **C** every postop iliac bone + implant construct geometry was registered to the first postop geometry. **D** the Hausdorff Distance was used as a metrics for the alignment accuracy evaluation. Geometrical reduction of the caudal and posterior part or the registered iliac bones was performed. **E** the trans iliac screws body's geometry overlapped after the iliac bone registration. The axis of the iliac screws were considered to be collinear and coincident.

3.3.4. Image processing, 3D geometry definition

In order to define the deformation of the Closed Loop implant construct we defined the construct 3D geometry and arbitrary the left iliac bone 3D geometry in every CT data set. We considered the iliac bone geometry constant, however at the fusion site after the

alignment a symmetric geometry reduction was performed by a cube substraction, in order to exclude the geometrical difference, the same substraction was performed for all geometries at the Ischial ramus, where the last axial CT slice ended for the first postop scan (for the rest all the pelvis was covered in the scan) **(Figure 10D**.) Segmentation process was performed on the 2D CT images [74]. For this, the thresholding algorithm and manual segmentation tools (erase, paint, fill etc.) in Mimics® image analysis software (Mimics Research, Mimics Innovation Suite v21.0, Materialise, Leuven, Belgium) were used. (**Figure 10A**). During the segmentation process the bone volume was first separated from the surrounding soft tissue by thresholding of the Hounsfield units' levels, and the left iliac bone was isolated, then the implant geometry was separated. The resulting masks (group of voxels) were homogenously filled by preserving the outer contour of the geometrical border in 2D. From the masks, a triangulated surface mesh was automatically generated for the iliac bone and for the implant construct (**Figure 10A**). To evaluate the accuracy of the segmentation process, we calculated the Dice Similarity Index (DSI) [75, 76] (for the DSI definition see Matherials and methods**,** 3.2.2. Definition of pre- and postop motion segments' 3D geometry). The DSI values range between 0 and 1, one denoting a perfect match. The implant geometry and the iliac bone geometry were segmented 12 times by (I_1) and repeated by (I_2), the second segmentation was compared to I_1 after which the DSI was defined.

3.3.5. Alignment of the implant construct geometries

To determine the implant deformation the 12 segmented (I_1) implant geometry with the iliac bone were aligned in the same coordinate system. The first postop CT scan based left iliac bone was used as the reference geometry. A control points based rigid registration algorithm was used via Mimics® software. The 8 control points corresponded to easily identifiable anatomical landmarks at the left iliac bone (**Figure 10B)**. During the registration the implant construct moved together with the iliac bone (**Figure 10C)**. To evaluate the accuracy of the registration and alignment procedure the Hausdorff Distance (HD) was measured with the MeshLab1.3.2 software [77] (http://www.meshlab.net) Metro tool [78] (**Figure 10D**) at the level of the aligned iliac bones. As described in the Materials and Methods section (3.2.3. Alignment of the motion segments' geometry), the HD represents the maximum distance

between two points (triangle vertex) of two sets, both from corresponding sections of the meshes (i.e.: the HD is expected to be equal to zero in case of a perfect alignment of absolute symmetrical geometries, whereas values >0 provide the actual distance between the two surfaces). The alignment of the 12 geometry was performed by I_1, and he HD measurements were performed from the second postop CT scan to the last 12^{th} scan compared to the first postop scan-based geometry. After registration of the iliac bones the trans iliac screws body's geometry overlapped. The axis of the iliac screws where consider to be collinear and coincident (**Figure 10E**, **F**). To test this hypothesis HD values were calculated for the screw body's by comparing the geometries to the first postop CT scan geometry after the alignment.

3.3.6. Implant deformity measurements

The implant construct geometry was considered a tubular structure and the centreline of the geometry was defined with the Mimics Software (**Figure 11A**). A „mobile" point corresponding to the L2 right pedicle screw tip and a fix point was selected in the centreline corresponding to the tip of the caudal iliac screw. The distances between the point were measured in three anatomical planes (**Figure 11B, C, D**) using 3-matic® software (Mimics Innovation Suite v21.0, Materialise, Leuven, Belgium). The segmentation of the implant construct, the centreline definition and the distance measurement in the three planes were performed by three investigators (I_1, I_2, I_3) a two different time points (T_1, T_2). For the repeatability and reliability test of the measurements from the X_d (coronal plane), Y_d (axial plane), Z_d (sagittal plane) the three dimensional distance $3D_d$ was calculated using the formula $3D_d=\sqrt{X_d^2 + Y_d^2 + Z_d^2}$

DOI:10.14753/SE.2020.2439

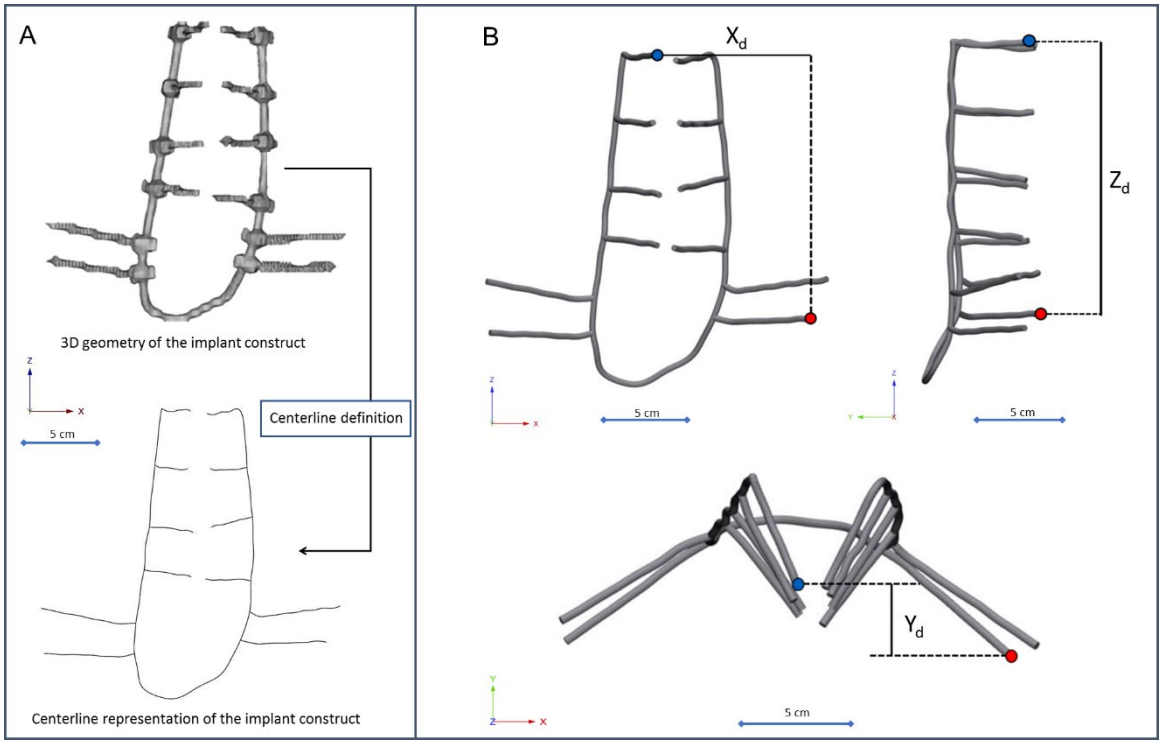

Figure 11. Implant construct geometry simplification and deformation measurement. **A** the segmented geometry of the implant construct was considered a tubular structure, the centerline of the geometry was defined. **B, C, D** a fix point (red dot) was selected in the centerline corresponding to the tip of the caudal trans iliac screw, and a mobile point (blue dot) corresponding to the L2 right pedicle screw tip. The distance between the point were determined **B** in the coronal plane (X_d), **C** sagittal plane (Z_d), **D** axial plane (Y_d)

3.3.7. Mapping of the bony fusion

In every CT scan, from the same region of interest (midplane between the right LIV and LV pedicle screw) a single axial slice was selected (**Figure 12A**). The bone tissue was segmented based on thresholding algorithm, to determine the outer boundary of the bony element (left and right iliac bone, and L.IV vertebra) (**Figure 12B**). The mask internal part was filled and a homogenous mask was created, from this mask a voxel based FE mesh was created with the Mimics Software (**Figure 12C**, **D**). Form the institutional PACS database QCT scans

where selected with the same acquisition protocol and machine **(Table 3**). The date of the scans where selected to be in the same month as the postop CT scans. The male subjects also had to have similar body mass index (BMI=28±2) as the presented patient (BMI=28). The Hounsfield Units values of the QCT images were converted into BMD equivalent values by using a densitometric calibration obtained with an inline phantom (HitachiPresto,Hitachi Medical Corporation,Tokyo, Japan) with five cylindrical insertion with known mean equivalent BMD values (0, 0.5, 0.1, 0.15, and 0.2g/cm^3). Based on the 12 QCT a mean conversion curve was defined and assumed to be linear (BMD=ρQCT=a+b*HU, where ρQCT [g/cm^3] is bone density) according to studies [9,10]. Figure 12E. In the voxel-based FE mesh every element was coded with 10 different colour code corresponding to the BMD values as shown in **Figure 12F.** The distribution of the FE nesh voxel element over the FU was analysed. The volume of the BMD categories were calculated (voxel dimension*number of elements) and visualised using a 3D surface plot (**Figure 38)** created with SigmaPlot 12 (SSI, San Jose, California, United States).

3.3.8. Statistical analysis

All statistical tests were performed with SPSS statistical package version 23 (SPSS Inc, Chicago, IL). Due to the small sample size we used non-parametric tests. Inter-rater (I_1 vs I_2 vs I_3) reliability was determined by Intraclass Correlation Coefficient (ICC) estimates and their 95% confident intervals (CI) were calculated based on a mean-rating (k = 2), absolute-agreement, 2-way mixed-effects model. Intra-rater (I_1T_1 vs I_1T_2, I_2T_1 vs I_2T_2, I_2T_1 vs I_2T_2) reliability was determined by ICC estimates and their 95% confident intervals were calculated based on a single measurement, absolute-agreement, 2-way mixed-effects model. The relationships between the implant deformation in the anatomical planes and the number of postop days were analysed by the Spearman's rank correlation (**Figure 36**).

DOI:10.14753/SE.2020.2439

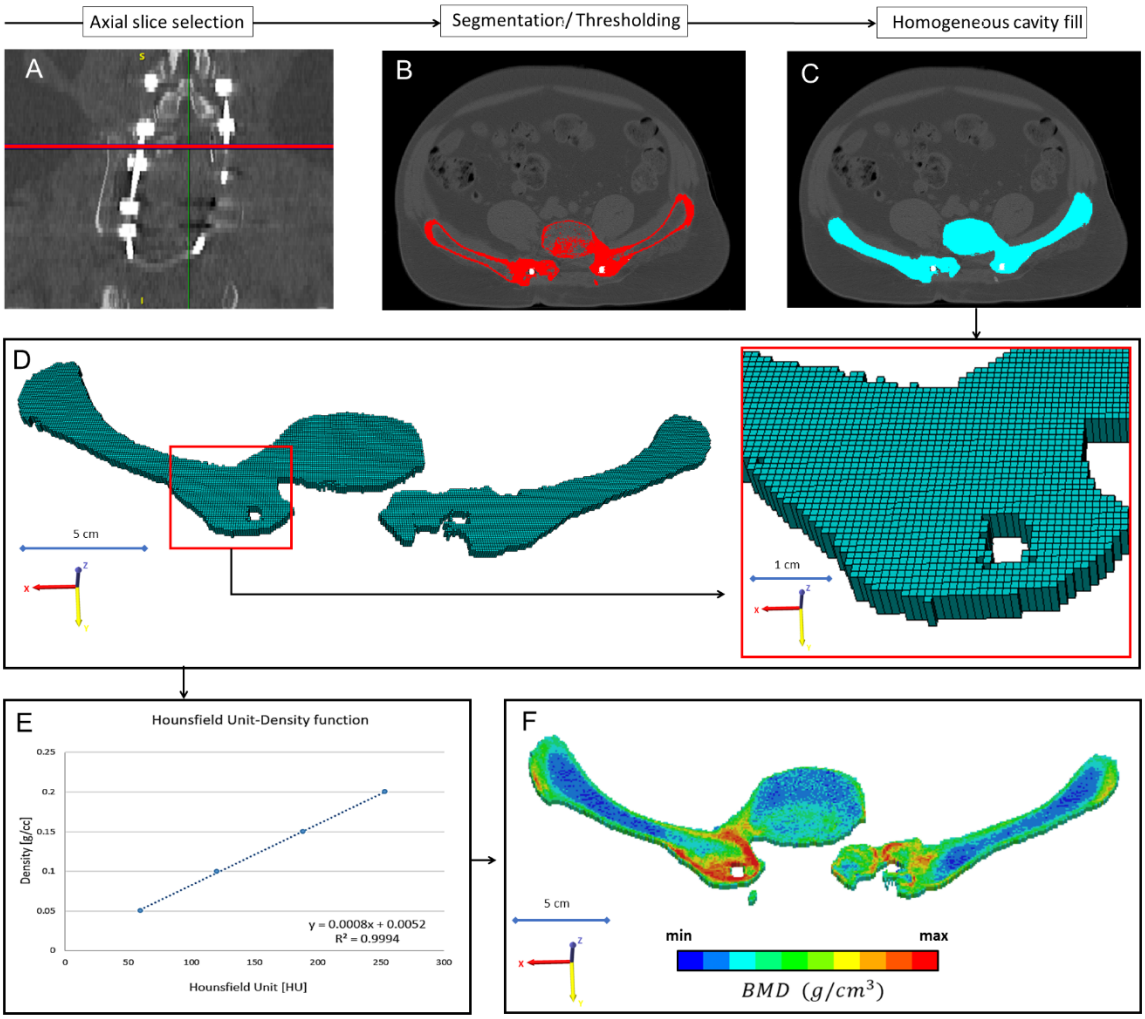

Figure 12. Evaluation of the bony fusion process between the LV vertebra and the two iliac bone. **A** from all the 12 CT scans, form the same region of interest (midplane between the right LIV and LV pedicle screw) an axial slice were selected. **B** the bone elements were segmented in the slice. **C** a homogeneous mask was crated corresponding to the bony element. **D** a voxel-based FE mesh was created based on the segmented mask. **E** a linear relationship was used to assign the bone mineral density values for the corresponding Hounsfield values. **F** in the voxel-based FE mesh every voxel was coded with a color code corresponding to the BMD.

3.4. PART IV. Application of 3D printing in spine care

3.4.1 Definition of the 3D geometry

A CT scan of a lumbar fourth (LIV) vertebra of a 25-year-old patient was selected from a study of 270 patients who underwent different treatments due to low back pain in our clinic (MySPINE, Project ID: 269909, Funded under: FP7-ICT). The vertebra of our interest and the neighboring segments were not affected by any musculoskeletal pathology. In order to define the 3D geometry, we performed thresholding and manual segmentation in 3D Slicer 4.1.1 [81], an open-source, free software: http://www.slicer.org (**Figure 13**).

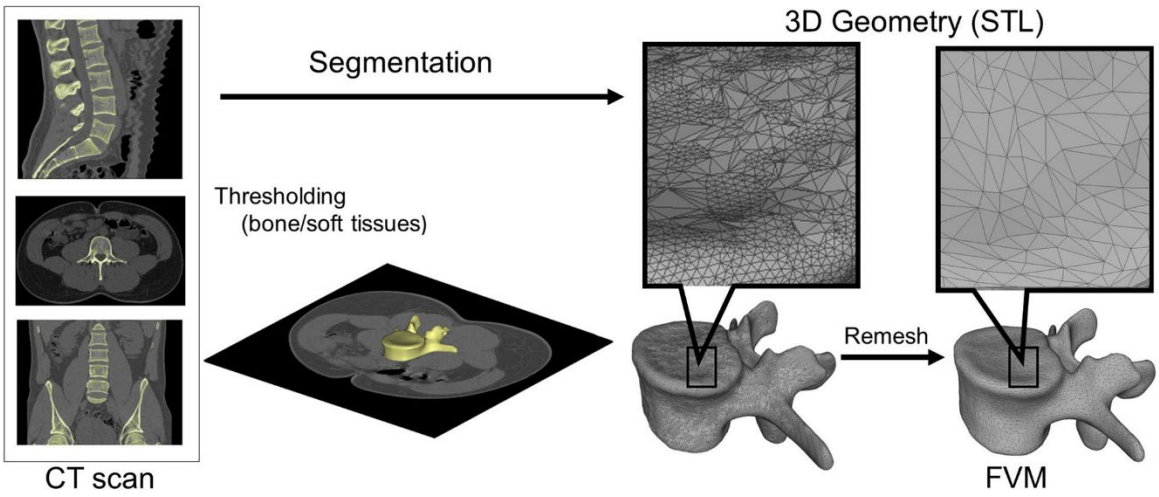

Figure 13. Definition of virtual 3D geometry from 2D medical images. During the segmentation process the bone volume is first separated from the surrounding soft tissue by thresholding of the greyscale levels of the CT images. The resulting mask (yellow) voxels represent the 3D volume of the vertebra. Then, from the mask, a triangulated surface mesh is automatically generated and exported into in STL (STereoLithography) format. Before 3D printing the quality of the 3D surface mesh is adjusted (remesh), while preserving the geometrical accuracy. The final vertebra model (FVM) is built from 8024 vertices and 16048 triangulated faces.

To evaluate the accuracy of the segmentation process, we calculated the Dice Similarity Index (DSI) with 3D Slicer Dice-Computation tool [76], for the DSI definition see methods: 3.2.2. Definition of pre- and postop motion segments' 3D geometry. The DSI values range between 0 ± 1, one denoting a perfect match. DSI value of the segmentation process was 0.96 indicating a high accuracy.

3.4.2 3D printing

The segmented geometry was converted to STereoLithography (STL) format using the "ModelMaker" module of 3D Slicer. Inspection and correction of the 3D geometry was performed with MeshLab1.3.2 [77] (an open-source free software: http://www.meshlab.net), and the following adjustments were made on the triangulated surface mesh: (1) isolated pieces were considered artefacts and therefore, were removed; (2) duplicate edges and faces, that resulted from unification were deleted; (3) universal remeshing with contour preservation. A final vertebra model (FVM) was built from 8024 vertices and 16048 triangulated faces (**Figure 13**).

The FVM was printed with the following two 3D printing technologies: (1) Fused Deposition Modelling (FDM) device (Dimension 1200es 3D Printer; Stratasys, Israel) **Figure 14A**, in which a thin filament of plastic (ABSplus in ivory) is melted in an extruding head, which is then deposited to build the desired shape, slice by slice, on a moving platform. During the printing all the significantly protruding parts are supported by a concurrently printed scaffold (printed from a water-soluble plastic; Soluble Support Technology, SST). The internal grid structure of the model (**Figure 14C**) is automatically generated. The building size of the machine is 254 x 254 x 305 mm and operates with a layer thickness of 0.330-0.254 mm. (2) The Digital Light Processing (DLP) device (VOXEL L 3D Printer; Do3D, Hungary) polymerizes selectively illuminated planes of the model, slice by slice (**Figure 14 B**). The DLP uses a model material Voxeltek White Resin (photo-polymer, acrylic based), and a light emitting diode (LED; with ultraviolet spectrum) as a light source. Upon selective illumination, the model material becomes polymerized and solid. The internal structure of the printed vertebra is empty (**Figure 14D**). The building size of the

machine is 125 x 65 x 65 mm, the wall thickness for the FVM was set to 1.2 mm, the printer operates with a layer thickness of 0.1-0.025 mm.

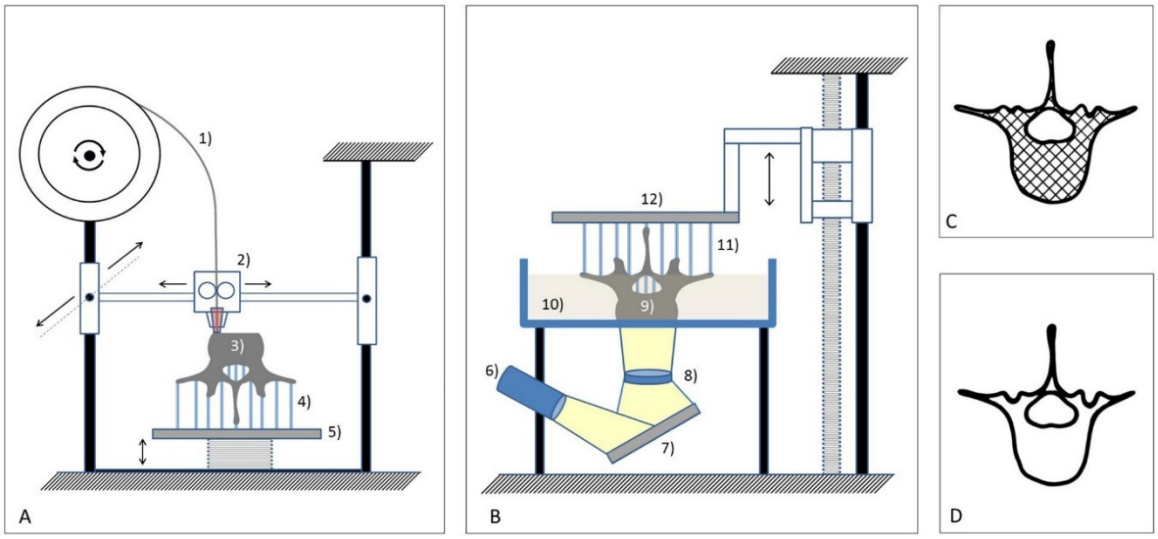

Figure 14. Schematic representations of the Fused Deposition Modelling (FDM) and Digital Light Processing (DLP) 3D printing technologies. **A** FDM: a thin filament of plastic (1) is melted in a extruding head (2) and deposited to build the vertebra (3), slice by slice on a moving platform (5). The complex geometry of the vertebra requires vertical column scaffolding (4) during the layer deposition. **B** DLP: UV light (6) is projected on a deformable mirror device (7) and directed, through a lens (8) to the surface of the bottom most layer of the liquid photopolymer resin (10). The light selectively polymerizes the resin, which then becomes solid (9). This process also requires vertical column scaffolding (11). Finally, a moving platform (12) raises the already solidified resin. **C**-**D** illustration of the internal perpendicular grid structure of the vertebra printed with (**C**) FDM (axial plane cross section) and the empty internal structure of the vertebra printed with (**D**) DLP (axial plane cross section).

3.4.4. Comparison of the 3D physical models printed with FDM or DLP

The FDM and the DLP printed models were scanned (ScanBox 3D scanner; Smart Optics Sensortechnik GmbH, Bochum, Germany) in two measurement sessions and in two orientations. The measurement field was 80x60x85 mm with a resolution of 0.006 mm (ISO

12836). First, the vertebra was attached to the scanner support system from the inferior endplate, with the optical system focusing on the superior part of the vertebra. Based on these measurements we created FDM-sup and DLP-sup two-point clouds. Next, we attached the model from the superior endplate and the optical unit focused on the inferior part of the vertebra and we created FDM-inf and DLP-inf point clouds. Based on these point clouds the scanner driving software created triangulated surface mesh models. The models where then exported in STL format.

In order to align their overlapping components with the segmented vertebra surface mesh model (FVM) used as reference geometry, the FDM-sup, DLP-sup, FDM-inf and DLP-inf, 3D data sets were transposed into the same coordinate system by surface registration. We used MeshLab1.3.2 software Align Tool for the point based rigid registration process. Eight symmetrical (left-right sides, 4-4) and two asymmetrical control points were selected from the superior and inferior region of the reference FVM and from the aligned geometry, respectively (**Figure 15**).

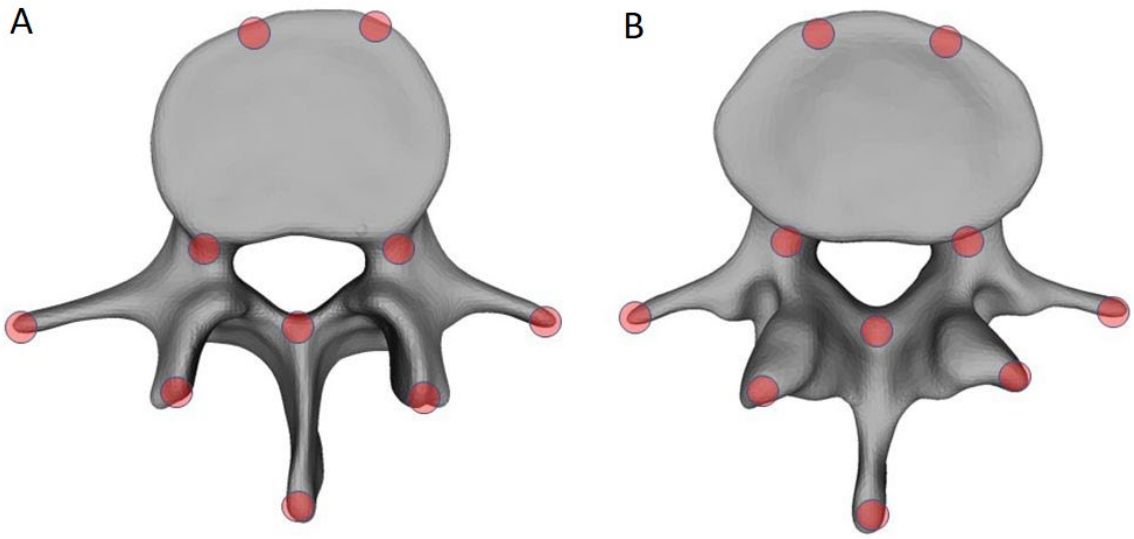

Figure 15. Control points selection for the rigid surface registration. Ten control points were selected from the superior (**A**) and inferior (**B**) region of the reference FVM and from the aligned geometry, respectively. Red circles represent the registration points selection areas.

The points where in the following regions: anterior part of the endplate (1-1), in the pedicles (1-1), in the articular processes (1-1), in the transvers processes (1-1) and one point for the apex of the vertebral arch, and another for the spinous process. The registration was performed by the two investigators (I_1, I_2) and at two different time points (T_1, T_2).

To evaluate the accuracy of the registration and alignment procedure the Hausdorff Distance (HD) was measured with the MeshLab1.3.2 software Metro Tool [78]. The HD represents the maximum distance between two points of two sets, both from corresponding sections of the meshes (i.e.: the HD is expected to be equal to zero in case of a perfect alignment of absolute symmetrical geometries). Theoretically, its values range from 0 to ∞, with 0 indicating that the compared volumes have identical boundaries, whereas values greater than zero provide the actual distance between the two surfaces. Because the values not only indicate the precision of the printing technology, but also the precision of the surface registration, this process was conducted by two independent investigators (I_1, I_2) and at two different time points (T_1, T_2). The HD values were calculated at the vertices of the triangulated surface meshes as follows: $h(A,B) = max_{a\epsilon A}\{min_{b\epsilon B}\{d(a,b)\}\}$; where *A* is the FDM-sup, DLP-sup, FDM-inf, DLP-inf mesh; *B* is the FVM reference mesh; *a* and *b* are points from sets *A* and *B*, respectively, and *d(a, b)* is the Euclidean distance between these points.

In order to measure Surface Roughness (SR), two symmetrical rectangular surface areas from the superior endplates and from the right superior part of the pedicles of the aligned (I_1T_2) FDM-sup and DLP-sup meshes were determined and separated as regions of interest (ROI) with Autodesk ReMake (free for academics, https://www.autodesk.com/) and Autodesk Meshmixer 3.1 (free software, http://www.meshmixer.com/). The selected and isolated ROIs were exported in STL format, and the surface roughness was then quantified with CloudCompare v2.6.0 open-source software (R&D Institute EDF, Paris, France, https://www.danielgm.net/cc/). For each point (vertices of the triangulated surface mesh), the roughness value represents the distance between the point of interest and the best fitting plane, which is computed from its nearest neighbours within a defined kernel. The kernel size equals with the radius (mm) of a sphere centered on each point. In case of the endplates it was set to: 0.5, 1,1.5, 2, 2.5 and 3 mms respectively (6 individual measurements); and to

0.5, 0.6, 0.7,0.8, 0.9, 1 mms, respectively (6 individual measurements) in the case of the pedicles.

3.4.5 Application of 3D printed physical models in surgical planning

An FDM model was used for planning the trajectory of transpedicular screw insertion in case of a 12-year-old patient suffering from congenital scoliosis (**Figure 16**) caused by an LI hemivertebra. A preoperative CT scan, with 1.25 mm slice thickness, was performed from the lower part of ThXI vertebra to the upper part of LIII vertebra. The data was exported from the hospital PACS in DICOM file format. To fulfil patient data protection, de-identification of the DICOM data was performed using the freely available Clinical Trial Processor software (Radiological Society of North America, https://www.rsna.org/ctp.aspx). The vertebras from the anatomical region of interest were segmented with 3D Slicer 4.1.1 as described in case of the FVM, and a model including ThXI-LIII vertebras was created.

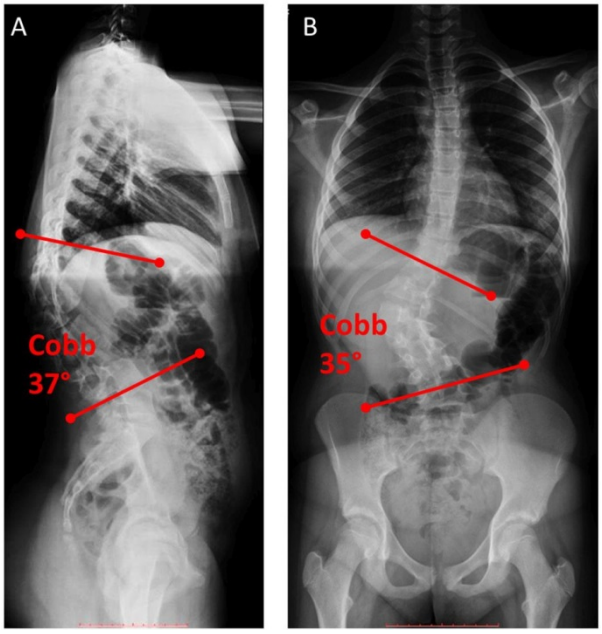

Figure 16. Standing X-ray images of the thoracic and lumbar spine, and the pelvis of the patient. A- B, The 12 year old female patient suffers from congenital scoliosis, caused by LI hemivertebrae. The (A) kyphotic deformity is 37º Cobb angle in the sagittal plane (lateral view) and the (B) scoliotic deformity is 35° Cobb angle (antero-posterior view).

The segmented volumes were converted to STL using the module ModelMaker option. Inspection and correction of the 3D geometry was done with MeshLab. The model was then printed with FDM technology and was used for planning the trajectory of the screw insertion at the ThXII and LII levels. Ten cm long 1.3mm diameter titanium rods were

inserted in the pedicles in the ideal axis, the orientation of these guided the surgeon visually, during the operation, to find the optimal angle and axis of the screw insertion.

3.4.6 3D data integration in the clinical communication

The virtual model used in the clinical case was imported in STL format to MeshLab1.3.2 and subsequently saved as a Universal 3D File (U3D). A 3D Portable Document Format (3DPDF) file, containing the U3D mesh, was created using Adobe Acrobat (version 10 Pro Extended) 3D tools with default Activation Settings and assignment of a Poster Image from default view. The 3D visualization parameters were set as follows: CAD optimized lights, white background, solid rendering style and default 3D conversion settings. The 3DPDF file was incorporated in our institutional web browser-based SQL database (Oracle Database 12c) which is accessible by clinicians from any institutional desktop PC or mobile device.

3.4.7 Statistical analysis

All statistical tests were performed with SPSS version 23 (IBM, Armonk, New York, United States). HD and SR measurement related dataset normality distribution was testedby the Kolmogorov-Smirnov test with Lilliefors Significance Correction (sample size >2000, $p \leq 0.05$). The between group statistical difference was assessed by Independent Samples Kruskal-Wallis test ($p \leq 0.05$) for **Figure 39** and Two-sample Kolmogorov–Smirnov test ($p \leq 0.05$) for **Figure 40** and **Figure 41**.

The cumulative probability plots were created with SigmaPlot 12 (SSI, San Jose, California, United States). The data management was performed in Microsoft Excel 2016 (Microsoft, Redmond, Washington, United States)

DOI:10.14753/SE.2020.2439

3.5. PART V. Affordable patient-specific surgical navigation

3.5.1. Clinical Case

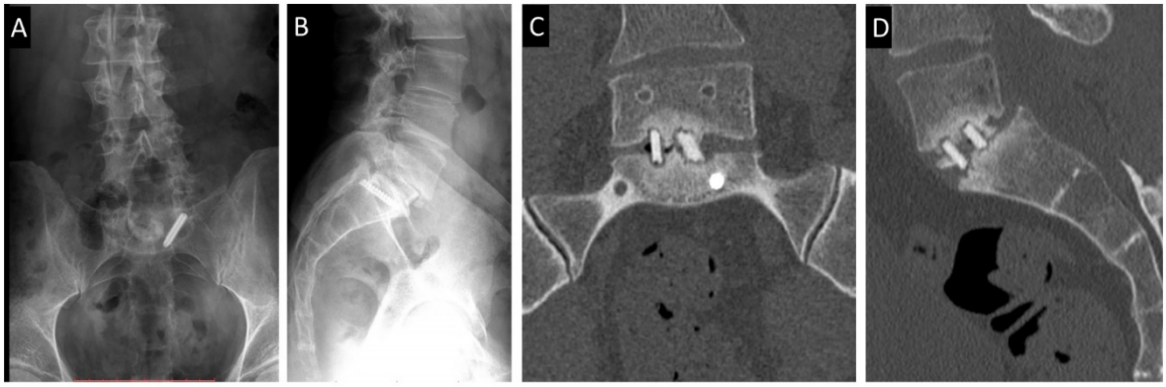

Figure 17. Clinical case of a 38-year-old male patient suffering from low back pain. The patient previously underwent multiple surgeries at the LV-S1 level. A broken left sacral screw can be identified on the standing X-ray images of the patient (**A** coronal, **B** sagittal plane). Signs of non-union are identifiable in the intervertebral space on the CT scan images of the LV vertebra and the sacrum (**C** coronal, **D** sagittal plane).

The study was approved by the National Ethics Committee of Hungary and the National Institute of Pharmacy and Nutrition (reference number: OGYÉI/163-4/2019). Informed consent was obtained from the patient. A 38-year-old patient underwent multiple spine surgeries at the LV-SI level over a 5-year period with transforaminal interbody fusion (TLIF). During the latest surgery, implant removal and S.I left side nerve root decompression were performed and 6 months later the patient was referred to our institution due to manifestation of mechanical low back pain, with no sign of sensorimotor deficit. Medical imaging at admission (**Figure 17**) showed a broken SI left side pedicle screw, and a non-union in the LV-SI intervertebral space. Refusion surgery was decided, however the broken screw caused a geometrical and technical difficulty for new screw insertion. The case raised the need for a safe screw insertion without compromising the local bone tissue.

4.5.2 Patient-specific 3D geometry definition

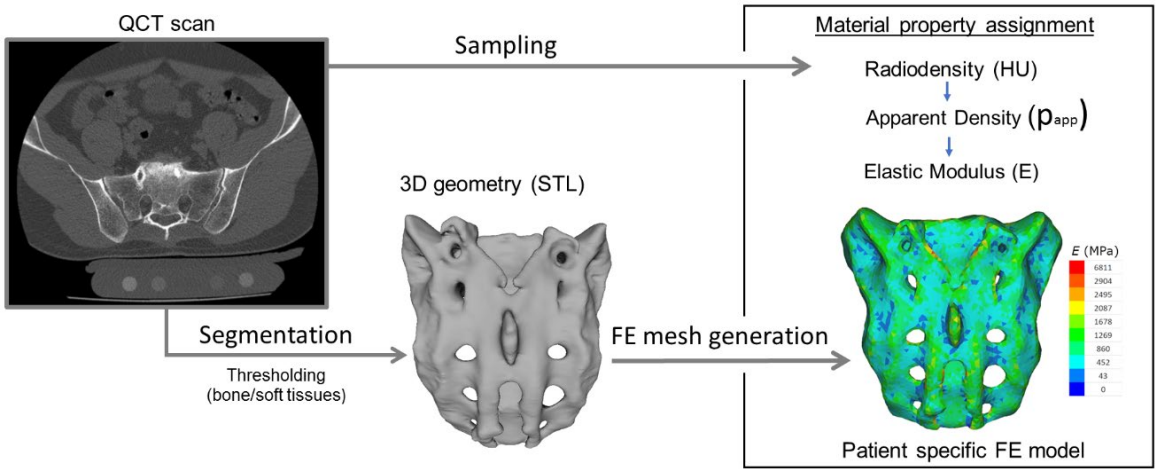

Figure 18. Patient-specific geometry and FE model definition. QCT based segmentation was used to define the sacrum geometry. Hounsfield Unit (HU) values of the QCT images were converted into bone mineral density (BMD) equivalent values. Elastic properties of the sacral bone were estimated using a set of density to elasticity relationships from the literature to convert the BMD equivalent value at each element of the FE mesh to Apparent Density (ρ_{app}) (Rho et al., 1995; Kopperdahl et al., 2002) and then to the Elastic Modulus (E).

For the study Quantitative Computed Tomography (QCT) scans were used, performed with a Hitachi Presto CT machine (Hitachi Presto, Hitachi Medical Corporation, Tokyo, Japan) using an in-line calibration phantom with five cylindrical insertions of known mean equivalent bone mineral density (BMD) values (0, 0.5, 0.1, 0.15, and 0.2 g/cm^3) with an intensity of 225mA and voltage of 120kV. The imaging protocol was previously defined in the MySPINE project (ICT-2009.5.3 VPH, Project ID: 269909) [71], [72], and the images were reconstructed with a voxel size of 0.6x0.6x0.6 mm^3. The data was extracted from the hospital PACS in DICOM file format. To comply with the ethical approval of the patient data protection, deidentification of the DICOM data was performed using the freely available Clinical Trial Processor software (Radiological Society of North America, https://www.rsna.org/ctp.aspx) [73]. The thresholding algorithm and manual segmentation tools (erase, paint, fill etc.) in Mimics image analysis software (Mimics Research, Mimics

Innovation Suite v21.0, Materialise, Leuven, Belgium) were used **(Figure 18.)** to define the geometry of the sacrum and the broken screw. The resulting masks (group of voxels) were homogenously filled by preserving the outer contour of the geometrical border in 2D. From the mask, a triangulated surface mesh was automatically generated. On the 3D geometries surface smoothing (iteration: 6, smooth factor: 0.7, with shrinkage compensation) and uniform remeshing was applied (target triangle edge length 0.6 mm, sharp edge preservation, sharp edge angle 60°).

3.5.3. Surgical planning and FE model generation

A CD Horizon Legacy (Medtronic) polyaxial pedicle screw, 45 mm long and 6.5 mm in diameter, was scanned with ScanBox 3D scanner (Smart Optics Sensortechnik GmbH, Bochum, Germany). The model of the screw was reconstructed and modified (from polyaxial to monoaxial head) in 3-matic (Mimics Research, Mimics Innovation Suite v21.0, Materialise, Leuven, Belgium) software. The triangulated surface mesh of the screw model was uniformly re-meshed (target triangle edge length: 0.6 mm, sharp edge preservation, sharp edge angle: 60°) **Figure 19A**. The screw model was virtually inserted in the 3D model of the patient sacrum in two position (convergent S.I, divergent ALA) using the Mimics software STL import toll (**Figure 19B**) by taking in account and overcoming the broken screw geometry caused difficulty. Two non-manifold assemblies were created in the Mimics software containing the broken screw, implanted screw and sacrum for the convergent (S1) and divergent (ALA) positions. The assembly was exported to the 3-matic software where 9 FE meshes were generated for each of the implantation scenarios (S1, ALA). The broken screw, inserted implant, and sacrum-implant interface had a triangle set with an edge length of 0.6 mm. The outer surface of the sacrum mesh was changed in the 9 models by defining the uniform triangle mesh edge length as 2.0, 2.5, 3.0, 3.5, 4.0, 4.5, 5.0, 5.5, 6.0 mm. Adaptive meshing protocol was used for the volume mesh creation with 10-node tetrahedral elements. The maximum edge length of the meshing process corresponded with the initial edge length of the sacrum surface mesh (**Figure 20**), for the screw and the broken screw the same FE mesh parameters was used in all models. The material property assignment for the volumetric elements representing the sacral bone tissue was performed in two steps (**Figure 18**). In the

first step conversion of the HU (*Hounsfield Unit)* values to BMD values based on the in-line phantom was performed, the conversion curve was assumed to be linear according to studies [20],[21]. The obtained relationship between the HU and the apparent bone density for each element was $\rho_{app} = -0.0829 + 0.0026 \cdot HU$, ($\rho_{app}$ [g/cm³]). Then, the bone tissue was assumed to be isotropic and linearly elastic with a Poisson's ratio of 0.3 [84]. Conversion curves between the density and the elastic modulus of the bone were based on the correlation established by Kopperdahl et al. [85], $E = -34.7 + 3230 \cdot \rho_{app}$, (bone elastic modulus = E [MPa]). The FE models were exported to Abaqus/CAEv11 (Dassault Systemes, Simulia Corp, Providence, RI, USA). For the broken and the inserted pedicle screws the material properties were defined as follows: Poisson's ratio of 0.3 [86], elastic modulus of 114000 MPa [86]. Between the screws and the sacrum tie connections were used. The finite element model was subjected to a static 500 N tensile load applied to the screw head and it was fixed at the S.I endplate and lower third of the sacrum (**Figure 19C**)

DOI:10.14753/SE.2020.2439

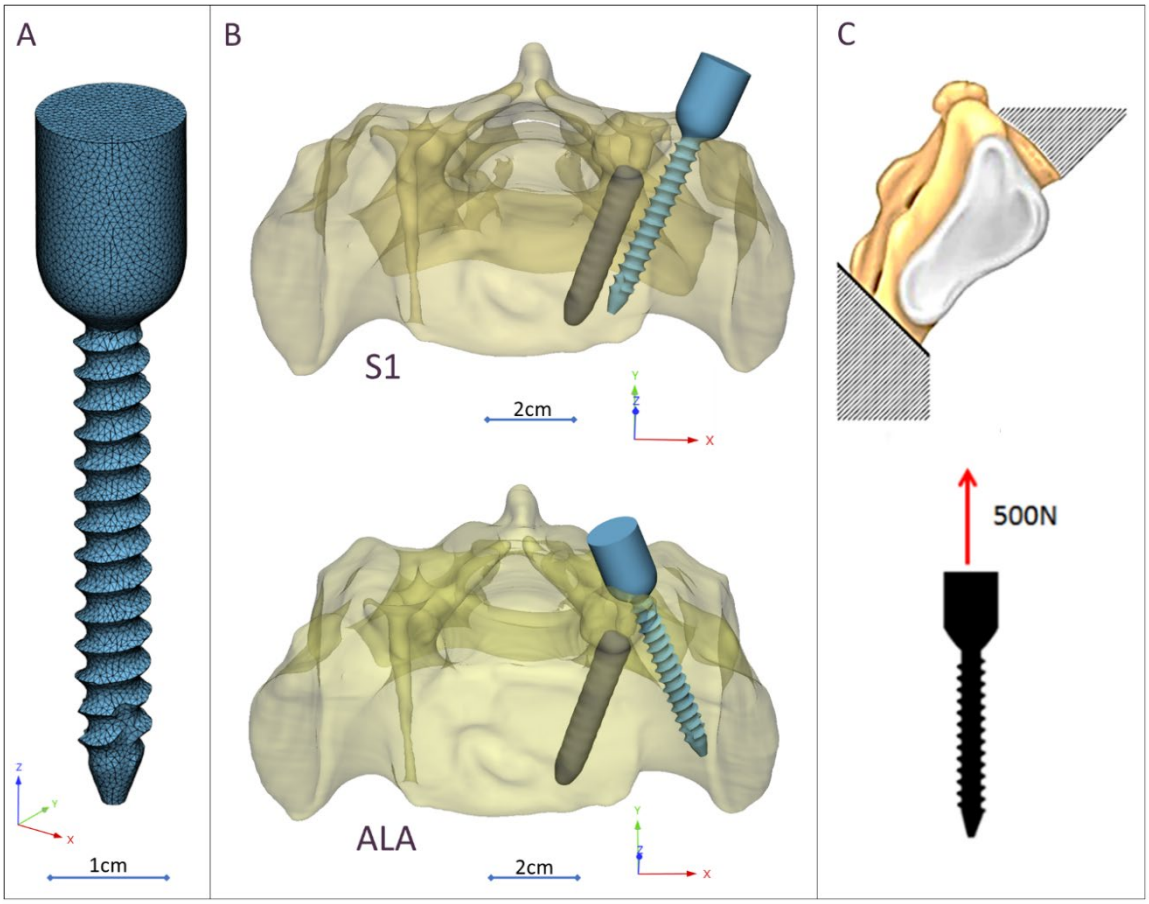

Figure 19. Virtual pedicle screw insertion into the patient-specific sacrum model. **A** modified (monoaxial) virtual model of the pedicle screw. **B** pedicle screw insertion in the convergent position (S1) and divergent position (ALA), the geometrical difficulty caused by the broken screw was overcome in both insertions. **C** boundary condition of the FEA, the sacrum was fixed on the S.I endplate and the caudal 1/3 of the sacrum, 500 N tensile load was applied on the screw head.

DOI:10.14753/SE.2020.2439

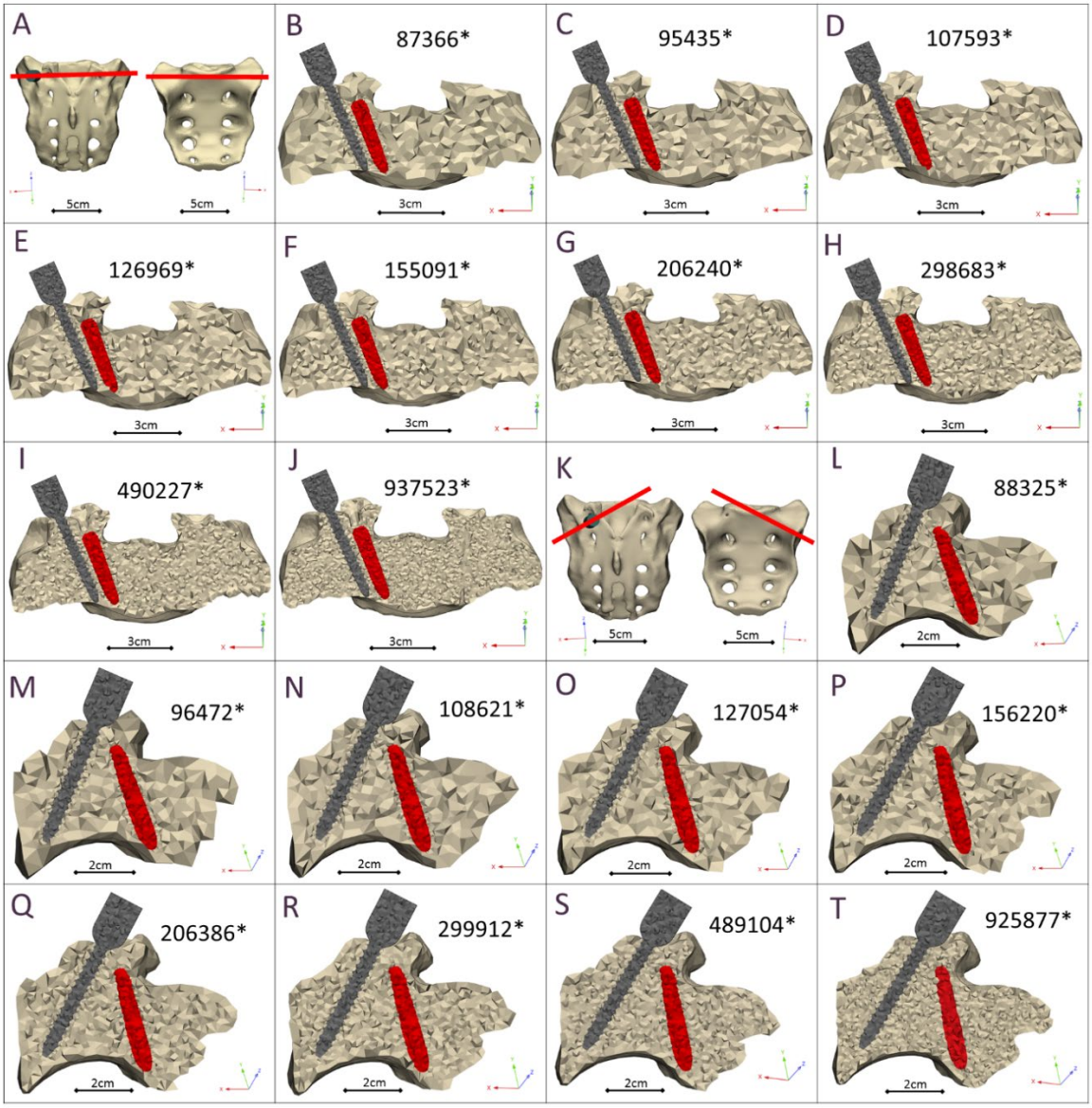

Figure 20. Finite element models of the sacrum with convergent (S1) and divergent (ALA) screw insertions. **A** section plane in the convergent screw insertion model (posterior and anterior view). **B-J** the screw is inserted into the convergent position in close proximity to the broken screw (red). **K** section plane in the divergent screw insertion model (posterior and anterior view). **L-T** the screw is inserted into the convergent position in close proximity to the broken screw (red). The FE models' mesh element numbers (*) vary according to mesh density.

DOI:10.14753/SE.2020.2439

3.5.4. Navigation template design, manufacturing and accuracy evaluation

The template design was based on the axis of the virtually inserted screw, individual geometry and surface of the cranial/dorsal part of the sacrum. In the 3-matic software the two axes and surface for the template/sacrum contact were defined based on the STL assembly (broken screw, inserted implant, sacrum). The contact surface and the axes were exported to the Autodesk Fusion 360 (Autodesk Inc., California, U.S.A.) CAD software which was used for the finalization of the design (**Figure 21**.**A**).

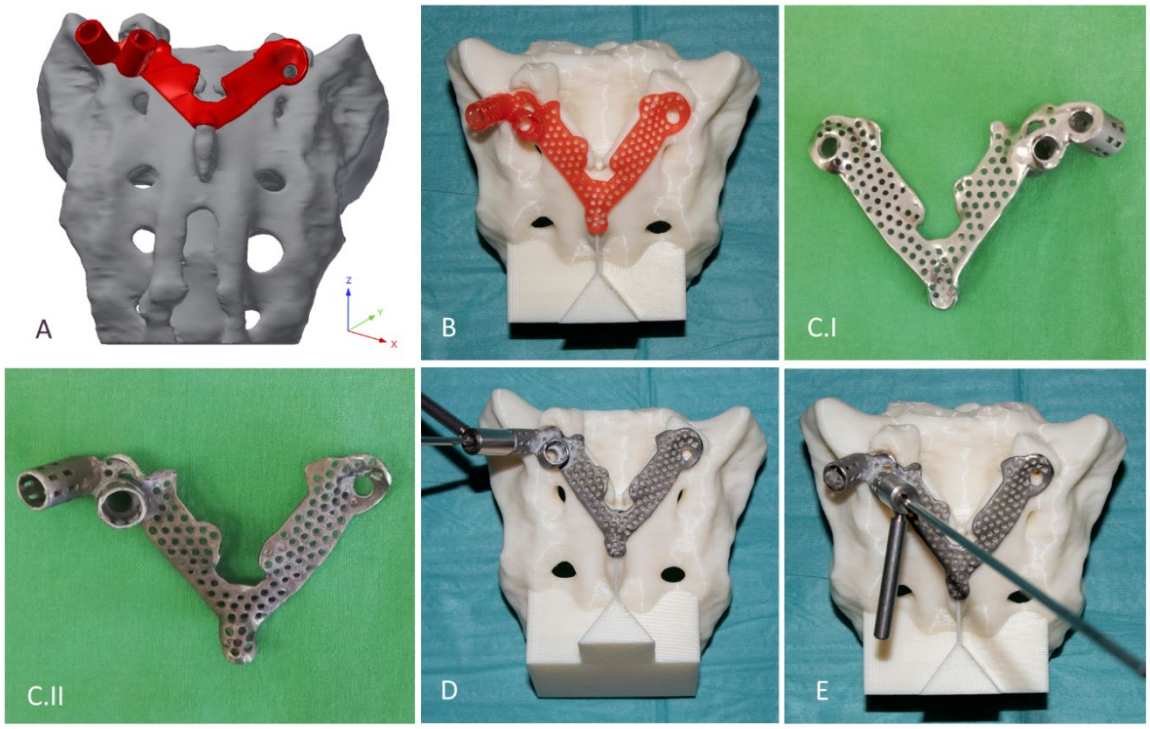

Figure 21. Design, manufacturing and accuracy evaluation of the navigation template. **A** template's virtual model created via CAD software. **B** 3D printed (MSLA technology) template (red) fits exactly on the 3D printed (FDM technology) patient-specific physical model. **C.I-II** final navigation template created via investment casting from cobalt-chrome (**C.I** ventral surface polished, **C.II** dorsal surface). Evaluation of the drilling accuracy was performed on the physical model in the (**D**) convergent position (S1) and (**E**) divergent position (ALA).

The virtual model of the template was printed with a masked stereolithography (MSLA) technology based 3D printing machine (VOXEL L 3D Printer; Parameters: building size: 125 x 65 x 65 mm, layer thickness: 0.05 mm; Material: Voxeltek Cast Resin; Do3D, Hungary)(**Figure 21A,B)**. The used photopolymer resin can be applied as a pattern for investment casting. Finally, the model was produced in a dental laboratory via investment casting (Hexacast induction centrifugal casting machine; Parameters: start torque: 0-21 Nm, maximum melting mass: 100 g, max heating: 1750 °C, dimensions (width x height x depth): 660 x 390 x 645 mm; Material: CoCr; PiDental, Hungary) from cobalt-chrome (**Figure 21C.I-II**). The accuracy of the casted part was tested via 3D scanning ScanBox 3D scanner (Smart Optics Sensortechnik GmbH, Bochum, Germany) and compared to the 3D printed model. The point clouds resulting from the scanning were aligned and compared in the 3-matic software with the part comparison module.

The accuracy of the template was tested on a patient-specific sacrum physical model, 3D printed with a Fused Deposition Modelling (FDM) printer (Dimension 1200es 3D Printer; Parameters: building size: 254 x 254 x 305 mm, layer thickness: 0.330-0.254 mm; Material: ABSplus/ivory; Stratasys, Israel). The drill template was placed on the FDM sacrum model; then, a cylinder inlet was connected to the template to support the drill bit, and the drilling of the model was performed according to the S1 and ALA positions (**Figure 21D,E)**.

The template was removed, and two CT scans were performed of the sacrum model with drill bits inserted in the S1 and ALA positions. The CT scan images were imported into the Mimics software where the segmentation (thresholding) and 3D reconstruction of the patient-specific FDM sacrum model geometry and drill bits were performed. The models were registered to the initial sacrum geometry derived from the QCT via point based rigid registration by selecting anatomical landmarks in the caudal part of the sacrum (**Figure 22**). This step was followed by an automatic global registration inside the 3-matic software. The registration accuracy was measured with the part comparison module of the 3-matic software. The centreline for the drill bit 3D geometry was defined and an analytical primitive (cylinder with 2.5mm diameter was fitted) was fitted to the centreline to visualise the drilling axis.

DOI:10.14753/SE.2020.2439

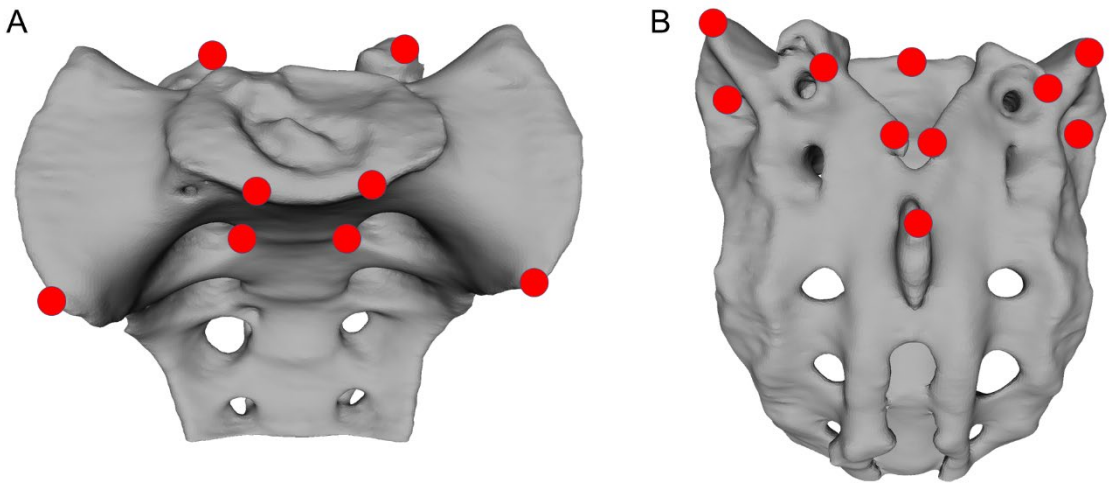

Figure 22. Control points selection for rigid surface registration. Eight control points from the superior-ventral (**A**) region and ten control points from the superior-dorsal (**B**) region were selected from the reference (patient QCT) and aligned geometry (physical model CT scan) respectively. The red circles represent the registration points selection areas.

DOI:10.14753/SE.2020.2439

4.RESULTS

4.1. PART I. Attitude of spine surgeons towards the application of 3D technologies

283 AOSpine members from the six AO regions completed the online survey.

Table 4. Demographics of survey respondents

Characteristic		N (%)
AO Spine region		**283**
	Africa*	1 (0,4)
	Asia Pacific	56 (19,8)
	Europe	101 (35,7)
	Latin America	69 (24.4)
	Middle East	30 (10,6)
	North America	26 (9,2)
Human Development Index (HDI)		**282**
	Very high	158 (56.0)
	High	86 (30,5)
	Medium	38 (13,5)
	Low	0 (0.0)
Practice where you do spine surgeries		**281**
	Public	124 (44,1)
	Private	55(19,6)
	Both	102 (36,3)
Your common practice in spine surgery **		**282**
	Degenerative	236 (83,7)
	Deformity	111 (39,4)
	Tumor	78 (27,7)
	Trauma	142 (50,4)
Years of experience in spine surgery		**281**
	0-3	46 (16,4)
	3-10	94 (33,5)
	10-20	75 (26.7)
	> 20	66 (23,5)
What percentage of your cases are complex, challenging surgeries?		**281**
	0-20%	102 (36,3)
	20-40%	100 (35,6)
	40-60%	57 (20,3)
	more than 60%	22 (7,8)

*Note: The single respondent from AoSpine region Africa was excluded from the survey
Note: **multiple choice

Only one person completed the questionnaire from AOSpine Africa region, thus this region and participant were excluded from further analysis **(Figure 23.).** The study population was grouped into three subgroups based on the HDI of the country of the participants. More than half of the subjects (56.0%) have been from a very high HDI country while 30.5% of the responders have come from a country with high HDI and 13.5% from a country with medium HDI. None of the responders were in the low HDI group. Most of the surgeons perform surgeries in the public system (44.1%) while 36.3% of them operate in a mixed practice and 19.6% work only in private healthcare. Regarding the specialties, 83.7% of the surgeons treat degenerative cases, 50.4% of them have trauma and 39.4% have deformity practice. Out of the responders 27.7% operate on spinal tumors. The majority of the study population has had an experience of 3 to 10 years in spine surgery (33.5%). Regarding the experience 26.7% of the responders had 10 to 20 years, while 23.5% have been more experienced surgeons (more than 20 years in spine surgery). Young surgeons (0 to 3 years' experience) represented the 16.4% of the study population.

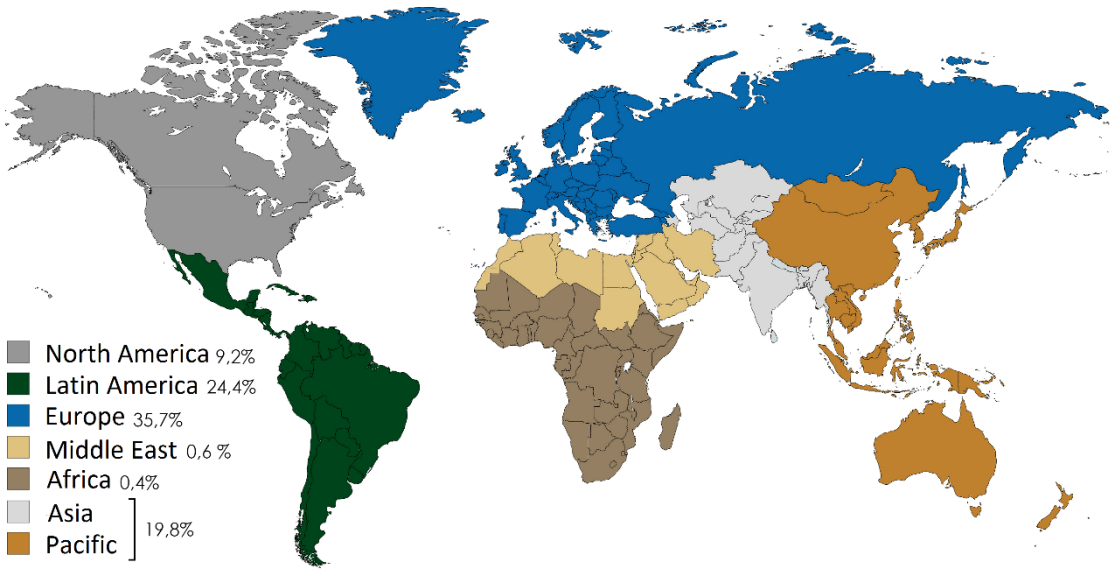

Figure 23. World map indicating the AOSpine regions and the survey respondents (n=283) distribution (%) according to the regions.

Table 5 summarizes the questions and the distribution of the answers related to the acceptance of 3D technologies. 17% of the participants have not had any specific knowledge about the 3D technologies while a similar rate of the subjects (18%) had already used these techniques. Most of the participants (41.5%) have had some information only from the media and a further 23% of the responders had learned about the 3D technologies on scientific forums. Only 7.1% of the clinicians use regularly 3D virtual or printed models for education or demonstration, while 46.1% of the surgeons have never used them. 3D models can play a significant role in the surgical planning [87], [88] or in the development process of new surgical methods, but 61% of the respondents have never used such a model for that purpose. Only 7.1% from the responders are regular users. Intraoperative 3D navigation can reduce intraoperative complications and morbidity rates [89]. More than half of the study participants (55%) use some type of navigation in their surgical practice and the rate of regular or occasional users of 3D printed navigation guides is 1.8% and 4.6% respectively. One of the advantages of 3D technologies, especially 3DP is that unique device andtools can be manufactured in a cost-effective way [90]. The claim for a specific, unique surgical instrument has been quite high in the survey population (28% of the surgeons would frequently need such a tool while 56.4% of them would occasionally need a unique, individually manufactured instrument). Implants manufactured by an advanced technique (e.g. 3DP) are regularly used by a minority of the surgeons (3.2%) and most of them (81.1%) have never used such a spinal implant. About forty percent (40.5%) of the responders have thought that these implants have got a possible advantage in challenging surgeries (e.g. tumor resections, special anatomical variations) and in individual, complex cases where patient specific implants would be required. On the other hand, 16.1% of the surgeons would use advanced manufactured implants in all instrumented spine surgeries providing a plausible better clinical outcome. Only 2.9% think that there is no need for such implants.

DOI:10.14753/SE.2020.2439

Table 5. Questions related to the acceptance of 3D technology

Characteristic	Score	N (%)
I/6: Are you familiar with the concept and the benefits of 3D printing/modelling technologies?		**282**
I don't have any specific knowledge	0	48 (17.0)
I have some general information from news, advertisements	1	117 (41.5)
I have read scientific papers/conference talks in the topic	2	65 (23.0)
I have already used some of these technologies	3	52 (18.4)
II/1: Have you ever used any 3D technology for education (or demonstration) for medical students, residents, colleagues?		**282**
never	0	130 (46.1)
occasionally, 3D virtual models	1	89 (31.6)
occasionally, 3D printed models	2	43 (15.2)
frequently, 3D virtual or printed models	3	20 (7.1)
II/2: Have you ever used 3D virtual models or printed models for surgical planning or for the development of a surgical technique (e.g. by demonstrating the difficult anatomical situation or the challenging surgical steps)?		**282**
never	0	172 (61.0)
occasionally	2	90 (31.9)
frequently	3	20 (7.1)
III/1: Intraoperative 3D navigation systems can reduce the complications and the morbidity of spinal surgeries. Do you use any 3D navigation system or tool in your clinical practice? *		**282**
not at al	0	127 (45.0)
occasionally (CT or fluoro based system)	1	84 (29.8)
regularly (CT or fluoro based system)	2	60 (21.3)
occasionally (3D printed surgical guide)	3	13 (4.6)
regularly (3D printed surgical guide)	4	5 (1.8)
III/4: Have you ever experienced or felt that a specific, unique surgical instrument (e.g. a particular chisel, curette or screwdriver) would have helped the surgery?		**282**
no	0	44 (15.6)
occasionally	1	159 (56.4)
frequently	2	79 (28.0)
IV/1: Have you ever used any advanced manufactured (3D printed) implant?		**280**
never	0	227 (81.1)
occasionally	2	44 (15.7)
frequently	3	9 (3.2)
IV/2: Where do you see the possible advantage of the use of advanced manufactured implants?		**279**
all implanted surgeries because a general or patient-specific advanced manufactured implant can provide better clinical outcome even in case of a standard pathology	4	45 (16,1)
challenging surgeries (e.g. tumor resection) and compromised anatomy or biology	3	113 (40,5)
only in complex cases where patient-specific implant would be required	2	113 (40,5)

none of the spinal surgeries	0	8 (2.9)
V/1: What do you think about the role of 3D printing/modelling technologies in spinal surgery?		**281**
no real future – too complicated and expensive	0	6 (2.1)
an option only for very limited applications, individual cases	2	123 (43.8)
a promising, feasible option for the near future	3	118 (42.0)
revolutionary	4	34 (12.1)

*Note: multiple choice

Over half of the spine surgical community believed that 3D technologies are a promising choice (42%) or will play a revolutionary (12.1%) role, based on the responses related to question V/1. However, 43.8% of the respondents consider it as an option with limited applications in individual cases. It is important to underline that only 2.1% of the spine surgeons have answered that 3D technology has no real future because it is too complicated and expensive. To understand the differing attitudes towards 3D technologies we investigated the acceptance score according to the AOSpine region affiliation, the field of spine surgery, experience in spine surgery (years of practice) and practice type (public, private, both).

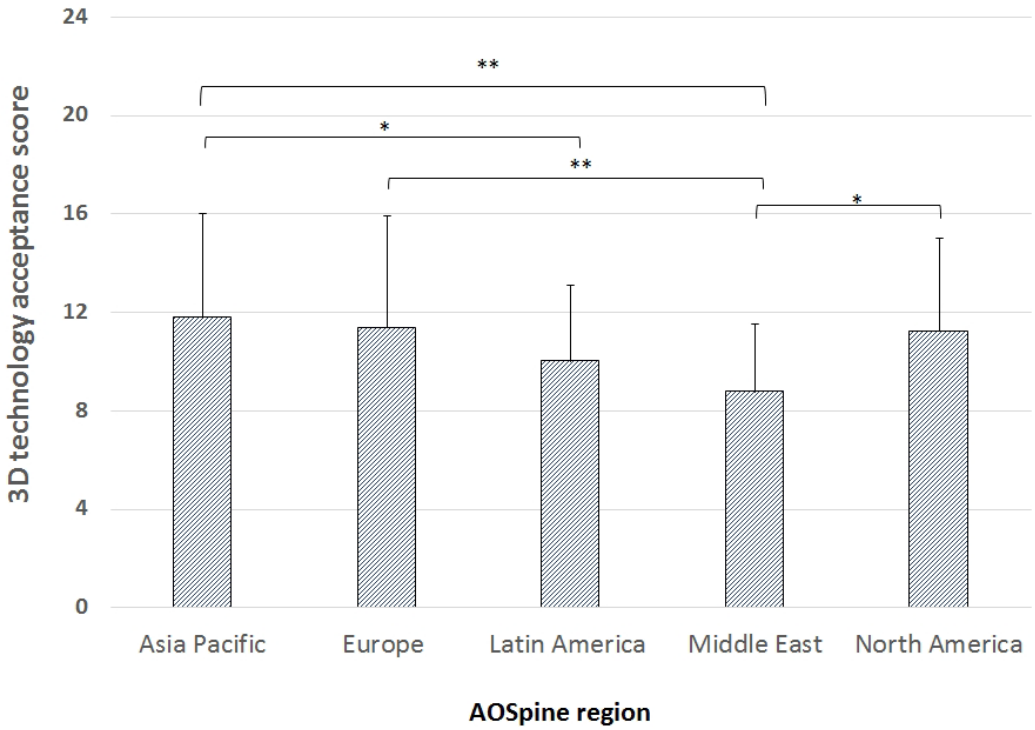

Figure 24. 3D technology acceptance scores according to the AOSpine regions. Significant differences were found between regions (*= $p \leq 0.05$, **= $p \leq 0.01$).

DOI:10.14753/SE.2020.2439

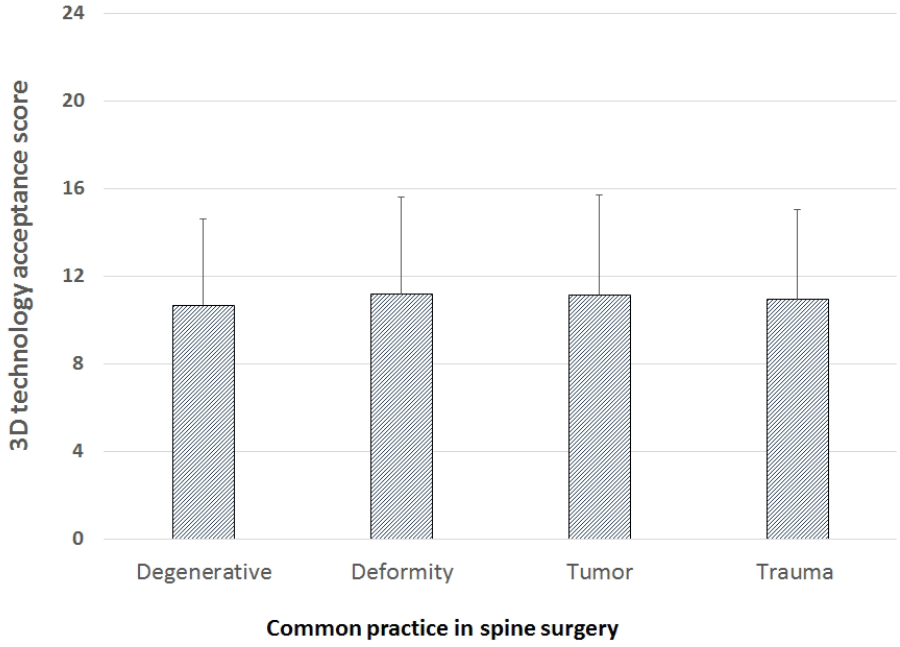

Figure 25. The field of spine surgery does not significantly influence the acceptance score (p= 0.77).

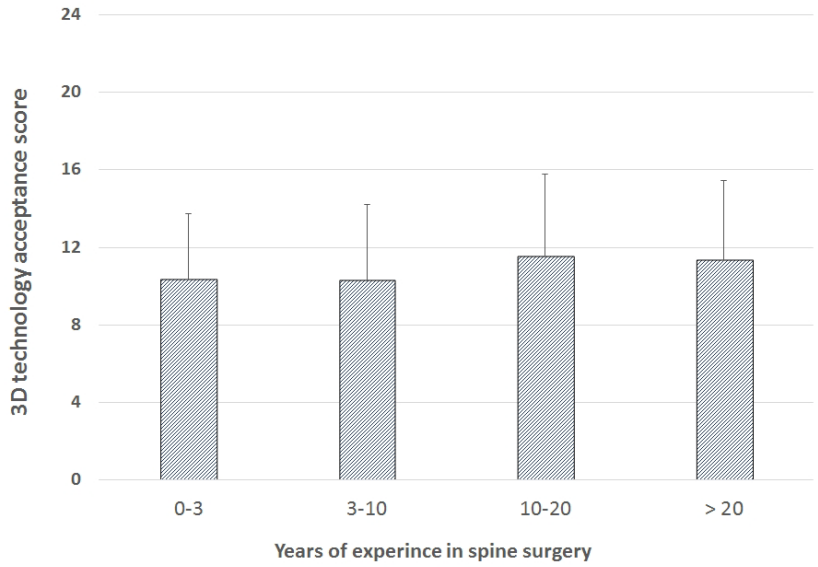

Figure 26. The surgical experience does not significantly influence the 3D technology acceptance score (p= 0.19).

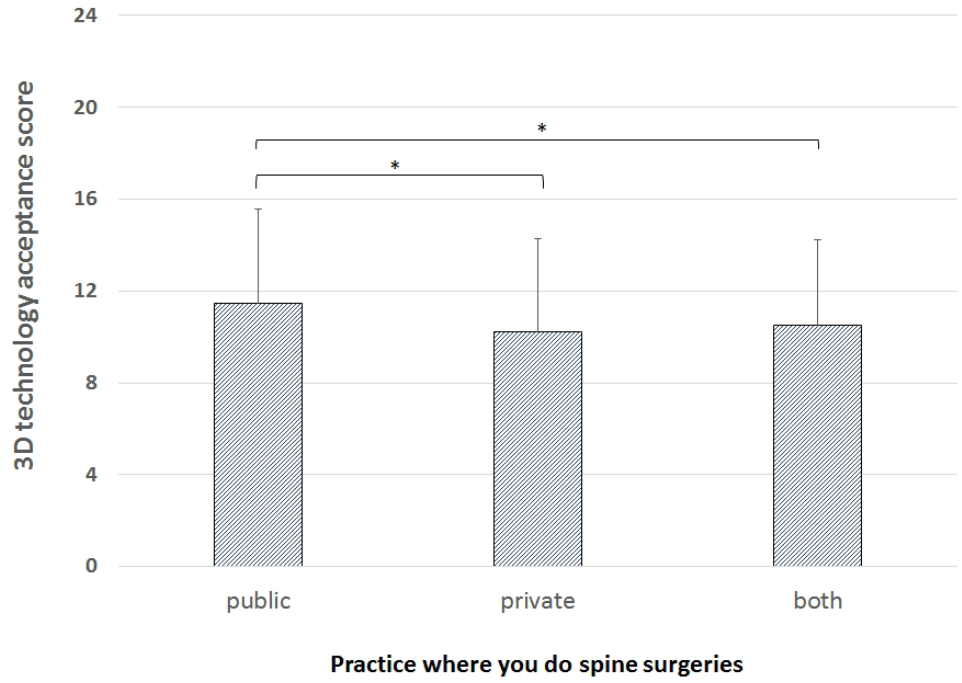

Figure 27. The 3D technology acceptance score is significantly higher among surgeons who perform their clinical activity exclusively in the public sector (*= $p \leq 0.05$). In the public group, the mean is 11.4±4.1 compared to the group of surgeons working only in the private sector (10.2±4.1, *p=0.026*) and to those having mixed praxis (10.5±3.8, *p=0.036*).

Figure 24 represents the comparison between the AOSpine regions. The highest acceptance was observed in the Asia-Pacific region (Mean±SD: 11.8±4.2), which has not differed significantly from Europe (11.4+4.5) or North America (11.2±3.8) regions, but it was significantly higher compared to Latin America (10.0±3.1, *p=0.028*) and to Middle East (8.8±2.8, *p=0.002*). We found no significant difference (p= 0.77) of the acceptance scores between the fields of spine surgery (**Figure 25**); nor (p= 0.19) when the subjects were grouped according to surgical experience in years (**Figure 26**). However, we revealed significantly higher acceptance scores among surgeons who perform their clinical activity exclusively in the public sector (**Figure 27**).

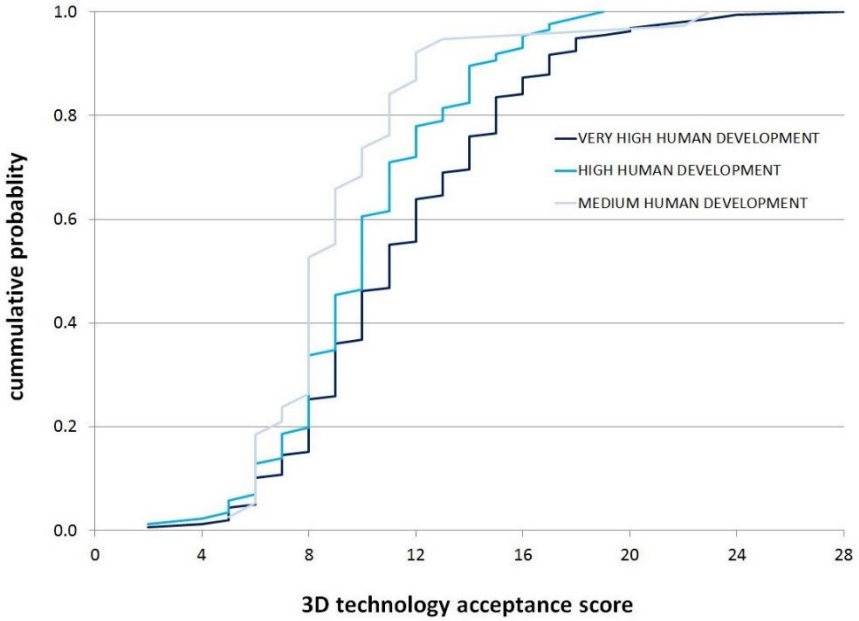

Figure 28. The influence of the HDI index on the 3D technology acceptance score is represented on the cumulative probability plot. The scores were the lowest for the medium development group, the leftward shift in the cumulative probability plot showing an increasing interest in the 3D technologies in higher developed countries. The difference reached the significance level for the medium vs very high, and high vs very high HDI groups (posthoc test between medium vs very high HDI: *p=0.0005*, and high vs very high HDI: *p=0.019*).

In this group, the mean score was 11.4±4.1 compared to the group of surgeons working only in the private sector (10.2±4.1, *p=0.026*) and to those having shared praxis (10.5±3.8, *p=0.036*). The influence of the HDI index on the acceptance score is represented on Figure 28 by a cumulative probability plot. The scores were the lowest for the medium development group, the leftward shift in the cumulative probability plot showing an increasing interest in the 3D technologies in the higher developed countries. However, the difference reached the significance level for the medium vs very high and high vs very high HDI groups (posthoc test between medium vs very high HDI: *p=0.0005*, and high vs very high HDI: *p=0.019*). In order to directly test this association, a correlation analysis was

performed between acceptance score and the HDI values as shown in **Figure 29** (Spearman test, ρ=0.37, *p=0.007*).

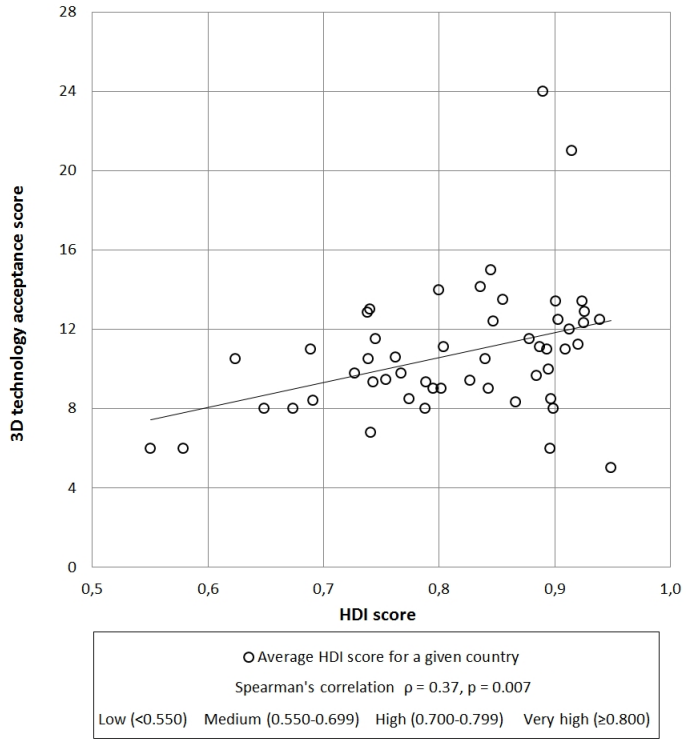

Figure 29. Positive correlation was found between the 3D technology acceptance score and the survey respondents residence country's HDI values (Spearman test, ρ=0.37, *p=0.007*)

Table 6. represents the questions related to the limitations, main obstacles in the wider spreading of these technologies. Answers to multiple choice questions revealed that most of the subjects, regardless of the AO region believe costs, lack of access and insufficient knowledge/expertise are limiting the frequent use of 3D technology in clinical/educational practice. When spine surgeons were asked about the reason for not using 3D navigation technologies the answers were similar: high purchasing and maintenance price, prolonged surgery time and recruitment of extra personnel. However, in this case we found a significant difference (*p=0.03*) between the AO regions. In Latin America, Middle-East and Asia-Pacific the high purchasing and maintenance cost, whereas in Europe the high purchasing price and complicated usage, were considered as the main limiting factors. The answers of North Americans point to the redundancy of these 3D navigational technologies in their praxis among the high costs.

DOI:10.14753/SE.2020.2439

Table 6. Limitations towards regular use of 3D technologies

	Global	Asia Pacific N (%)	Europe N (%)	Latin America N (%)	Middle East N (%)	North America N (%)	p**
II/3: What is the main barrier of the frequent use of such techniques in your clinical/educational practice? *							
no or limited knowledge about the possibilities and requirements	**98 (34.8)**	14 (25.0)	36 (35.6)	22 (31.9)	17 (56.7)	9 (34.6)	0.227
no or limited access to 3D modelling software	**116 (41.1)**	30 (53.6)	39 (38.6)	31 (44.9)	10 (33.3)	6 (23.1)	
no or limited access to 3D printing	**99 (35.1)**	16 (28.6)	42 (41.6)	24 (34.8)	11 (36.7)	6 (23.1)	
costs of 3D modelling/printing	**117 (41.5)**	23 (41.1)	43 (42.6)	26 (37.7)	13 (43.3)	12 (46.2)	
I am not interested in these technologies	**4 (1.4)**	1 (1.8)	3 (3.0)	0 (0.0)	0 (0.0)	0 (0.0)	
other	**11 (3.9)**	3 (5.4)	8 (7.9)	0 (0.0)	0 (0.0)	0 (0.0)	
III/2: If you are not using Intraoperative 3D navigation systems what is the reason? *							
lack of knowledge	**40 (14.2)**	3 (5.4)	7 (6.9)	18 (26.1)	10 (33.3)	2 (7.7)	0.029
high purchasing price	**107 (37.9)**	22 (39.3)	30 (29.7)	35 (50.7)	15 (50.0)	6 (23.1)	
high maintaining costs	**55 (19.5)**	13 (23.2)	16 (15.8)	14 (20.3)	10 (33.3)	3 (11.5)	
too complicated to use (longer surgery, need of a technician, etc)	**53 (18.8)**	9 (16.1)	26 (25.7)	9 (13.0)	4 (13.3)	5 (19.2)	
lack of confidence	**11 (3.9)**	3 (5.4)	4 (4.0)	2 (2.9)	1 (3.3)	1 (3.8)	
I do not see its necessity in my practice	**32 (11.3)**	3 (5.4)	16 (15.8)	5 (7.2)	1 (3.3)	7 (26.9)	
other	**10 (3.5)**	1 (1.8)	7 (6.9)	1 (1.4)	0 (0.0)	1 (3.8)	
IV/4: How do you see what is the main barrier of the spreading of advanced manufactured (3D printed) implants? *							
limited knowledge about the possibilities among the surgeons	**99 (35.1)**	13 (23.2)	38 (37.6)	21 (30.4)	14 (46.7)	12 (46.2)	0.327
limited access to 3D modelling and/or printing solutions	**144 (51.1)**	31 (55.4)	57 (56.4)	31 (44.9)	12 (40.0)	13 (50.0)	
high cost of modelling/printing	**162 (57.4)**	35 (62.5)	55 (54.5)	45 (65.2)	17 (56.7)	11 (42.3)	
unclear regulations	**53 (18.8)**	10 (17.9)	26 (25.7)	7 (10.1)	5 (16.7)	5 (19.2)	
lack of confidence, limited evidence	**54 (19.1)**	10 (17.9)	31 (30.7)	6 (8.7)	2 (6.7)	5 (19.2)	
other	**7 (2.5)**	1 (1.8)	6 (5.9)	0 (0.0)	0 (0.0)	0 (0.0)	
V/2: What do you think what are the main barriers of the spreading of 3D printing/modelling technologies? *							
"distance" between engineers and surgeons	**85 (30.1)**	20 (35.7)	32 (31.7)	16 (23.2)	9 (30.0)	8 (30.8)	0.627
"distance" between the hospital and the printing/designing facility	**80 (28.4)**	19 (33.9)	31 (30.7)	22 (31.9)	5 (16.7)	3 (11.5)	
surgeons are not aware of the possibilities provided by 3D printing/modelling	**116 (41.1)**	22 (39.3)	42 (41.6)	24 (34.8)	15 (50.0)	13 (50.0)	
expensive technology	**177 (62.8)**	36 (64.3)	56 (55.4)	48 (69.6)	20 (66.7)	17 (65.4)	
market are full with traditional solutions	**45 (16.0)**	7 (12.5)	24 (23.8)	10 (14.5)	2 (6.7)	2 (7.7)	
surgeons are not motivated to use advanced manufactured implants	**56 (19.9)**	15 (26.8)	20 (19.8)	11 (15.9)	8 (26.7)	2 (7.7)	
process of a patient-specific surgery are time-consuming	**64 (22.7)**	19 (33.9)	25 (24.8)	7 (10.1)	5 (16.7)	8 (30.8)	
other	**6 (2.1)**	3 (5.4)	6 (5.9)	3 (4.3)	1 (3.3)	1 (3.8)	

Majority of the spine surgeons identify the high cost of modeling/printing and limited access to 3D modeling and/or printing solutions as main obstacles in the extensive use of advanced manufactured (eg. 3D printed) implants. The insufficient knowledge and lack of confidence, little evidence about the possibilities of the 3D printing technologies/solutions were also selected as limiting factor. We found no significant difference in the proportion of answers according to the AO region affiliation of the respondents. Concerning the 3D technologies generally, most of the surgeons (62.8%) consider the technology too expensive and they are not well informed about its full potentials.

4.2. PART II. Investigation of the PCD surgical technique using 3D methods

4.2.1 Evaluation of the segmentation procedure

To evaluate the accuracy of our segmentation process we used the DSI for 6 randomly selected and postoperative geometries (**Table 7**). The obtained DSI values for both pre- and postoperative geometries were very high (preop: 0.96 ±0.02; postop 0.90 ±0.07, n = 6) and showed negligible variance, indicating a high accuracy of our segmentation method for all segmented geometries [91].

Table 7. Accuracy of the vertebra segmentation

preop			**postop**		
Patient ID	***Vertebra***	***DSI***	***Patient ID***	***Vertebra***	***DSI***
P01	L4	0.97	P01	L5	0.96
P02	L3	0.98	P02	L4	0.83
P04	L4	0.96	P05	L5	0.96
P06	L2	0.99	P07	L4	0.91
P08	L3	0.96	P08	L5	0.81
P09	L1	0.93	P09	T12	0.96
mean DSI 0.96 ±0.02			**mean DSI** 0.90 ±0.07		

DSI (Dice Similarity Index)

Next, for assessing the injected PMMA cement geometries we first evaluated the PMMA geometry distribution over the caudal vertebra endplate of the motion segments visually in 3D in the same view (**Figure 30**). Because the degenerative processes are not only age dependent but also depend on the musculoskeletal status of each patient, the features of intervertebral disc degeneration will be widely different. Accordingly, we found that the injected volumes are arranged patient-specifically to widely differing 3D shapes (**Figure 30**). Because of this large variance, the selection of representative volumes randomly is less likely; therefore, we chose to validate the segmentation process on all injected PMMA volumes instead. We calculated the DSI as above for the 16 segmented geometries (**Table 8**).

Table 8. Accuracy of the PMMA segmentation

Patient ID	*Treated Segment*	*DSI*
P01	L4-L5	0.90
	L2-L3	0.94
P02	L3-L4	0.91
	L4-L5	0.92
P03	L5-S1	0.89
P04	L3-L4	0.96
P05	L5-S1	0.95
P06	L1-L2	0.85
	L2-L3	0.97
P07	L3-L4	0.97
	L4-L5	0.90
P08	L3-L4	0.95
	L4-L5	0.96
P09	Th12-L1	0.94
	L1-L2	0.91
P10	L1-L2	0.96
mean DSI 0.93 ±0.035		

Again, the DSI values were very high for all segmented geometries (mean: 0.93±0.035, n =16) demonstrating the precision of our segmentation method also in case of the injected PMMA geometries.

4.2.2. Motion segments alignment evaluation

Having confirmed the precision of our segmentation process, we next evaluated the accuracy of the alignment of the pre-and postop motion segments by measuring HD values. The same processes were performed by two investigators. The HD values represent the maximal distance between two corresponding points (vertex) of the respective registered surface meshes. We obtained a mean HD value of 0.43±0.19 mm for the first investigator (I_1), and 0.54±0.16 mm for the second investigator (I_2). These values are considered by the field to be indicative of adequate fitting [92],**Table 9**. To obtain a detailed view on the precision of our alignment we created cumulative probability plots for the measured HD values for both investigators. We found that the maximal distance between the registered pre- and postop 3D geometries was almost always (90%) smaller than 2 mm, and ~70% of the values were smaller than 1 mm (**Figure 31)**. These measurements confirm the accuracy of registration/alignment methods. Consequently, the calculation of volumetric changes of the spinal canal, are expected to be similarly precise.

DOI:10.14753/SE.2020.2439

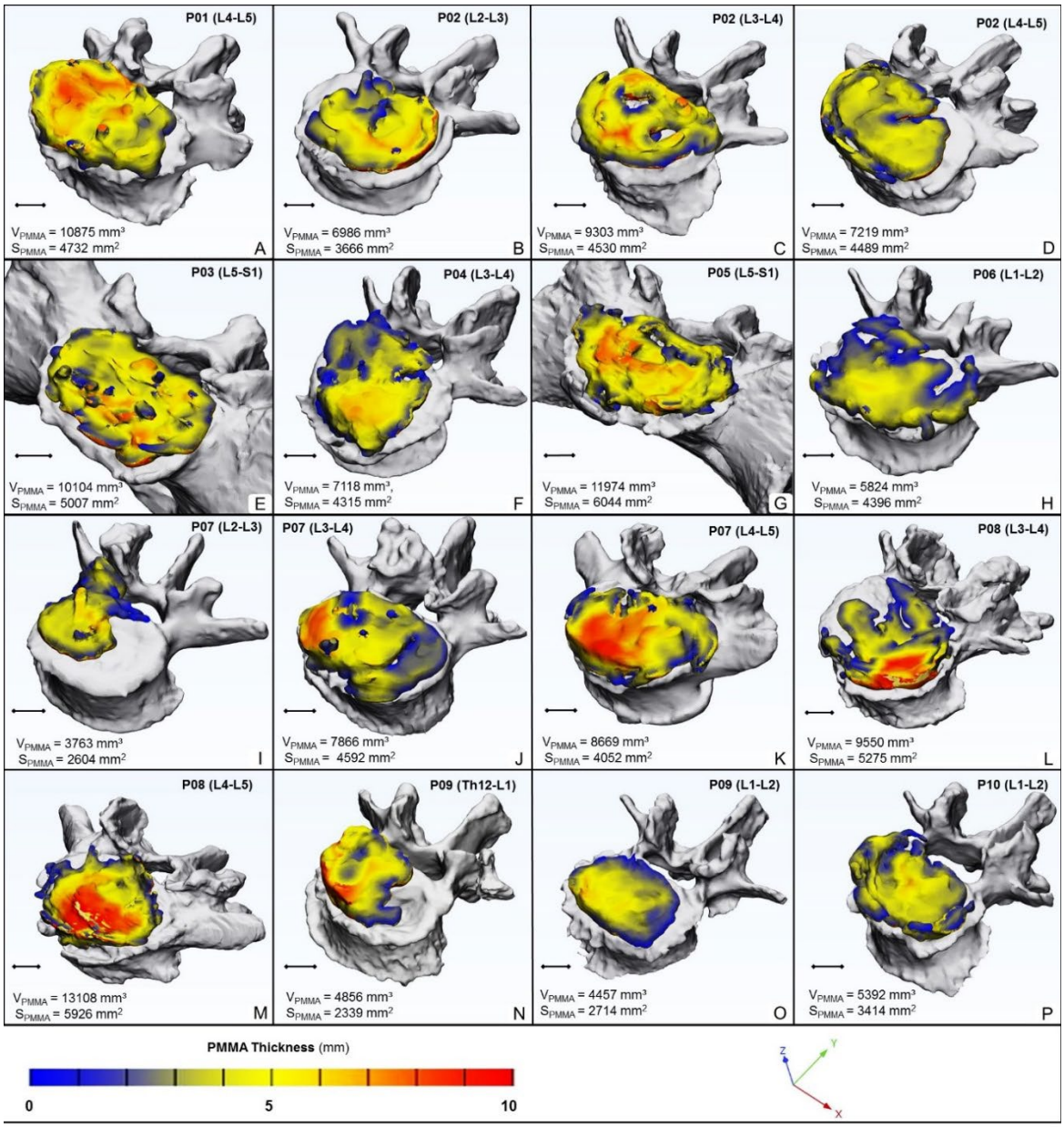

Figure 30. Visualization and thickness measurement of the PMMA geometry injected during PCD. **A-P** the PMMA geometry distribution over the caudal vertebral endplate of the investigated motion segment (the *xyz* coordinate system defines the view). The average volume is 7941.59±2749.82 mm³, and surface is 4256.02±1094.20 mm2. Thickness is represented by the colorbar 0-10 mm (Blue/Green/Red), scale bar 10 mm (**A-P**).

Table 9. HD values of the registration process

Patient ID	*Treated segment*	*Registred vertebra*	I_1 HD (mm)				I_2 HD (mm)			
			Min	*Max*	*Mean*	*RMS*	*Min*	*Max*	*Mean*	*RMS*
P01	L4-L5	L5	0	3.07	0.32	0.48	0	3.15	0.45	0.57
	L2-L3	L3	0	3.98	0.36	0.48	0	3.39	0.48	0.60
P02	L3-L4	L4	0	7.64	0.79	1.03	0	7.62	0.79	1.07
	L4-L5	L5	0	3.81	0.54	0.74	0	4.32	0.69	0.94
P03	L5-S1	S1	0	4.57	0.39	0.59	0	4.53	0.45	0.65
P04	L3-L4	L4	0	2.90	0.02	0.32	0	2.99	0.40	0.50
P05	L5-S1	S1	0	3.85	0.37	0.51	0	4.19	0.41	0.56
P06	L1-L2	L2	0	2.75	0.30	0.39	0	2.51	0.57	0.68
	L2-L3	L3	0	5.80	0.51	0.71	0	5.14	0.68	0.87
P07	L3-L4	L4	0	5.82	0.54	0.86	0	6.06	0.71	0.98
	L4-L5	L5	0	3.07	0.28	0.44	0	3.15	0.36	0.51
P08	L3-L4	L4	0	5.70	0.68	0.85	0	5.07	0.67	0.85
	L4-L5	L5	0	6.31	0.73	0.96	0	6.17	0.79	1.04
P09	Th12-L1	L1	0	3.14	0.36	0.49	0	2.94	0.35	0.47
	L1-L2	L2	0	3.80	0.27	0.38	0	3.76	0.38	0.51
P10	L1-L2	L2	0	2.72	0.43	0.60	0	2.88	0.47	0.67

HD (Hausdorff Distance, mm), I (Investigator), min (minimum), max (maximum), RMS (Root Mean Square)

4.2.3. PCD induced indirect decompression volumetric measurement

We measured the induced modification by defining the spinal canal geometry pre- and postop and calculating the volumetric change. For this, we created measurement cylinders -patient specifically- overlapping each preop and postop 3D geometries with impressions of the respective vertebral body, pedicules, facets and vertebral arches (see Materials and methods Section, **Figure 8**). We then quantified the indirect decompression effect as the subtracted volumes ΔV (ΔV = Vpostop - Vpreop). To test the accuracy and reproducibility of these measurements we involved two investigators (I_1 vs I_2) who performed the same procedures at two time points (T_1 vs T_2). We found that intra-rater reliability for I_1T_1 vs I_1T_2 was ICC=0.999 (IC 95%, Lower Bound=0.998, Upper Bound=1); for I_2T_1 vs I_2T_2 ICC=0.994 (IC 95%, Lower Bound=0.984, Upper Bound=0.998). The inter-

DOI:10.14753/SE.2020.2439

rater reliability for I_1(mean T_1, T_2) vs I_2 (mean T_1, T_2) was found: ICC=0.987 (IC 95%, Lower Bound=0.939, Upper Bound=0.996). These data indicate high accuracy and reproducibility of the volumetric change measurements. Data is summarised in the **Table 10, Table 11**.

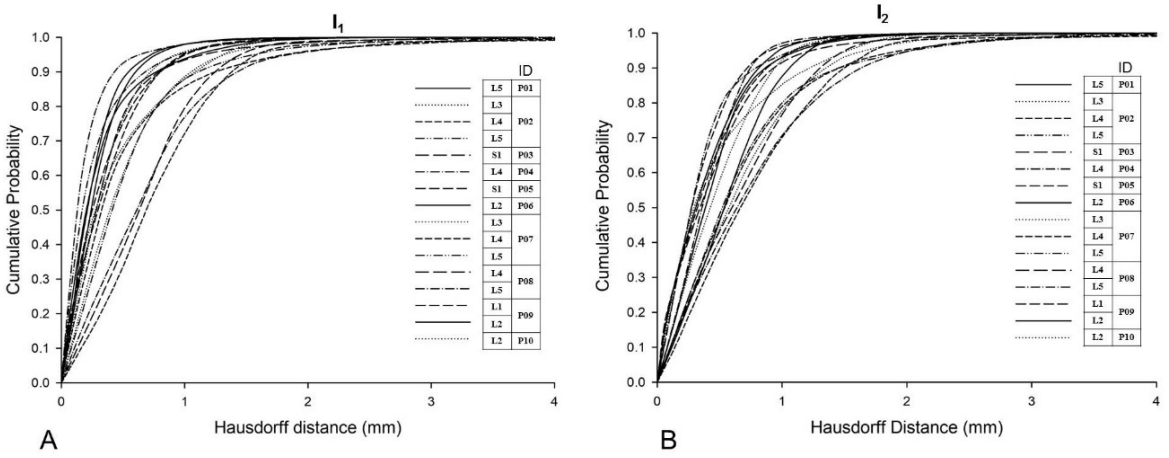

Figure 31. Distribution of HD values between the surface meshes of the registered vertebras. **A-B** Cumulative probability plots of HD values for preoperative and postoperative caudal vertebra models of the treated motion segments. Approximately 90% of HD values are <2 mm and ~80% < 1 mm for all I_1 registrations, and ~70% < 1 mm for all I_2 registrations (I, investigator).

DOI:10.14753/SE.2020.2439

Table 10. Volumetric measurements performed by the first investigator

Patient ID	Treated segment	Cylinder height (mm)	Cylinder radius (mm)	I_1T_1			I_1T_2		
				Subtracted cylinder volumes (preop mm³)	Subtracted cylinder volumes (postop mm³)	Δ volume (mm³)	Subtracted cylinder volumes (preop mm³)	Subtracted cylinder volumes (postop mm³)	Δ Volume (mm³)
P01	L4-L5	90	11	23481.77	26791.48	3309.71	23565.42	26981.21	3415.79
	L2-L3	90	10	22440.44	24220.51	1780.07	22386	24192.35	1806.35
P02	L3-L4	90	11	25998.95	29231.33	3232.38	25916.9	29135.09	3218.19
	L4-L5	90	10	18606.19	22116.6	3510.41	18961.63	22540.93	3579.3
P03	L5-S1	90	10	10557.01	14197.34	3640.33	10654.93	14258.86	3603.93
P04	L3-L4	90	12	30949.7	33164.51	2214.81	31221.81	33359.25	2137.44
P05	L5-S1	90	11	14871.04	18819.89	3948.85	14443.92	18421.84	3977.92
P06	L1-L2	90	10	21174.4	22652.73	1478.33	21137.92	22613.81	1475.89
	L2-L3	90	10	21320.77	22826.86	1506.09	21578.23	23034.73	1456.5
P07	L3-L4	90	10	20337.3	22892.13	2554.83	20406.59	22916.85	2510.26
	L4-L5	90	10	18704.32	21819.18	3114.86	18756.52	21833.27	3076.75
P08	L3-L4	90	11	24294.87	25606.03	1311.16	24028.83	25420.71	1391.88
	L4-L5	90	12	26848.94	30482.31	3633.37	26739.6	30439.9	3700.3
P09	Th12-L1	90	10	22608.27	23847.78	1239.51	22564.76	23873.82	1309.06
	L1-L2	90	10	22436.18	23014.5	578.32	21767.42	22316.17	548.75
P10	L1-L2	90	10	24099.99	24490.95	390.96	23999.63	24401.2	401.57

I (investigator), T (time point)

Table 11. Volumetric measurements performed by the first investigator

Patient ID	Treated segment	Cylinder height (mm)	Cylinder radius (mm)	I_2T_1			I_2T_2		
				Subtracted cylinder volumes (preop mm³)	Subtracted cylinder volumes (postop mm³)	Δ volume (mm³)	Subtracted cylinder volumes (preop mm³)	Subtracted cylinder volumes (postop. mm³)	Δ volume (mm³)
P01	L4-L5	90	11	23057.69	26796.4	3738.71	23099.09	26668.36	3569.27
	L2-L3	90	10	21812.04	23483.62	1671.58	22468.57	24159.33	1690.76
P02	L3-L4	90	11	25953.74	29151.15	3197.41	25939	28900.64	2961.64
	L4-L5	90	10	18677.31	22098.47	3421.16	18569.22	21943.59	3374.37
P03	L5-S1	90	10	10899.12	14372.15	3473.03	11071.42	14370.87	3299.45
P04	L3-L4	90	12	31147.28	33441.94	2294.66	31296.25	33473.92	2177.67
P05	L5-S1	90	11	14296.2	18270.97	3974.77	14222.07	17981.05	3758.98
P06	L1-L2	90	10	21032.8	22417.46	1384.66	21080.68	22418.56	1337.88
	L2-L3	90	10	21647.23	23146.92	1499.69	21777.41	23087.61	1310.2
P07	L3-L4	90	10	20548.06	22691.35	2143.29	20532.03	22715.41	2183.38
	L4-L5	90	10	18414.7	21475	3060.3	18066.85	20903.98	2837.13
P08	L3-L4	90	11	23821.27	24633.23	811.96	23806.12	24606.98	800.86
	L4-L5	90	12	26162.06	28985.67	2823.61	26883.45	30189.36	3305.91
P09	Th12-L1	90	10	22599.85	23670.88	1071.03	22750.69	23736.31	985.62
	L1-L2	90	10	22614.97	23091.49	476.52	22334.28	22890.83	556.55
P10	L1-L2	90	10	24061.54	24454.58	393.04	24025.81	24442.8	416.99

I (investigator), T (time point)

We then, determined the actual volumetric change (ΔV) of the spinal canal in the PCD-treated motion segments as $(I_1T_1+I_1T_2+I_2T_1+I_2T_2)/4$. The distribution of the actual volumetric change is presented in **Figure 32**. The volumetric changes widely differ, similarly to the shape of the injected volumes (**Figure 30**). The observed geometrical change (mean=2266.50, SD=1172.19, n=16) between the preop and postop measurement cylinder volumes demonstrates significant difference (Vpostop vs Vpreop., *p<0.0004*, Paired Wilcoxon signed rank test, **Figure 32**), meaning that PCD caused a significant increase of the volume of the spinal canal.

4.2.4. PMMA geometry effect on the volumetric change (ΔV) of the spinal canal

We next tested how the geometry of the injected PMMA relates to the observed volumetric change. We found significant, strong, positive correlation between the volume of the injected PMMA and the ΔV of the spinal canal (*correlation coefficient* (ρ)=0.762, *p=0.001*) (**Figure 33)**. The surface area of the discoplasty showed a significant and strong, positive correlation (ρ=0.668, *p=0.005*) the volumetric change of the spinal canal.

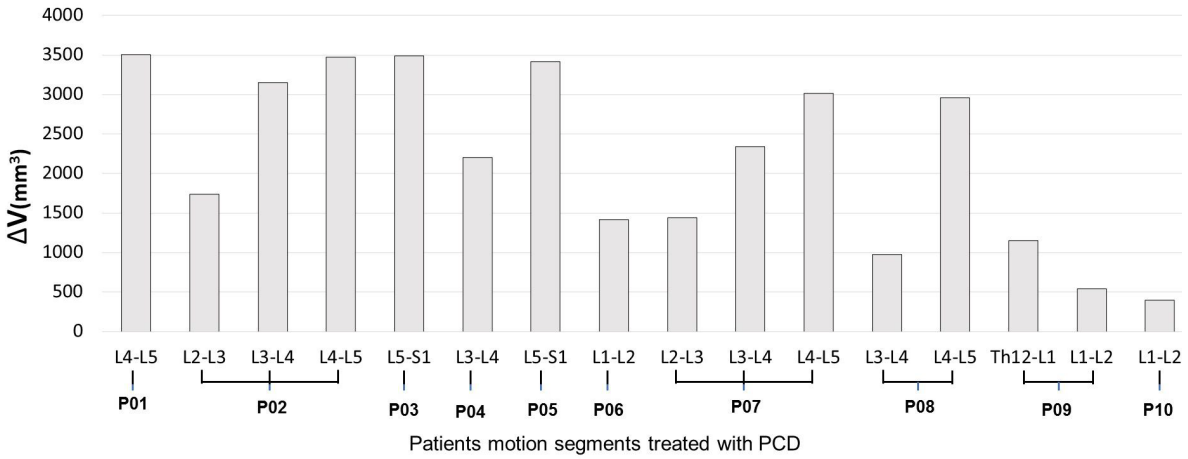

Figure 32. Distribution of PCD induced mean volumetric change (ΔV) of the spinal canal. An average of 2266.50± 1172.19 mm³ volumetric increase was measured (16 PCD treated segments, n = 10 patients.). We found a significant geometrical change between the mean preop and postop spinal canal volume (Vpostop vs Vpreop, p=0.0004).

A significant and moderate [93], negative correlation (ρ= -0.535, *p=0.033*) was found between the PMMA surface-volume ratio (SF:V) and the volumetric change of the spinal

canal. These data indicate that the volume and surface area of the injected PMMA are the most predictive regarding the extent of the expected indirect spinal decompression.

4.2.5. Clinical outcome

To test the clinical effect of the indirect decompression we used the patient- reported outcome questionnaire Oswestry Disability Index (ODI) and visual analogue scale (VAS) for leg pain (LP) and low back pain (LBP). The ODI and LP, LBP significantly decreased 6 months after the PCD procedure (*p=0.013; p=0.036; p=0.015*; respectively, **Table 12**), and as such reflecting significant amelioration of our patients' pain intensity after PCD procedure . In order to find a predictive measure of clinical improvement we analysed the association of the volumetric change of the spinal canal and ODI, LP and LBP. We found only weak, negative, but non-significant correlation between the change of the ODI and ΔV (ρ=-0.321, p=0.365), indicating clinical improvement regardless of the indirect decompression volume. However, the correlation between the change of the LP, LBP and ΔV (ρ=0.772, *p=0.009*; ρ=0.693, *p=0.026*, respectively) (**Figure 33)** was significant, strong and positive. This indicates a volume dependent amelioration of patient symptoms, with a higher injected volume resulting in better patient outcome.

DOI:10.14753/SE.2020.2439

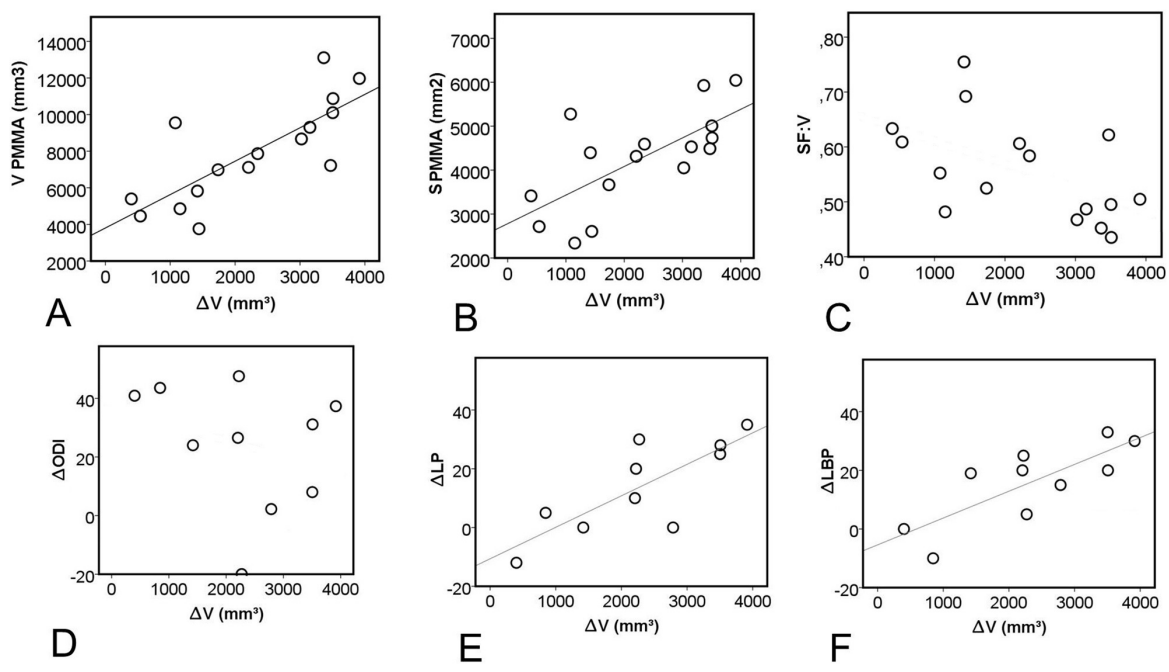

Figure 33. Association of the mean volumetric change (ΔV) of the spinal canal induced by the PCD with the PMMA volume, surface, surface-volume ratio (SF: V) and with the clinical outcome (ODI, LP, LBP). **A, B** we found significant positive correlation between the PMMA volume, PMMA surface and ΔV (ρ=0.762, *p=0.001* and ρ=0.668, *p=0.005*,). **C** the correlation between SF: V and ΔV although moderate, was found to be significantly negative (ρ=-0.535, *p=0.033*). **D** The negative, weak correlation was found not to be significant between the change of the ODI and ΔV (ρ=-0.321, p=0.365). **E, F** positive, significant and strong correlation was found between the ΔLP, ΔLBP and ΔV (ρ=0.772, *p=0.009*, and ρ=0.693, *p=0.026* respectively). For **D, E, F** a patient averaged ΔV was used for patients who underwent multiple segment PCD.

DOI:10.14753/SE.2020.2439

Table 12. Preop, and postop 6-month follow-up results of patient reported outcome questionnaires

Patien ID	preop			postop (6m FU)			Δ (preop- postop 6m FU)		
	ODI	LP	LBP	ODI	LP	LBP	ODI	LP	LBP
P01	71.11	55	70	40.00	27	50	31.11	28	20
P02	68.89	60	40	66.67	60	25	2.22	0	15
P03	50	75	80	42.00	50	47	8.00	25	33
P04	66.67	60	80	40.00	50	60	26.67	10	20
P05	73.33	82	80	36.00	47	50	37.33	35	30
P06	46	60	60	22.00	60	41	24.00	0	19
P07	37.8	70	70	57.78	40	65	-20.00	30	5
P08	75.56	50	70	28.00	30	45	47.56	20	25
P09	75.56	75	80	32.00	70	90	43.56	5	-10
P10	68.89	30	80	28.00	42	80	40.89	-12	0
Average±SD	63.37±13.6	61.7±18	71±13	39.24±13.8	47.6±14	55±19	24.13±21.4	14±16	15.7±14

FU (follow-up), ODI (Oswestry Disability Index), VAS (visual analogue scale), LP (leg pain), LBP (low back pain), SD (standard deviation)

4.3. PART III. Investigation of the "Closed Loop" lumbo-sacral reconstruction technique using 3D methods

4.3.1. Locomotor biomechanics

The patient was able to walk independently with minor gait alterations to compensate lost neural functions **Figure 34**. During the FU no radiological sign of implant failure was registered. The gait was slow and asymmetric with more support on the left side. Joint mobility was close to the normative data in all joints, distally in particular. A forward leaning of 20° was seen at the level of the pelvis and trunk throughout the gait cycle. Adduction moments increased at the hip on both sides while joint moments decreased at the knee. Joint power analysis showed a decrease in propulsion power at the hip and ankle.

DOI:10.14753/SE.2020.2439

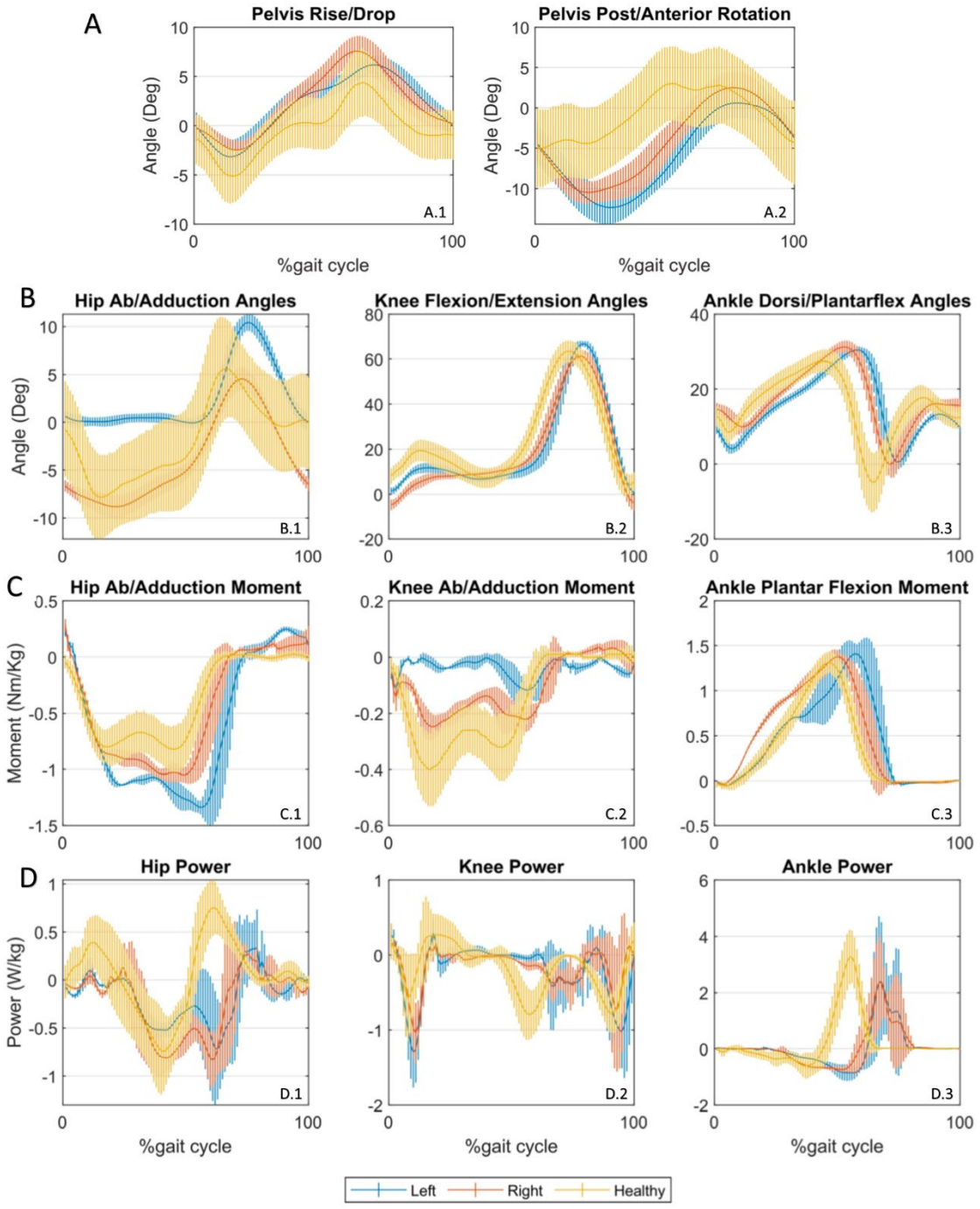

Figure 34. Gait evaluation at 5 years after total sacrectomy. Time-series Kinematics (**A**, **B**) and Kinetics (**C, D**) of the pelvis, hip, knee and ankle compared to healthy subjects. The data was normalized to 100% of the gait cycle, kinetic data was normalized to body weight. Vertical lines along the curves indicate the standard deviation. Positive values correspond to pelvic hike (**A.1**), pelvis posterior rotation (**A.2**), hip abduction (**B.1**), knee flexion (**B.2**), ankle dorsiflexion **(B.3)**, hip and knee abductor moments **(C.1,2)** and ankle plantar flexor moment (**C.3**). Plots in (**D**) indicate the joint power in the hip, knee and ankle during flexion/extension.

4.3.2. Evaluation of the segmentation procedure

To evaluate the accuracy of our segmentation process we used the DSI for the 12 CT scan - based implant construct and left iliac bone geometry **(Table 13)**. The obtained DSI values for the implant construct geometries were very high 0.97 ±0.02 (n=12) as well as for the iliac bone 0.96 ±0.05 (n = 12) and showed negligible variance, indicating a high accuracy of our segmentation method for all segmented geometries [91].

4.3.3. Alignment evaluation

Having confirmed the precision of our segmentation process, we next evaluated the accuracy of the alignment of the iliac bones to the first postop iliac bone geometry by measuring HD values. We obtained a mean HD value of 0.63±0.14 mm (**Table 14**). The HD was determined for the iliac screw bodies by comparing to the first postop geometry (**Table 15**) and it resulted in a mean value of 0.95±0.10 mm. These values are considered by the field to be indicative of adequate fitting [92]**.** After the iliac bone alignment in order to demonstrate the colinear and coincident position of the iliac screw axis, we visualised the geometric overlap of the iliac screws body's in **Figure 35**. The figure demonstrates that the screw body does not deform or change its position in the new common coordinate system. Theoretically any point in this two screw body geometries can be used as a reference point in a measurement process.

DOI:10.14753/SE.2020.2439

Table 13. Evaluation of the accuracy of the segmentation process

No. CT	DSI implant construct I_1 vs I_2	DSI iliac bone I_1 vs I_2
1	0.95	0.96
2	0.98	0.96
3	0.99	0.96
4	1.00	0.97
5	1.00	0.96
6	0.99	0.97
7	0.84	0.96
8	0.99	0.96
9	0.99	0.96
10	0.98	0.97
11	0.96	0.96
12	1.00	0.97
	mean DSI= 0.97±0.05	mean DSI= 0.96±0.05

CT (Computed Tomography), DSI (Dice Similarity Index), I (Investigator), T (time point)

Table 14. Iliac bone alignment accuracy evaluation

No. of the compared iliac bone geometry	Hausdorff Distance [mm]			
	min	**max**	**mean**	**RMS**
1-2	0.00	3.23	0.50	0.66
1-3	0.00	5.30	0.72	0.98
1-4	0.00	3.82	0.54	0.70
1-5	0.00	3.16	0.57	0.75
1-6	0.00	4.33	0.78	0.99
1-7	0.00	3.72	0.47	0.64
1-8	0.00	5.67	0.49	0.71
1-9	0.00	3.65	0.52	0.67
1-10	0.00	4.69	0.83	1.06
1-11	0.00	4.77	0.80	1.03
1-12	0.00	5.01	0.67	0.87
mean ±SD	**0.00**	**4.30±0.85**	**0.63±0.14**	**0.82±0.16**

RMS (Root Mean Square), min (minimum), max (maximum), SD (standard deviation)

DOI:10.14753/SE.2020.2439

Table 15. Iliac screws body's alignment accuracy evaluation

No. of the compared iliac screw body's geometry	Hausdorff Distance [mm]			
	min	max	mean	RMS
1-2	0.00	2.28	0.92	1.11
1-3	0.00	3.29	0.96	1.27
1-4	0.00	2.98	0.95	1.16
1-5	0.00	2.90	1.02	1.24
1-6	0.00	3.14	1.03	1.24
1-7	0.00	4.25	0.90	1.20
1-8	0.00	2.94	0.91	1.11
1-9	0.00	4.74	0.92	1.26
1-10	0.00	3.79	1.18	1.42
1-11	0.00	3.21	0.78	1.00
1-12	0.00	3.35	0.85	1.09
mean ±SD	**0.00**	**3.35±0.68**	**0.95±0.10**	**1.19±0.11**

RMS (Root Mean Square), min (minimum), max (maximum), SD (standard deviation)

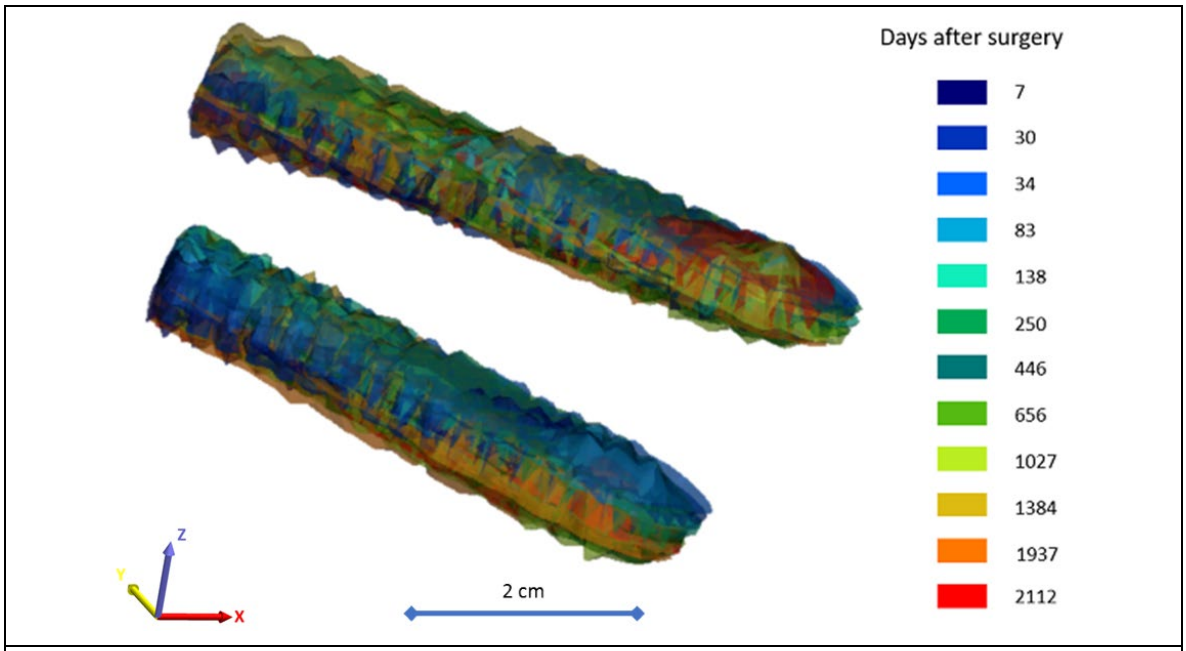

Figure 35. Geometric overlap of the iIliac screws body's after the alignment process. The 12 postop CT scan-based surface mesh representing the iliac screw bodies are color coded corresponding to the scale bar (color= CT scan session +number of days after surgery). The surfaces mesh is visualized with 75% transparency.

4.3.4. Implant deformation

We defined the implant deformation by measuring the distance in the three planes between the right LII pedicle screw tip and the left caudal iliac screw tip. The measurements were performed by three investigators at two different time points (I_1,I_2,I_3,T_1,T_2) **Table 16, 17, 18**. The mean change in the dimensions compared to the first post op CT was ΔX_d=7.27±2.80 mm for the frontal plane, ΔY_d=8.24±2.51 mm for the coronal plane, ΔZ_d= 10.15±2.97 mm for the sagittal plane. To test the accuracy and reproducibility of these measurements we performed inter- and intrarater reliability test by calculating the intraclass correlation coefficient (ICC) based on the $3D_d$ values, presented in **Table 19**. With exception for the I_1T_1 vs I_1T_2 intra-rater reliability the ICC was 0.768, however this value indicates good reliability, in other cases excellent reliability was achieved [94]. The association between the average X_d/Y_d/Z_d measurement and the number of days after surgery is shown in **Figure 36**. The implant construct deformation can be registered in the anatomical planes over the postop follow up period, however only in the sagittal plane was significant negative, strong correlation between the Z_d and the number of days after surgery (ρ=-0.664, p=0.018). This result demonstrates the forward bending tendency of the construct.

DOI:10.14753/SE.2020.2439

Table 16. Deformation measurements performed by the first investigator

No. CT	I_1T_1				I_1T_2			
	X_d (mm)	Y_d (mm)	Z_d (mm)	$3D_d$ (mm)	X_d (mm)	Y_d (mm)	Z_d (mm)	$3D_d$ (mm)
1	87.24	13.89	165.43	187.54	84.58	13.45	165.39	186.25
2	92.78	8.99	163.54	188.24	93.73	8.97	161.34	186.81
3	91.32	8.80	158.86	183.45	91.02	10.12	158.14	182.74
4	99.72	11.39	154.62	184.34	97.62	3.04	153.00	181.52
5	96.41	4.63	155.62	183.12	96.57	6.50	154.38	182.21
6	96.60	6.20	153.12	181.15	97.10	4.65	156.34	184.10
7	89.57	4.90	159.27	182.79	91.33	3.75	157.81	182.37
8	93.29	2.38	155.89	181.69	92.81	2.24	157.26	182.62
9	89.31	5.83	157.35	181.02	90.15	6.61	157.29	181.41
10	95.57	6.01	152.24	179.85	99.93	9.12	152.26	182.35
11	93.46	8.14	155.47	181.58	94.21	7.59	155.48	181.95
12	96.40	11.72	151.24	179.73	98.76	10.10	150.81	180.55
mean	**93.47**	**7.74**	**156.89**	**182.88**	**93.98**	**7.18**	**156.63**	**182.91**
±SD	3.65	3.38	4.31	2.72	4.35	3.36	4.00	1.90

CT (Computer Tomography), I (Investigator), T (time point), Xd (distance in the coronal plane), Yd (distance in the axial plane), Zd (distance in the sagittal plane), 3Dd (three-dimensional distance), SD (standard deviation)

Table 17. Deformation measurements performed by the second investigator

No. CT	I_2T_1				I_2T_2			
	X_d (mm)	Y_d (mm)	Z_d (mm)	$3D_d$ (mm)	X_d (mm)	Y_d (mm)	Z_d (mm)	$3D_d$ (mm)
1	87.64	17.17	165.95	188.45	87.44	16.13	167.12	189.30
2	94.33	12.37	160.53	186.60	92.69	8.66	161.93	186.78
3	89.70	8.70	159.97	183.61	92.12	10.23	159.65	184.60
4	97.19	2.26	154.68	182.69	96.50	3.01	154.60	182.27
5	96.50	6.67	155.58	183.20	95.77	5.86	155.66	182.86
6	96.35	5.73	154.93	182.54	96.68	5.06	154.06	181.95
7	91.43	4.17	158.61	183.12	91.74	3.36	159.10	183.69
8	92.75	2.48	157.15	182.50	92.62	2.56	157.11	182.40
9	91.05	8.19	157.49	182.10	89.83	4.72	158.27	182.05
10	96.44	5.19	154.03	181.80	96.54	4.66	153.69	181.56
11	93.43	7.40	154.88	181.03	93.78	7.47	155.25	181.53
12	95.55	9.27	151.71	179.53	95.52	9.29	151.68	179.49
mean	**93.53**	**7.47**	**157.13**	**183.10**	**93.44**	**6.75**	**157.34**	**183.21**
±SD	3.07	4.21	3.78	2.37	2.93	3.88	4.23	2.63

CT (Computer Tomography), I (Investigator), T (time point), Xd (distance in the coronal plane), Yd (distance in the axial plane), Zd (distance in the sagittal plane), 3Dd (three-dimensional distance), SD (standard deviation)

Table 18. Deformation measurements performed by the third investigator

No. CT	I_3T_1				I_3T_2			
	X_d (mm)	Y_d (mm)	Z_d (mm)	$3D_d$ (mm)	X_d (mm)	Y_d (mm)	Z_d (mm)	$3D_d$ (mm)
1	87.63	16.26	167.23	189.50	86.87	15.63	167.36	189.21
2	93.24	9.86	161.12	186.42	92.89	9.29	160.84	185.97
3	92.38	10.25	160.20	185.21	92.24	10.33	158.73	183.88
4	97.74	4.84	155.48	183.71	97.19	3.27	154.88	182.88
5	96.65	5.85	154.66	182.47	97.18	7.60	156.05	183.99
6	96.68	5.54	153.71	181.67	96.00	4.14	154.45	181.90
7	91.39	4.34	158.59	183.09	90.47	3.76	160.09	183.92
8	92.13	2.81	156.67	181.77	92.68	3.00	157.16	182.48
9	88.83	6.77	158.29	181.64	88.62	6.38	159.43	182.52
10	96.48	5.66	153.08	181.04	95.64	4.84	153.88	181.24
11	93.34	8.05	155.51	181.55	93.05	7.91	155.54	181.42
12	97.45	10.53	150.92	179.96	96.94	10.53	152.23	180.78
mean	**93.66**	**7.56**	**157.12**	**183.17**	**93.31**	**7.22**	**157.55**	**183.35**
±SD	3.39	3.68	4.36	2.69	3.43	3.78	4.08	2.35

CT (Computer Tomography), I (Investigator), T (time point), Xd (distance in the coronal plane), Yd (distance in the axial plane), Zd (distance in the sagittal plane), 3Dd (three-dimensional distance), SD (standard deviation)

4.3.5. BMD mapping at the fusion site

The bone material density distribution in the region of interest for the fusion process was measured over the follow up period, **Figure 37**. The colour map captures the bone remodelling process in the ROI. After the second year FU a solid fusion was detected between the lumbar spine LV vertebra and the two iliac bones, however due to the cyclical loading the bone remodelling represented by the change in the element distribution in the colour coded BMD categories still continues. The change in the volume of the BMD categories over the days after surgery is presented in **Figure 38**. The 3D contour plot demonstrates an increase in the high BMD category volume after the second year FU.

DOI:10.14753/SE.2020.2439

Table 19. Results for the two-way mixed absolute agreement calculation for ICC

	ICC	95% Confidence Interval	
		Lower Bound	Upper Bound
intra-rater reliability			
I_1T_1vsI_1T_2	0.768	0.362	0.928
I_2T_1vsI_2T_2	0.980	0.934	0.994
I_3T_1vsI_3T_2	0.949	0.838	0.985
inter-rater reliability			
I_1vsI_2vsI_3	0.980	0.948	0.994

ICC (intraclass correlation), I (Investigator), T (time point)

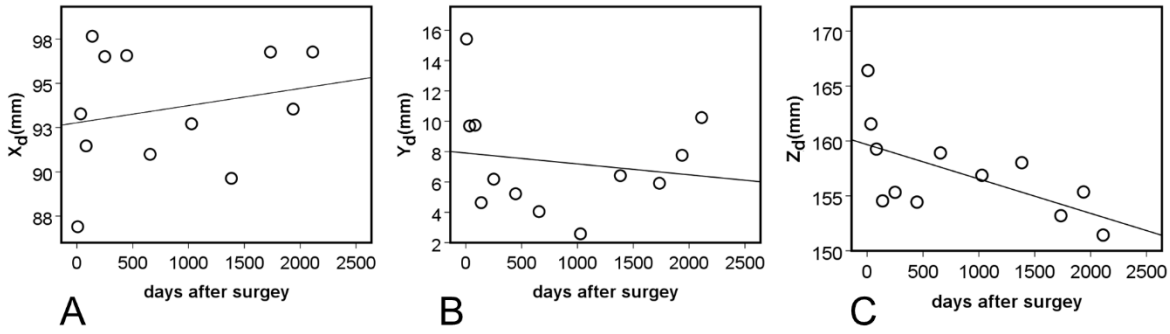

Figure 36. Association between the distance of the mobile (LII right pedicle screw tip) point from the fixed point (left, caudal trans iliac screw tip) in the anatomical planes, and and the number of days after surgery (DAS). **A** nonsignificant positive, moderate correlation was found between the X_d (frontal plane) and DAS (ρ=0.336, p=0.286). **B** nonsignificant, negative, weak correlation was found between the Y_d (axial plane) and DAS (ρ=-0.182, p=0.572). **C** significant negative, strong correlation was found between the Z_d (sagittal plane) and the number of days after surgery (ρ=-0.664, p=0.018).

DOI:10.14753/SE.2020.2439

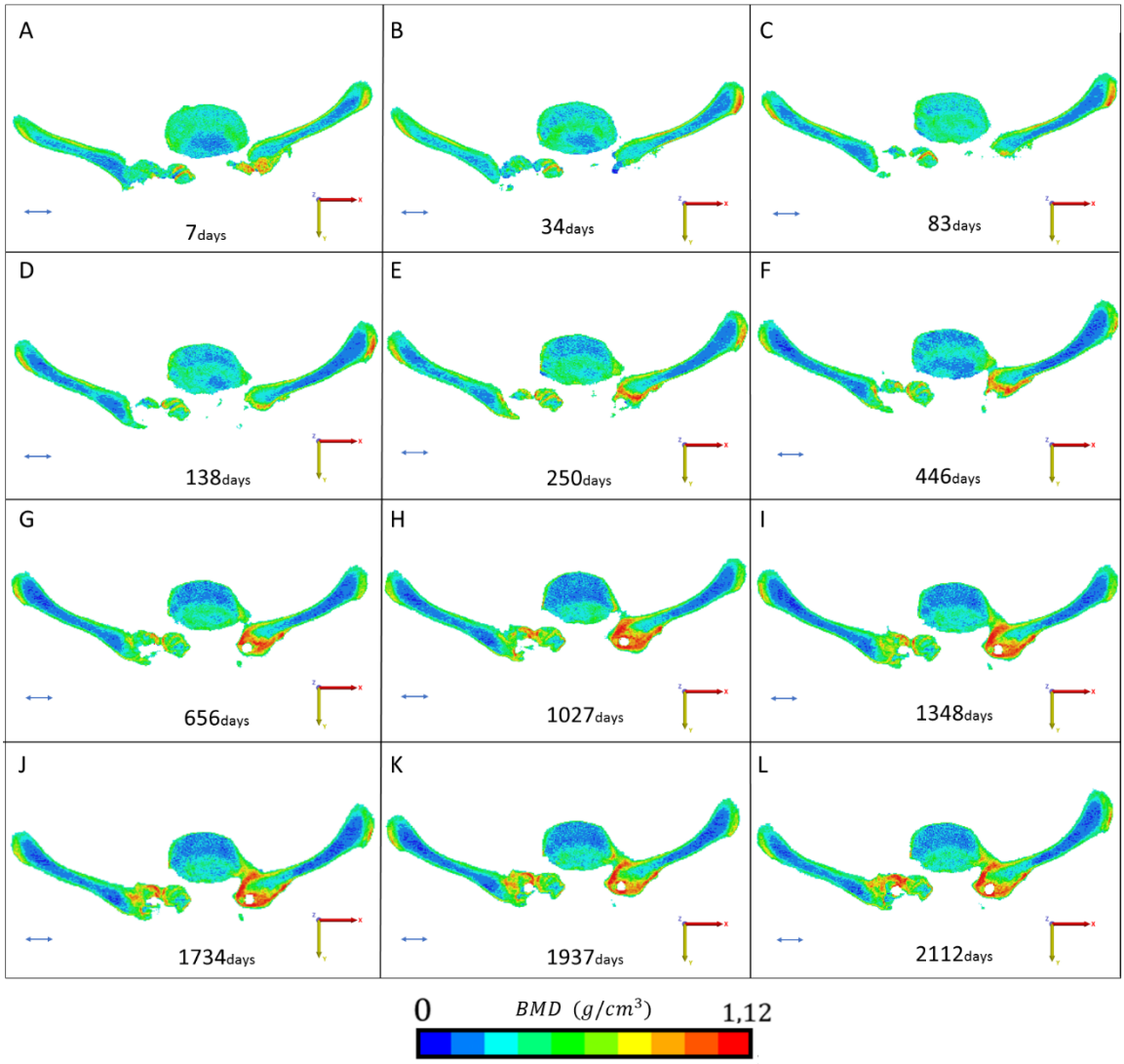

Figure 37. Mapping of the fusion and remodeling process. **A-L**. The figures represent the region of interest for the 12 postop CT scans (from 7 to 2112 days). The BMD values are represented in ten color codes from 0 to 1.12 g/cm^3 in a RGB scale. Red color represents the strongest bone tissue.

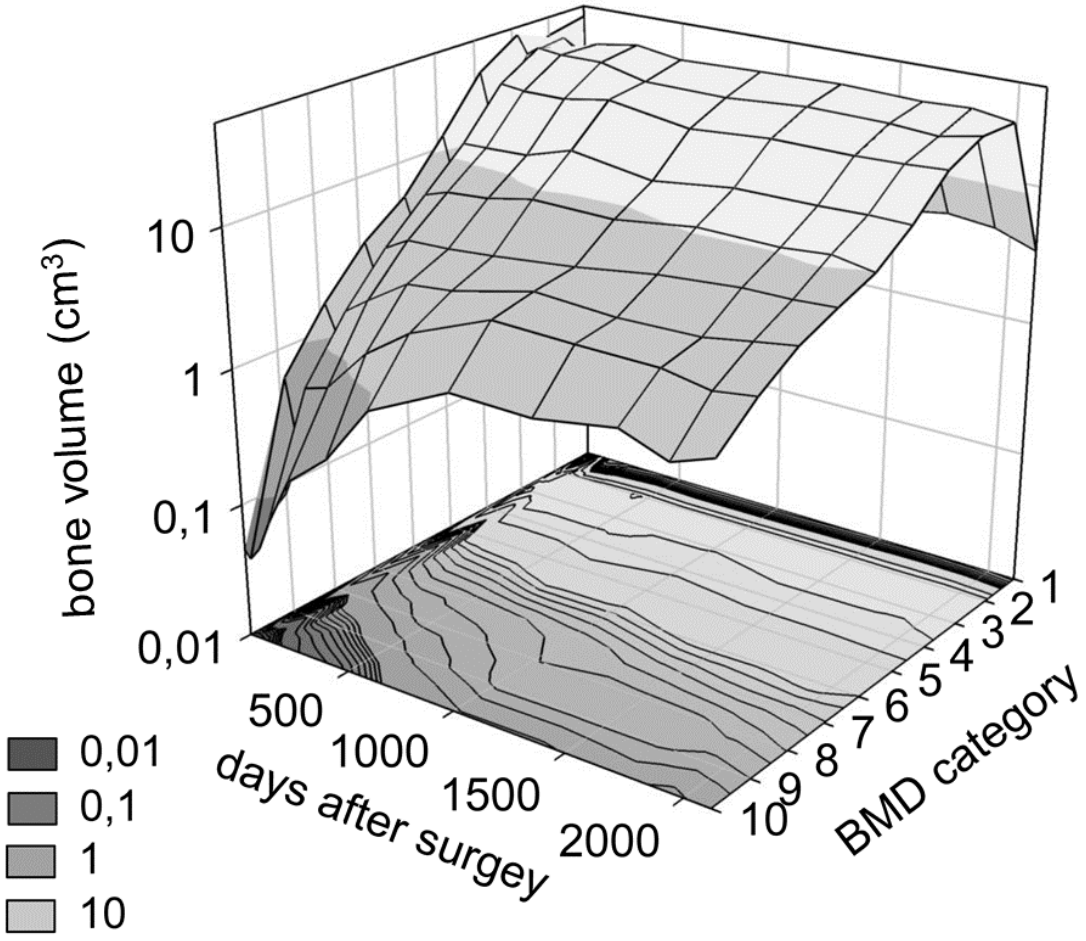

Figure 38. Distribution of the bone volume in the 10 BMD category over the follow up period. The bone volume is defined using the FE mesh voxel dimensions. The BMD categories from 1 to 10 correspond to the color code from **Figure 37** (1st category =0 g/cm^3, 10th category 1.12 g/cm^3).

4.4. PART IV. Integration of the 3DP physical models in spine care

4.4.1 Comparison of the FDM and DLP 3D printing technologies

Geometrical differences between the surface meshes printed by the two 3D printing methods are represented by the calculated the Hausdorff Distance (HD) values between the aligned surfaces (FDM_{sup}, FDM_{inf}, DLP_{sup}, DLP_{inf}) and the FVM (**Table 20**).

Table 20. The HD measurement represents the difference between the aligned/registered surfaces and the input geometry for 3D printing (FVM)

	I_1								I_2							
	T_1				T_2				T_1				T_2			
	HD (mm)				HD (mm)				HD (mm)				HD (mm)			
	min	max	mean	RMS	min	max	mean	RMS	min	max	mean	RMS	min	max	mean	RMS
FDM_{sup}	0.00	0.82	0.11	0.14	0.00	0.81	0.17	0.23	0.00	0.68	0.13	0.16	0.00	1.05	0.27	0.35
FDM_{inf}	0.00	0.85	0.23	0.28	0.00	0.56	0.13	0.15	0.00	0.64	0.16	0.19	0.00	0.73	0.22	0.26
DLP_{sup}	0.00	1.29	0.20	0.26	0.00	1.33	0.18	0.23	0.00	1.25	0.20	0.24	0.00	1.28	0.18	0.22
DLP_{inf}	0.00	1.58	0.21	0.29	0.00	1.43	0.19	0.23	0.00	1.67	0.17	0.24	0.00	1.68	0.16	0.22

The mean HD between two surfaces is defined as the surface integral of the distance divided by the area of the compared surface (FDM_{sup}, FDM_{inf}, DLP_{sup}, DLP_{inf}). **I_1**= firs investigator, **I_2**= second investigator, **T_1**= firs measurement, **T_2**=second measurement, HD= Hausdorff Distance, RMS= root mean square

The distribution of the HD values along the vertebral surface meshes provides evidence for high accuracy (**Figure 39, Figure 40**). However, 'critical points' with higher HD values are revealed (red in **Figure 39**): the vertebral endplate in case of the FDM technique (superior surface: I_1T_2, I_2T_2; inferior: I_1T_1); the spinous process and the inferior articular processes in case of the DLP technology. The fact that, these higher HD values are not present in all segmentation processes (investigators and time points), indicates that it is probably a registration error and not a flaw of the printing technologies. The distribution of the HD values were indeed dependent on the investigators and the measurement time point (I_1vsI_2: FDM_{sup}, FDM_{inf}, DLP_{sup}, DLP_{inf}, Two-sample Kolmogorov–Smirnov test, for the measurement time point T_1vsT_2: FDM_{sup}, FDM_{inf}, DLP_{sup}, DLP_{inf}, Two-sample Kolmogorov–Smirnov test, $p < 0.01$). Nevertheless, ~99% of HD values were <1mm and ~80% <0.4 mm for all measurements (**Figure 40**), which according to the literature [95],[96] is an admissible difference and indicates that the geometry of the FVM model was printed correctly with both techniques. To compare the quality of the surfaces that provide the tactile experience during surgical planning we measured the surface roughness (SR) of the FDM and DLP printed physical models' surfaces. We chose two ROIs from both, FDM_{sup} and DLP_{sup}, surface meshes: one plain like and one highly curved structure, the superior vertebral endplate and the superior part of the pedicle, respectively.

DOI:10.14753/SE.2020.2439

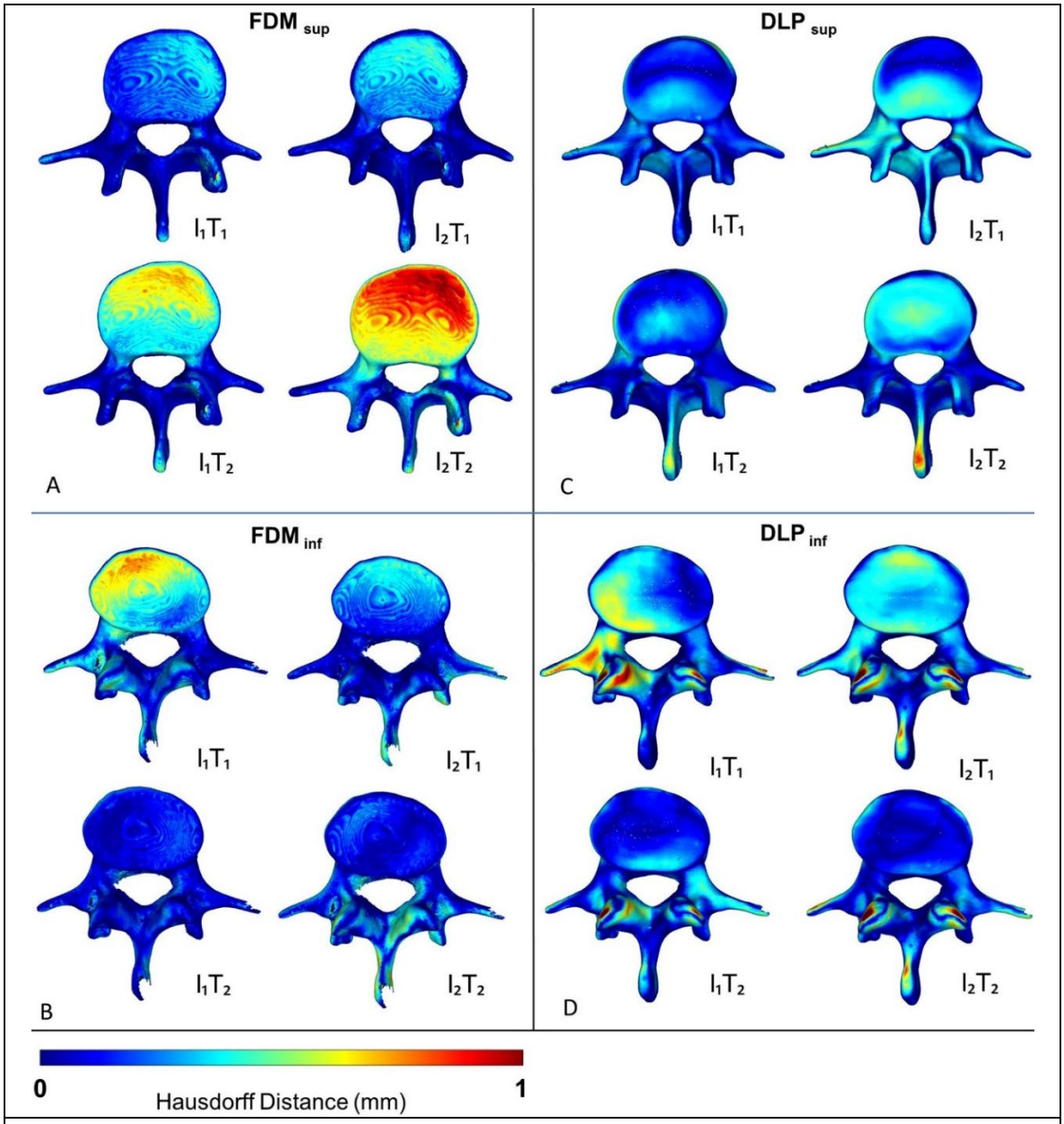

Figure 39. Comparison of the surface meshes of the 3D printed models to the input geometry. **A-D** distribution of Hausdorff Distance (HD) values between the aligned (I_1T_2, I_1T_2, I_2T_1, I_2T_2) surface meshes, derived from 3D scanning of the 3D printed models and the input geometry for the 3D printing process. (**A**, **C**) superior and (**B**, **D**) inferior surface mesh of the FDM and DLP printed models, respectively. The distribution of the measurements (I_1, I_2, T_1, T_2) across the FDM_{sup}, FDM_{inf}, DLP_{sup}, DLP_{inf} groups was significantly different (Independent Samples Kruskal-Wallis test, $p < 0.01$). I, number of the investigator; T, timepoint of the measurement.

DOI:10.14753/SE.2020.2439

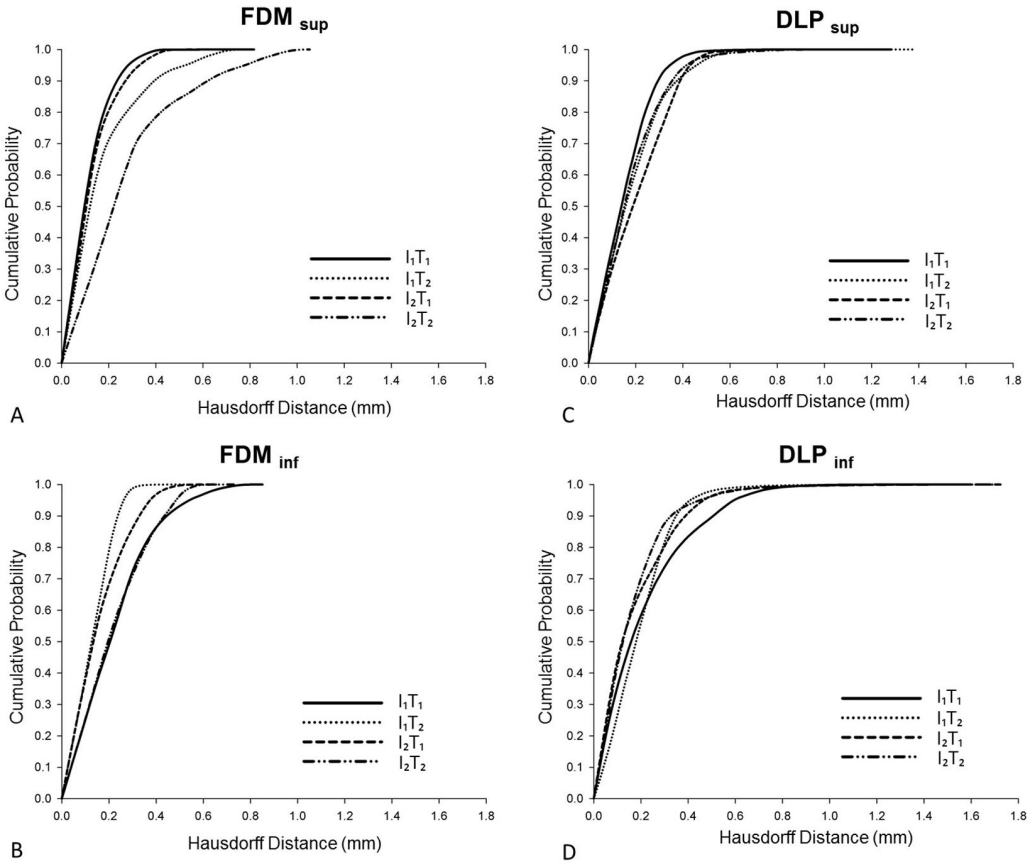

Figure 40. Distribution of HD values between the surface meshes of the 3D printed models and the input geometry. **A-D** cumulative probability plots of HD values for (**A**, **C**) superior and (**B**, **D**) inferior surface mesh of the FDM and DLP printed models, respectively. Approximately 99% percent of HD values are <1 mm and ~80% <0.4 mm for all comparisons. The distribution of the HD values are dependent from the investigator (I_1vs I_2: FDM_{sup}, FDM_{inf}, DLP_{sup}, DLP_{inf}, Two-sample Kolmogorov–Smirnov test, $p < 0.01$) and from the measurement time point (T_1vsT_2: FDM_{sup}, FDM_{inf}, DLP_{sup}, DLP_{inf}, Two-sample Kolmogorov–Smirnov test, $p < 0.01$). I, number of the investigator; T, time point of the measurement.

DOI:10.14753/SE.2020.2439

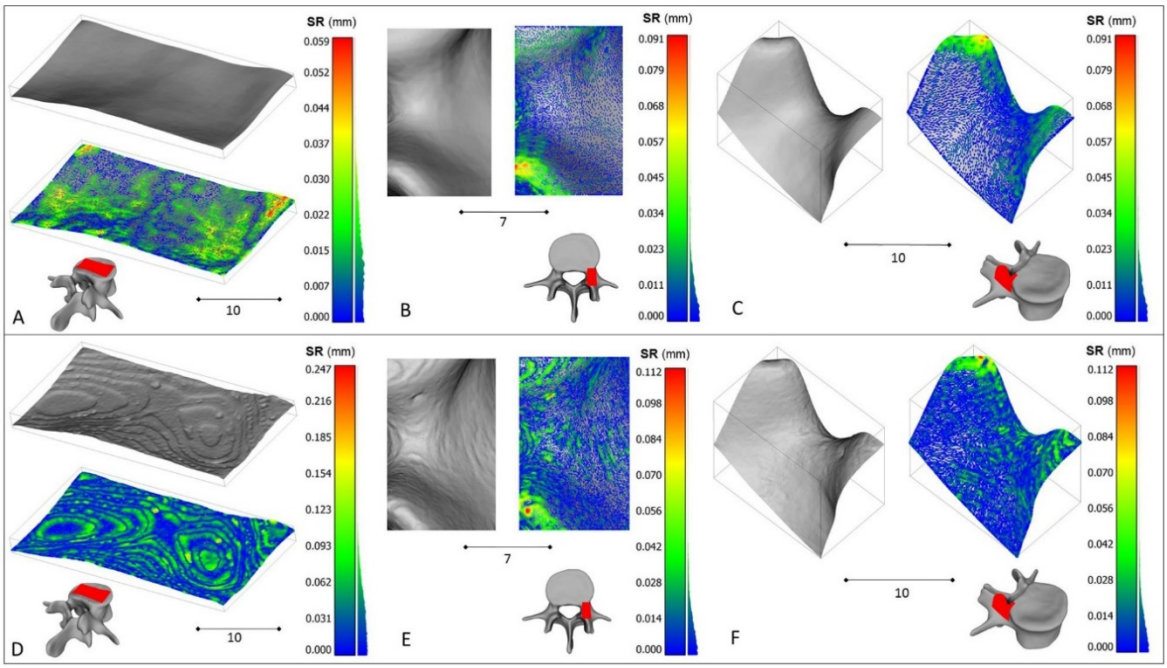

Figure 41. The surface roughness of the two 3D printed models is different. **A-F** roughness of FDM_{sup} (**D**, **E**, **F**) is greater compared to DLP_{sup} (**A**, **B**, **C** Two-sample Kolmogorov–Smirnov test, $p \leq 0.01$) for the endplate (**A**, **D** kernel set to 1.5 mm) and pedicle (**B**, **E**, **C**, **F** different views, respectively; kernel set to 0.6 mm) surface geometries (vertebra, view orientation; red, ROI). Scale bar **A**, **C**, **D**, **F** 10 mm; **B**, **E** 7 mm.

We found that the SR values of the surface meshes of the FDM printed model were significantly larger compared to the DLP printed model for the endplate ROI (Two-sample Kolmogorov–Smirnov test, $p \leq 0.01$), and in the case of the pedicle ROI (Two-sample Kolmogorov–Smirnov test, $p \leq 0.01$) (**Figure 41**).

However, the roughness values are relatively small on the entire ROI surfaces (**Figure 42**), with ~99% of the SR values being < 0.05 mm for the DLP printed model, and ~99% < 0.1 mm for FDM model in the case of the endplate. In the case of the pedicle ROI ~99% of SR values are < 0.09 mm for the DLP and for FDM model.

DOI:10.14753/SE.2020.2439

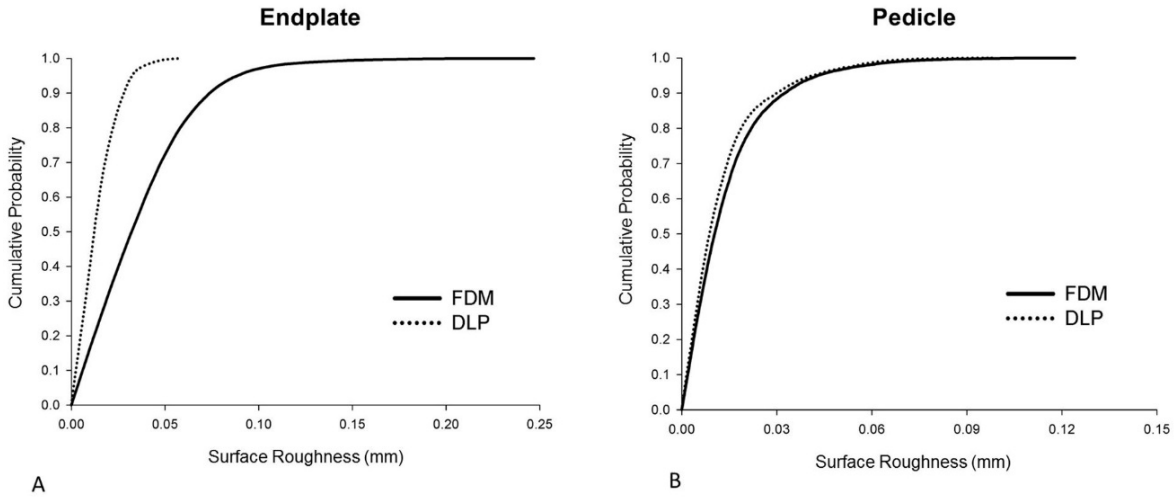

Figure 42. Distribution of Surface Roughness (SR) values for the FDM and DLP printing technology. **A-B** cumulative probability plots of SR values for the two region of interest ROI, **A** endplate and **B** right pedicle surface of the FDM and DLP printed models, respectively. In **A** ~99% percent of SR values are < 0,05 mm for the DLP printed model, and ~99% < 0.1 mm for FDM model. In **B** ~99% percent of SR values are < 0,09 mm for the DLP and for FDM model.

4.4.2. Clinical implementation of a physical model printed with FDM technology

We present a case of a 12-year-old patient suffering from congenital scoliosis due to an LI hemivertebra. During examination, the patient complained about back pain and fatigue; the physical examination did not reveal any sensorimotor deficits. In spite of conservative treatment (physical therapy, brace for two years), the clinical and radiological signs suggested progression **Figure 16** (COB angle 67° in coronal plane, and 90° kyphotic deformity in the sagittal plane); therefore, surgical treatment was indicated. A corpectomy and stabilization surgery from Th.IX to L.IV was planned.

DOI:10.14753/SE.2020.2439

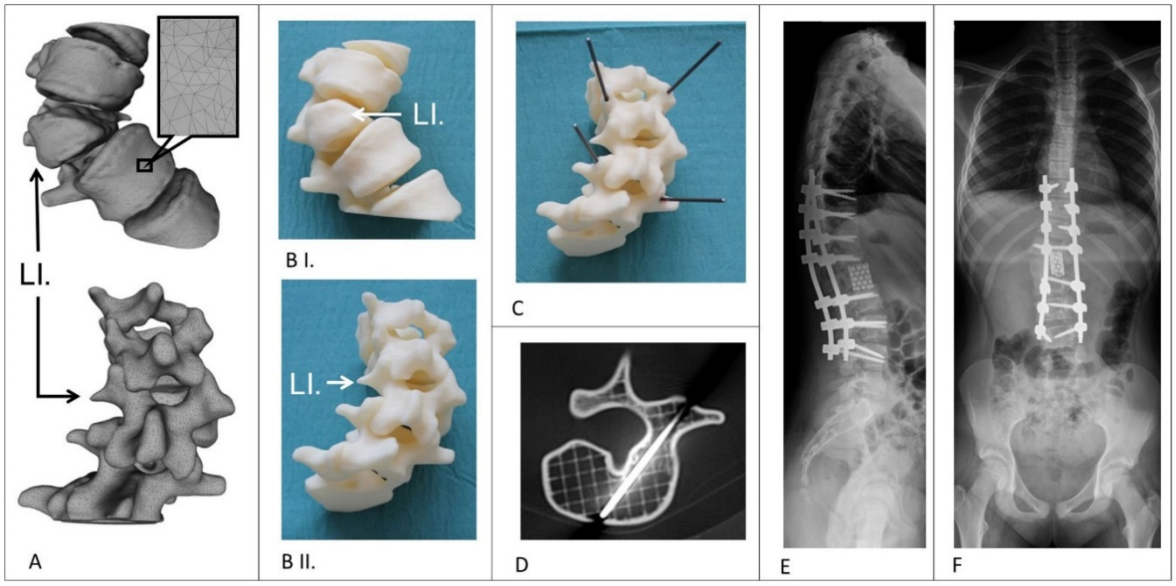

Figure 43. Application of the FDM 3D printed model in the surgical planning process in congenital scoliosis. **A** The segmented 3D geometry (triangulated surface mesh) of the thoraco-lumbar junction (L.I hemivertebra) in anterior and posterior view. **B** 3D printed physical model of the same thoraco-lumbar section as in **A**. **C** titanium rods were introduced in the pedicle, in the optimal axis of the screw insertion, as planned for the surgery. **D** internal grid structure of the FDM model with the inserted titanium rod (axial CT scan). **E-F** postoperative standing X-rays shows the screws (correction and stabilization from Th.IX to L.IV with Mesh cage) inserted in the correct position, helped by the visual guidance provided by the rods inserted in the physical model.

The virtual model of the Th.XI-L.III vertebrae (**Figure 43A**) was integrated in the clinical communication via a 3DPDF document (see Materials and methods), which provided access to its 3D content through the institutional database. Beingassisted by the patient specific 3D virtual model, the surgical team opted for a corpectomy and stabilization from Th.IX to L.IV. Our studies on FDM and DLP technologies revealed that the geometrical accuracy and surface qualities of the FDM printed models are adequate (HD, SR <1mm) and because its affordability, we chose to print our model with the FDM 3D printing technology. We used the physical model (1:1 scale) for surgical planning, namely to precisely define the trajectory and angle of the transpedicular screw insertion at the Th.XII and L.II levels (**Figure**

43B, C). During drilling, the internal grid structure of the FDM model supported the drill bit and allowed the precise insertion of guidance titanium rods **(Figure 43D**). The rods, due to their length, were protruding and indicating clearly the ideal axis of the screw insertion (**Figure 43C).** As a result of the visual guidance during the operation, we were able to find the optimal axis of the screw insertion and perform the planned surgery successfully (**Figure 43E)**.

4.5. PART V. Affordable surgical navigation using 3D printing and FEA

4.5.1 Navigation template geometrical accuracy and performance

In this part of my thesis a clinical case was used to present a technology development process in order to create a patient- specific drill template in a complex clinical case, in which a broken screw causes geometrical difficulty for new screw insertion. In order to safely insert the new screw, without compromising the local bone structure we developed a virtual surgical plan based on the QCT of the patient. This allowed us to test two different screw positions in the model and to design a drill template for safe screw insertion at the level of the first sacral vertebra with a geometrical difficulty caused by a broken screw from a previous surgery. The investment casted cobalt-chrome drill template retains the geometrical properties of the pattern (3D printed drill template model created with MSLA technology) based on the 3D scanning evaluation (**Figure 44**).

DOI:10.14753/SE.2020.2439

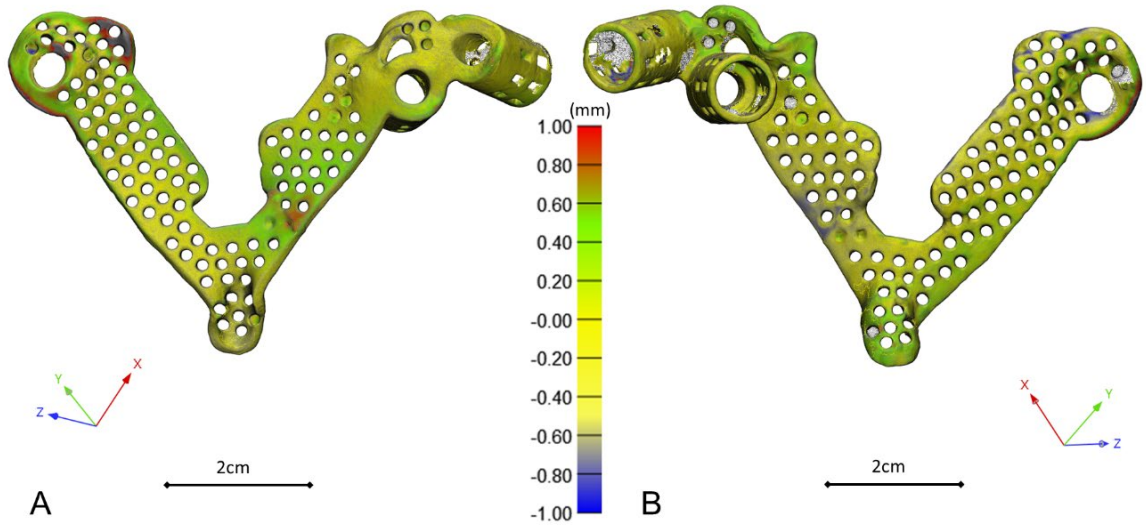

Figure 44. 3D scanning based geometrical accuracy measurement. Cobalt-chrome investment casted navigation template's geometrical accuracy compared to the 3D printed navigation template model created with MSLA technology. The colour map (Scale; min=-1 mm, max=1 mm) shows the geometrical difference, projected on the 3D printed navigation template triangle based mesh model vertices (**A** ventral view, **B** dorsal view).

DOI:10.14753/SE.2020.2439

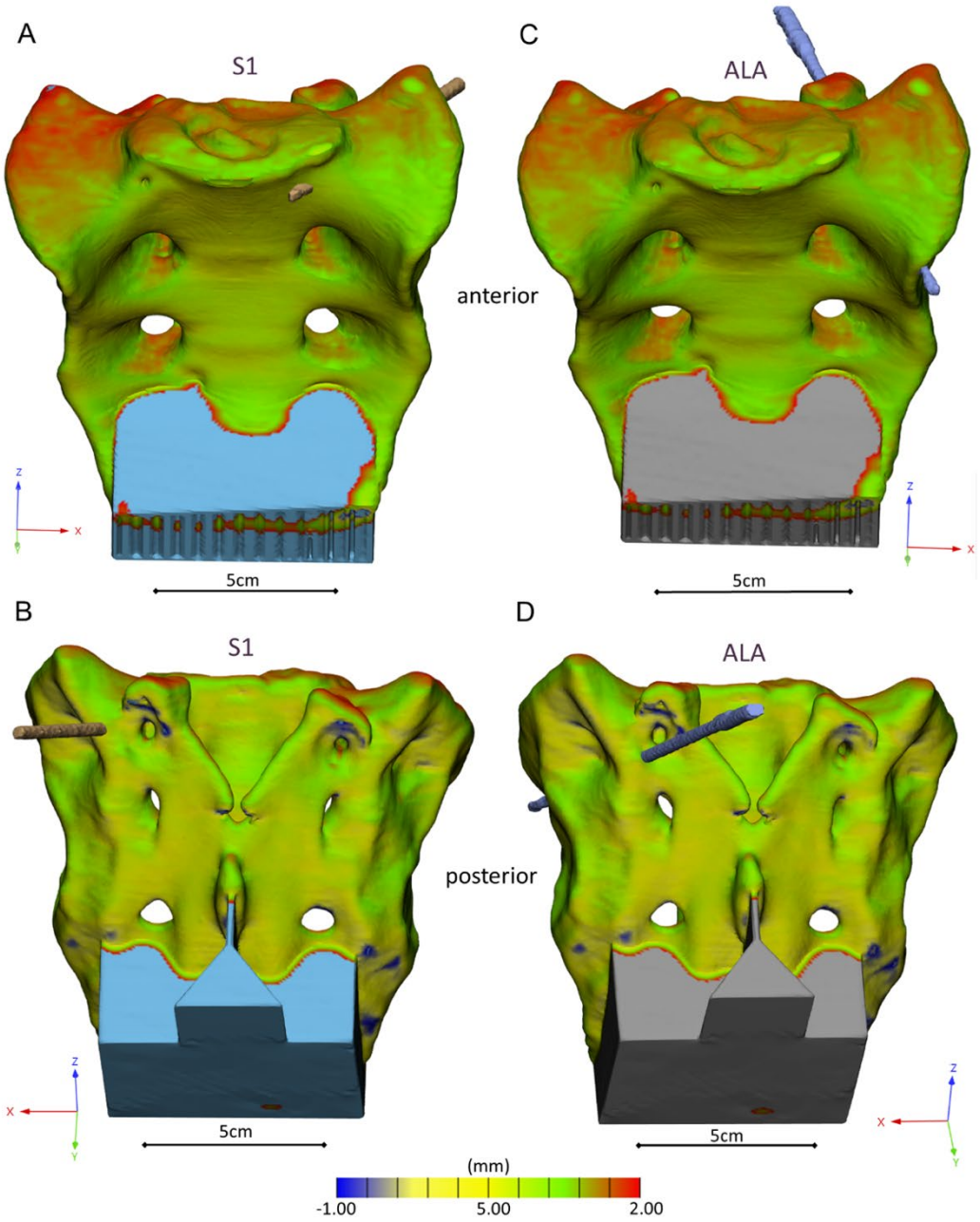

Figure 45. Alignment accuracy evaluation of the drilled patient specific physical and virtual sacrum model. (**A**, **B**, **C**, **D**) Surface mesh of the patient specific physical model and the drill bit (2.4 mm diameter) in S1 position (**A**, **B**) and ALA position (**C**, **D**) registered (rigid registration, point based + global registration) to the segmented patient sacrum derived from the QCT (**Figure 18**).

To evaluate the drill guide performance a 3D printed patient specific physical model was used. The physical model with the two drilling orientation was scanned with CT, then segmented and aligned to the virtual surgical plan (**Figure 22**, **Figure 45**). The drill guide provides a highly accurate screw insertion in both investigated positions (**Figure 46**). The cylinders representing the drilling axes were not perfectly colinear and coincident with the screws in the virtual surgical plan, but it can provide grade A (Gertzbein-Robbins scale) screw insertion.

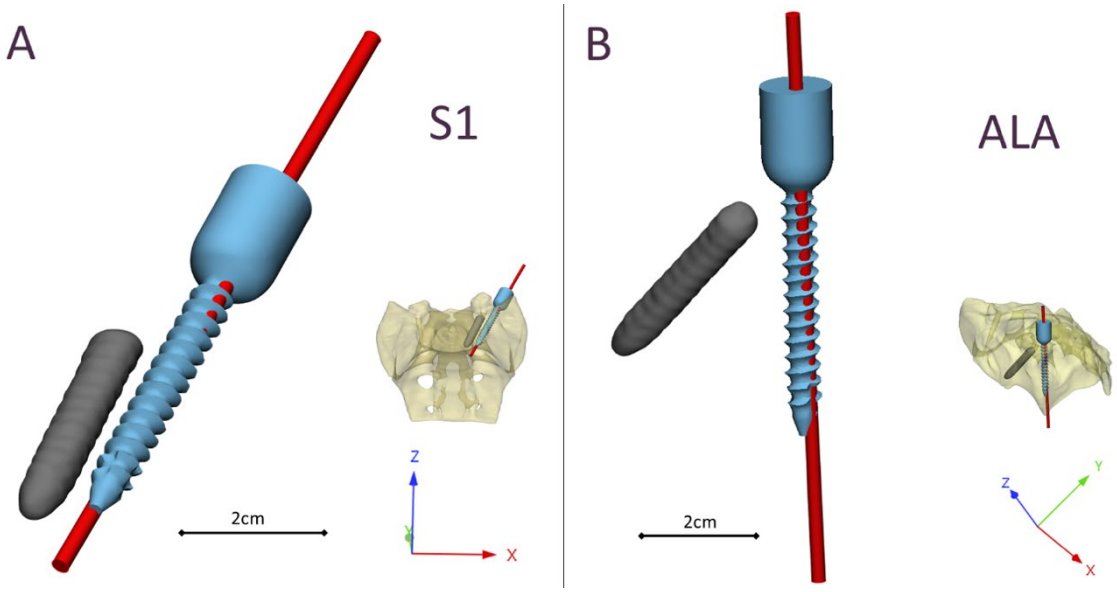

Figure 46. Visualization of the navigation template compared to the virtual plan. The red cylinders represent the drill bits' axes in the (**A**) convergent position (S1) and (**B**) divergent position (ALA), based on the evaluation performed on the patient-specific physical model. The broken and the implanted screw geometries are part of the virtual surgical plan based on the patient's QCT.

4.5.2. FEA results

In the presented workflow two possible screw insertion scenarios were investigated in a patient-specific FE model by integrating the individual geometry and bone material properties based on QCT. Nine models were created for each screw insertion scenario (N=9, S1 and N=9, ALA) with increasing element numbers based on the virtual surgical plan. The

FE simulation results converged above $2*10^5$ elements for both screw insertion scenarios at ~ 5 min solve times on 2 cores. The solve time at 2 cores for the S1 orientation was higher compared to the ALA (**Figure 47A**). The convergent bicortical screw insertion (S1) provided a stiffer position compared to the monocortical divergent screw position (**Figure 47B**).

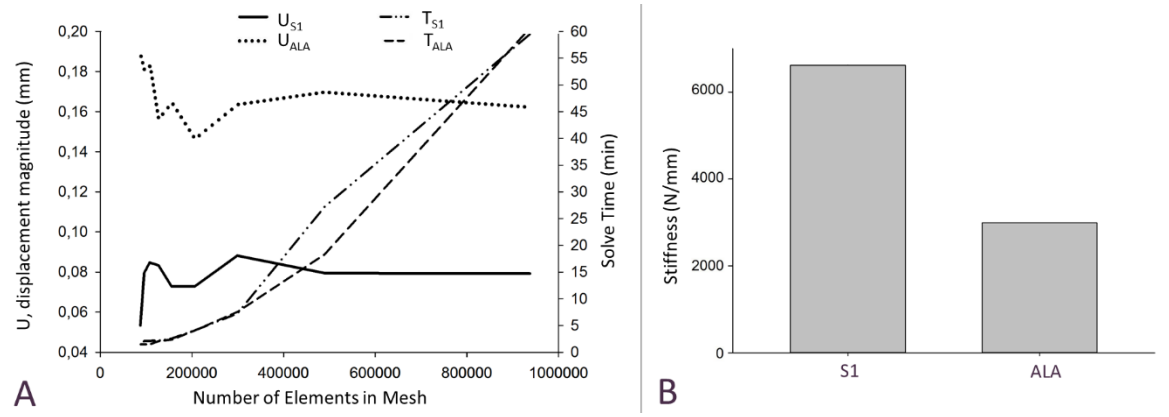

Figure 47. FE simulation results. (**A**) Convergence analysis for the average U, displacement magnitude (nodes of the middle 1/3 of the screw head) in convergent (U_{S1}) and divergent (U_{ALA}) screw positions at different mesh element numbers. Solve time distribution (right) at different mesh element numbers (convergent (T_{S1}) and divergent (T_{ALA}) screw positions). (**B**) The convergent screw insertion (S1) is stiffer (6617.23±1106.24 N/mm) compared to the divergent (ALA) insertion (2989.07±N/mm).

4.5.3. Proposed surgical technique

Based on our FEA results, the S1 screw insertion's surgical plan and drill template position is recommended for surgical implementation. We introduced a surgical technique for the screw insertion with the developed drill template (**Figure 48**). The technique uses a cannulated screw and tap, where the developed drill template supports a stainless-steel cylinder inlet to guide the drill bit and the Kirschner-wire.

DOI:10.14753/SE.2020.2439

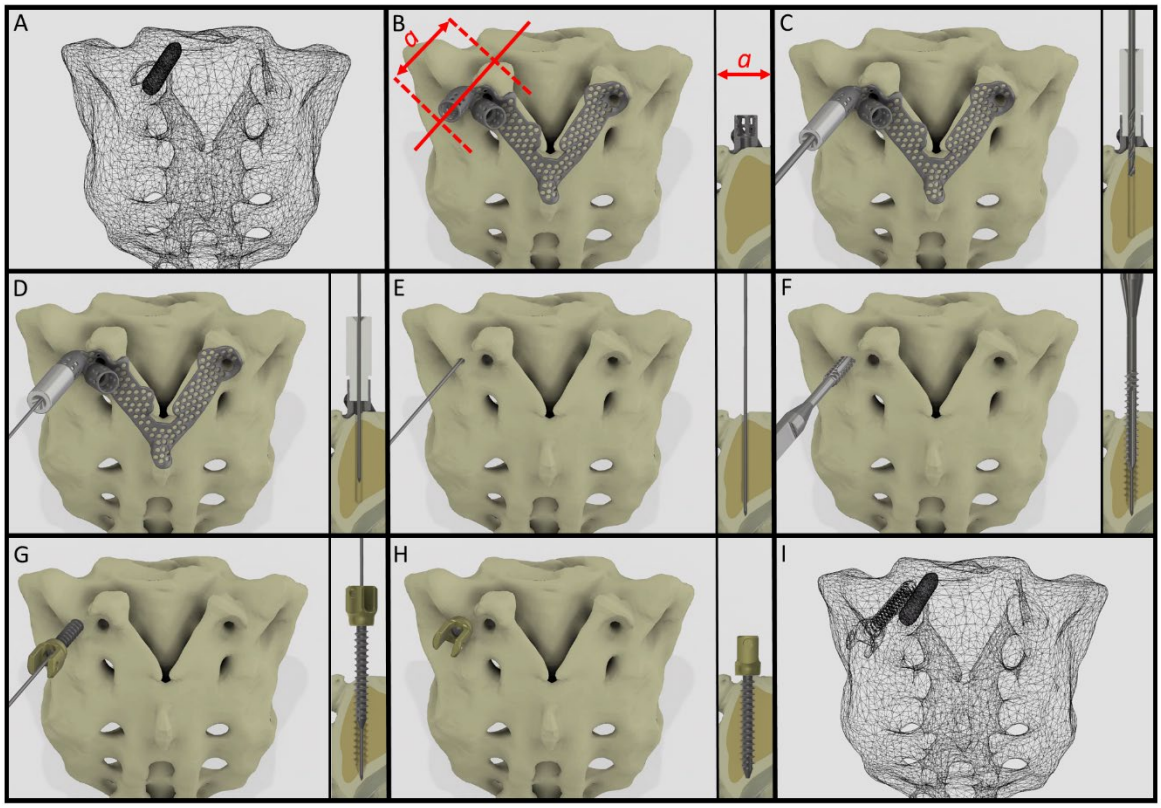

Figure 48. Proposed surgical technique for the safe and accurate screw insertion in convergent position. (**A**) transparent surface mesh of the patient sacrum with the broken screw. (**B**) section plane dimension and orientation, and drill guide position on the sacrum. (**C**) stainless steel cylinder inlet connected to the guide for the drill bit. (**D***)* stainless steel cylinder inlet connected to the guide for the Kirschner wire. (**E**) the inlet cylinder and the guide are removed, the Kirschner wire position is unchanged. (**F**) a cannulated tap is introduced along the Kirschner wire. (**G**) a cannulated pedicle screw is introduced in the sacrum along the Kirschner wire. (**H**) final position of the screw. (**I**) transparent surface mesh of the sacrum with the broken and convergently inserted pedicle screw geometry.

DOI:10.14753/SE.2020.2439

5. DISCUSSION

5.1. PART I. Need for 3D technologies among spine surgeons

Our survey research reveals a genuine interest in 3D technologies among spine surgeons on a global scale, which is emphasized by answers to questions related to the role of these technologies. Only 2.1% of the responders chose the answer: „no real future – too complicated and expensive"; and related to limitations to frequent use only a small minority of 1.4% chose the option „I am not interested in these technologies". Although the high financial demand topped among the barriers in front of frequent use of 3D modeling/printing, navigation, and advanced manufactured implants, it is important to note that these services and the technology itself has recently become less and less expensive. The decline in costs is expected to continue due to the continuous and fast development [67], [68], [69]. The appearance of several open-source software also reduces the required investments. Therefore, it is important to draw attention of the global spine surgeon community to the application of 3D technologies in everyday clinical practice and education, which does not necessary require significant financial investment. In case of the intraoperative navigation, the 3D printed patient-specific surgical guides are accurate [62], [63], and can be more accessible as traditional CT or fluoro-based systems [65], [66]. The lack of knowledge is an indisputable problem with several sources; little use of these technologies in education, incomplete information from media reports, growing but "hidden" body of scientific evidence. In addition, selection of the option „no or limited access to 3D modeling software" in high ratio demonstrates the disinformation of the paricipants since there are several user-friendly open-source or commercially available softwares. The use of these softwares requires some training, therefore establishing educational forums for surgeons is a necessity. These, educational events can also serve as an access platform to knowledge related to 3D technology and as an interaction platform with engineers for sharing the experience and starting collaborations.

The positive correlation between the attitude towards these technologies and the HDI of the country of origin highlights the role of education, economic environment and the developmental state of the healthcare system. The fact that the years of experience and

specialty of spine surgeons does not influence the level of acceptance raises the possibility of applying the technology within the whole professional community.

5.2. The importance of the 3D technologies in the investigation of surgical techniques

5.2.1. PART II. 3D geometrical change of the spinal canal after PCD

PCD is an MIS option to reduce low back pain caused by severe disc degeneration especially in elderly. The actual volumetric change and decompressive effect of the procedure was not quantified previously because of the lack of an appropriate 3D method. PCD is not the only a surgical procedure where the clinical effect is – at least partly – related to the indirect decompression of the spinal canal. A recent study by Navarro-Ramirez et al 2018 [97] reveals the usefulness of advanced computational methods by demonstrating that volumetric analysis of the anatomical change can predict better the clinical outcome of Extreme Lateral Interbody Fusion (XLIF) compared to conventional 2D methods [98] [99]. The highly accurate method described in the present study provides an exact and feasible option for the quantitative analysis of the 3D changes of the spinal canal after the different fusion techniques. The new approach for the assessment of the effect of the different techniques can provide the possibility for the evidence-based comparison method/methodology.

We found that PCD resulted in a significant increase of the spinal canal 3D dimensions and as such provided a clinically important indirect decompression effect. The injected PMMA distribution in the intervertebral space influences the decompression volume, with higher volume, larger surface and lower surface-volume ratio a greater decompression can be achieved. PCD procedure improves the disability and pain intensity of the patients. At 6-month follow-up we measured a 24 points improvement in ODI, 16 points in LBP, and 14 points in LP respectively which is a more than the minimal clinically important changes in ODI and VAS [100]. The pain relieving effect of the procedure significantly correlated with the measured volumetric change of the spinal canal (ie. the indirect decompression). This also indicates a volume dependent improvement of patient symptoms, with a higher injected PMMA volume resulting in better patient outcome. Disability was not associated with this parameter, indicating that the functional capacity of

the patient is a multidimensional feature also influenced by patient's lifestyle, general health status, other comorbidities, etc.

The present study provided scientific evidence on the indirect decompression effect of the PCD procedure due to the application of a novel computational method, however, there are some possible limitations of the study and the explanation of our results. Despite the fact, that the measurement and simulation method showed high accuracy and repeatability, we cannot exclude that more complex local anatomical variations can influence the application of the method. The external validation of the published measurement method even in another patient group would be also desirable. The change of clinical symptoms (ie. pain) and especially the disability are multifactorial features, so we could not precisely determine the direct effect of the indirect decompression. PCD is expected to also increase the biomechanical stability of the motion segment, which in itself can also provide pain relief and improved function. Further biomechanical, computational researches as well as large, multicenter cohort studies are required to clarify these open issues.

5.2.2. PART III. Nonrigid reconstruction of the lumbo-sacral junction using the "Closed Loop" technique

The Closed Loop reconstruction technique can provide excellent locomotor outcomes after total sacrectomy, similar result was demonstrated by Smith et al. [101], however, gait evaluation of this patient group is under published in the literature. The fact that the patient was able to walk resulted a periodic cyclical loading of the construct. Clark and his colleagues [102] compared 3 spinopelvic reconstruction techniques under gait-simulating fatigue loading and sagittal alignment failure on cadaveric specimens. Despite the complex gait like loading, the experiment's limitation (cadaveric specimen) does not take in consideration the bony fusion process only focus on the primer stability of the construct. In the scientific literature the cadaveric experiments or the FEA investigations proceed in the same way by investigating the primer stability of the constructs

In the present study, we developed a method for implant deformation investigation using postop CT scans collected over 6 years follow-up period of a patient who underwent sacrectomy and Closed Loop reconstruction. We were able, not only to demonstrate the non-

rigidity of the construct by measuring the geometry deformation over the FU, but we mapped bone remodeling at the fusion site (lumbar spine - two iliac bone) as well. Significant associations were found between the sagittal plane deformation and the postop days, resulting in a forward bending tendency of the construct.

According to Frost's *mechanostat* theory [103],[104] bone growth and bone loss is stimulated by the local mechanical elastic deformation of bone. Effects of implant construct stiffness on healing of fractures in case of long bones stabilized with internal fixation has been widely investigated [105],[106] , and it is known that too stiff constructs leads to non-union [107],[108],[109],[110]. In case of a posterior spinal fixation the stiffness of the implant rods (titanium alloys, stainless steel, cobalt-chromium–based alloys) can differ [111]. Load sharing that occurs with spinal implants results in decreased load through the stabilized vertebral body, thus strain is reduced in the bone of the vertebral body, which leads to bone mineral loss [111],[112]. The advantage of dynamic or non-rigid rods (exp. PEEK roods) is that it is able to reduce stress at the *implant*-bone interface and therefore does not produce stress shielding of the *bone graft* [113].

Our results demonstrated the non-rigid character (lower stiffness of the construct by using less implant) of the construct by quantifying the deformation over the follow-up period. The rod deformations are described in long constructs in the case of idiopathic scoliosis ([114],[115]) however it has not been investigated in lumbopelvic reconstructions. The developed method showed a high accuracy and repeatability, the provided information can play an important role in computational investigation of the lumbopelvic reconstructions techniques such as Finite Element models by enbending the simulation result in clinical context (demonstrating the deformation site of the contsruct to the FEA model).

The quantification of the bone formation uses the voxel dimensions and the Humsfield values of the voxel FE element mesh in the region of interests. The application of the mapping method on a large patient group would be desirable, for other reconstruction techniques as well. The optimal, expert opinion based, consensual reconstruction technique is not currently defined. The retrospective investigation of different methods based on CT scans over long FU (≥2 years) would be important for the better understanding of these complex surgical problems and to develop new solutions. The data obtained via this method

could be used for FEA models' validation and implant development, especially for 3D printed patient specific solutions [116].

Patient specific computational methods can provide accurate information about the implant construct deformation after sacrectomy, reconstructed with the „Closed Loop" technique. Due to its relative simplicity we suggest the application of our measurement method for the scientific and clinical analysis of other surgical procedures for the reconstruction of the lumbopelvic junction after sacrectomy, and for other clinical scenarios where large construct is needed such as idiopathic or degenerative deformity corrections, grooving rods systems, etc.

In the future the digitalisation of the medical field will provide large databases with imaging data , this will lead not only to In Silico Clinical Trails [117] but In Silico methods for follow up or retrospective analyses would be desirable.

Hopefully, the surgical treatment for chordomas in the future will be less aggressive and will have a tertiary role in the treatment, giving more space for molecular target-based drugs, combined with radiotherapy [118],[119]. The natural evolution of the chordoma treatment may result to the disappearance of the complex en-bloc resection by performing sacrectomy. The data collected about this rare patient population who underwent sacrectomy are highly valuable in the understanding of the pathology and physiology of the musculoskeletal system.

5.3. Application of 3D printing in spine care

5.3.1. PART IV. 3D printed physical models

Patient specific tangible, 3D printed physical models can improve surgical performance and outcome, compared to the sole on-screen inspection of the virtual models [120]. The first step in the medical image processing for the 3D printing is the segmentation method. The accuracy of this procedure is influenced by the resolution and the slice thickness of the 2D CT image series used for the segmentation [95]. In our institution the minimum criteria for the printing process is 512x512 pixel matrix resolution, and a maximum slice thickness of 1.3 mm. Manual editing is another potential source of error in the segmentation processes. For complex cases with severe deformations resulting in unique geometries, the

automatic or semi-automatic processes are not always adequate and therefore manual editing is inevitable. A solution to this issue is offered by the possibility of quantifying the segmentation accuracy using the inter-investigator DSI. According to the literature a DSI value of >0.85 is preferable [121],[91]. In this study the DSI value was 0.96, indicating that the segmented geometry of the LIV geometry represents accurately the anatomy of the vertebrae. Before printing, additional steps of the image processing are necessary to obtain high quality models. The surface mesh quality of the segmented geometry must be inspected for e.g. irregularities, holes, overlapping edges. In order to minimize the geometrical distortions, the following remeshing and optimization must take the preservation of the contour into consideration .

Once an accurate model of the vertebral geometry is achieved in STL format we propose a strategy of choosing any of the available 3D printing services, that the resources of a hospital permit. Our reasoning is that without an optimal, continuous utilization (not feasible in a hospital) of an in-house printing facility, its maintenance cost is a financial burden for the healthcare providers. Moreover, the technical parameters of a chosen in-house machine might not be adequate for all purposes, and therefore could potentially limit or define the projects or patients who can benefit from these technologies. In contrast, our strategy of choosing an available service, based on the predefined expectation on the geometrical accuracy, permits the most cost-effective choice for each case individually. Our comparison of an entry level, low cost (FDM) and a high category, expensive and highly precise (DLP) technologies provides evidence that a cost-effective technology can be more than suitable for patient specific 3D printed spine physical models. Final vertebral model (FVM) printing parameters with FDM technology: printing time: 343 min, total cost 198 € (euro), printing material cost 1 €/cm^3. Spine TXI-LIII model printing parameters with FDM technology: printing time: 660 min, total cost 336 €, printing material cost 1 €/cm^3. FVM printing parameters with DLP technology: printing time: 294 min, total cost 355 € (euro), printing material cost 3.2 €/cm^3. Spine TXI-LIII model printing parameters with DLP technology: printing time: 353 min, total cost 605 €, printing material cost 3.2 €/cm^3. 3D printing machines. The size of surface irregularities, even though somewhat larger for the FDM model, are tactually adequate for providing the surgeon with a tangible physical model

during surgical planning, therefore the advantage of superior printing precision of the more expensive DLP models is lost.

5.3.2. PART V. Affordable 3D printed patient-specific surgical navigation template

The concept of a patient-specific navigation template was first introduced by Radermacher et al. [122], who proposed a new navigation solution for the lumbar spine, hip and knee joint surgical procedures [122],[123]. The method used milling machine to manufacture the templates from polycarbonate. Due to the advances in 3D printing and 3D modelling technologies, the use of the individualised templates became more widespread [64], [124],[125], and it made an accurate and precise choice for navigational challenges [126].

The present study demonstrates the accuracy and applicability of the developed workflow which allows the creation of an affordable, metal individualized navigational template by integration FEA in the design and surgical planning process. The integration of FEA in the pedicle screw intraoperative navigation was investigated by Abbeele M. et al. [127], however the application of FEA in the design process of a navigational template in spine surgery by integrating the patient bone mineral density related material properties is new. The results of the simulations showed that the convergent S1 insertion is significantly stiffer than the divergent ALA insertion. This finding is supported by cadaveric experimental studies [128], [129] and clinical experience as well [130]. The biomechanical difference of the convergent and divergent insertions relies on the differences in the local bone mineral densities [131].

The combination of the 3D printing technology and cobalt-chrome casting makes the manufacturing process more affordable. Investment casting of cobalt-chrome is a widely used technology in dental laboratories [132]. 3D printed patterns for casting is an accepted method in dentistry [132], [133]; however, its application in spine surgery navigational templates is novel. The production of individualized metal navigational templates for screw insertion can be achieved via selective laser sintering 3D printing technology of titanium-

based alloys [134] , but at a higher cost and lower accessibility compared to dental casting. Metal templates are robust, resistant to damage and can also be easily autoclaved [134].

It is widely accepted in the literature to use cadavers for testing, evaluating the fitting accuracy of a navigational template [135]. FDM technology can produce geometrically accurate spine physical models [136] and the different designs can be tested as well as the drilling accuracy can be evaluated. The use of FDM models for design process evaluation and development is advantageous due to the possibility to include retrospective patient imaging data with complex anatomical/geometrical variation (deformities, tumours, etc.) which is extremely difficult to control and integrate in the case of cadaveric specimen studies. According to the Gertzbein-Robbins scale [137] the template theoretically allows an accurate (grade A) screw insertion (**Figure 46**). The suggested screw insertion surgical technique uses the philosophy of the minimally invasive pedicle screw insertion techniques (MIS) by using a Kirschner wire, cannulated tap and a pedicle screw. This technique can easily be performed by any spine surgeon familiar with MIS pedicle screw insertion.

Limitations of this study include the fact that the developed template is presented using a single case, however the workflow can be applied for different parts of the spine with different geometrical difficulties/pathologies. The presented FEA models' loading conditions are simplified as well as the material property assignments; more complex FEA investigations would be desirable. In the future, a randomized study of specific subtypes of spinal pathologies (tumours, deformities, etc.) with a larger sample size would be preferred to demonstrate the clinical efficacy and cost-effectiveness of the developed methodology.

5.4. Future plans for the application of the In Silico Biomechanical methods

The presented parts (I, II, III, IV, V) in my thesis demonstrate our institutional effort to integrate novel tools, techniques, and methods from the field of In Silico Medicine in the process of spine surgery related innovations. During my PhD years I had the opportunity to participate in a scientific collaboration between National Center for Spinal Disorders and the INSIGNEO Institute for in Silico Medicine, Department of Mechanical Engineering, The University of Sheffield, United Kingdom.

The need for this collaboration was based on the experience that the clinical assessment of risk of vertebral fracture in patients with lytic metastases is based on the Spinal Instability Neoplastic Score (SINS) [138],[139], which however in many cases does not provide clear guidelines. The joint effort made possible to perform a study [140], with the aim to develop a computational approach to provide a comparative biomechanical assessment of vertebrae with lytic lesions with respect to the adjacent controls and highlight the critical vertebrae.

The study used CT images of the thoracolumbar spine of eight patients suffering of vertebral lytic metastases with SINS between 7 and 12 (indeterminate unstable) were analysed. For each patient one or two vertebrae with lytic lesions were modelled and the closest vertebrae without lesions were considered as control. Metastatic and control vertebrae ($N = 12$, $N = 18$ respectively) were converted to subject-specific, isotropic, heterogeneous, nonlinear finite element models for simulating uniaxial compression. Densitometric and mechanical properties were computed for each vertebra. In average, similar mechanical properties were found for vertebrae with lytic lesions and controls (e.g. ultimate force equal to 6.2 ± 2.7 kN for vertebrae with lytic lesions and to 6.2 ± 3.0 kN for control vertebrae). Only in three patients the vertebrae with lytic lesions were found to be mechanically weaker (-19% to -75% difference for ultimate stress) than the controls [140]. Significant correlation between BMC (bone mineral content, g) and BMD (bone mineral density, g/cm^3) and the computed structural and normalised structural mechanical parameters were found, however, no significant correlation was found between SINS values and mechanical properties (**Figure 49**).

DOI:10.14753/SE.2020.2439

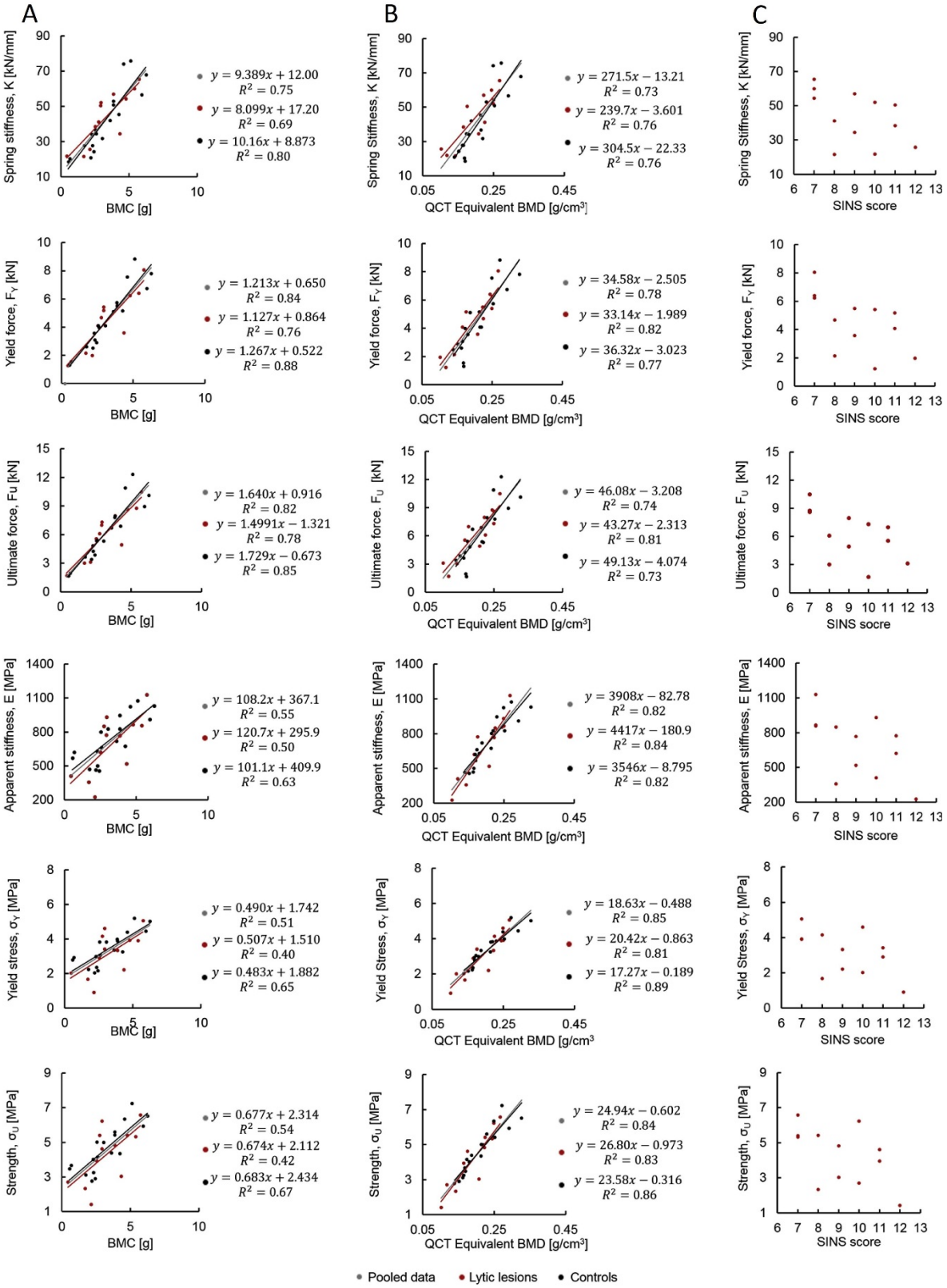

Figure 49. Results from the computational models (A, B) and the SINS (C). Linear regressions between BMC (A) and BMD (B) and structural and normalised structural mechanical parameters. Regression equations are reported for vertebrae with lesions (red), control vertebrae (black) or pooled data (grey). No significant correlation was found between SINS values and mechanical properties (C). Figure from Costa, M. C., **Eltes, P**., Lazary, A., Varga, P. P., Viceconti, M., & Dall'Ara, E. (2019). Biomechanical assessment of vertebrae with lytic metastases with subject-specific finite element models. *Journal of the mechanical behavior of biomedical materials*, *98*, 268-290.

The developed method underlines the need for tools that can be combined or integrated in the clinical scoring or classifications systems for a more accurate, patient-specific prediction of the current risk of fracture for vertebrae with lytic metastases. This study has the potential to offer for the clinicians a more accurate follow up data by capturing the mechanical properties of the lithic vertebra compared to normal or previous measurements. The future of in Silico Medicine not only offers In Silico clinical trials [117], but In Silico follow-up tools, methods as well, to evaluate the efficacy of treatments, or devices.

DOI:10.14753/SE.2020.2439

6. CONCLUSION

Based on the result of the survey research we can delineate tasks that are crucial for the further development and for the large-scale spinal application of 3D technologies. The clarification of the clinical cost-effectiveness of the technology is fundamentally requiring further clinical research projects with the active participation of spine surgeons. Spine surgeons should take part in the whole process not only as end-users but they have to be involved in the R&D steps as well. An optimal interdisciplinary work between researchers, engineers, and clinicians in order to develop and deliver new treatment possibilities through innovation can be supported by research funds but also facilitated by the active involvement of the med-tech industry. Another important task is the education and know-how delivery which has to be successfully implemented through educational events. Since the mission of the AOSpine is to advance science and spine care through research, education, and community development we invite members to initiate projects focusing on the sharing of the know-how of 3D technologies, taking into account the regional needs and differences.

Patient-specific computational methods provide accurate information about the unique and complex geometrical/anatomical relations due to intervertebral disc degeneration. In my thesis in Part II the 3D geometrical change of the spinal canal and the indirect decompression effect of a minimally invasive surgical procedure (PCD) was investigated with a new, computational 3D volumetric measurement method. Significant associations with the indirect decompression and the clinical improvement have been explored. Due to its relative simplicity we suggest the application of our measurement method for the scientific and clinical analysis of other surgical procedures based on indirect decompression effect such as anterior lumbar interbody fusion (ALIF), lateral lumbar interbody fusion (LLIF), oblique lumbar interbody fusion (OLIF), extreme lateral interbody fusion (XLIF).

Computational methods can provide accurate information about the implant construct deformation after sacrectomy, reconstructed with the „Closed Loop" technique. In Part III of my thesis, I developed a method for implant deformation investigation using the postop CT scans collected over 6 years' follow-up period of a patient who underwent sacrectomy and Closed Loop reconstruction. The method was able, not only to demonstrate the non-rigidity of the construct by measuring the geometry deformation over the FU, but mapped the bone

remodelling at the fusion site (lumbar spine-two iliac bones) as well. Significant associations with the sagittal plane deformation and the postop day were found, resulting in a forward bending tendency of the construct. Due to its relative simplicity, we suggest the application of the developed measurement method for the scientific and clinical analysis of other surgical procedures for the reconstruction of the lumbo-pelvic junction after sacrectomy, and for other clinical scenarios where large construct is needed such as idiopathic or degenerative deformity corrections, grooving roods systems, etc. Data obtained via this method could be used for FEA models' validation and implant development.

In Part IV and V of my thesis, I was investigating the clinical application of 3D printing technology with the use of image processing, 3D scanning, computer aided design finite element method.

Testing the accuracy of entry level (lower cost) 3D printing technologies, that are locally available on the healthcare market, is important for every clinician using such methods in surgical planning or education using 3D printed physical models. In Part IV of my thesis, it has been proven that a more cost-effective technology is sufficiently precise in the case of 3D printed physical models of the spine. If other less expensive technologies can similarly be proven to be adequate for several purposes, than the cost of 3D printing technologies can be reduced to a level that is not only acceptable for healthcare systems but will promote their widespread use.

The developed patient-specific template presented in Part V of my thesis for pedicle screw insertion allows surgeons to insert the screw into its optimal position. Its advantages compared to the conventional surgical navigation techniques are the relatively low cost, and the potential to reduce the intraoperative X-ray exposure and the possibility for the consideration of the patient-specific bone geometry and biomechanics. This new patient- and condition-specific approach can be widely used in revision spine surgeries or in challenging primary cases after its further clinical validations**.**

DOI:10.14753/SE.2020.2439

7. SUMMARY

The general aim of my Ph.D. work was to investigate the implementation of In Silico Biomechanical Methods in Spine Surgery Innovations.

The first part of my thesis in a survey based study (Eltes et al., 2019) in which I answered the question of what determines the acceptance rate and the factors which stand against the widespread usage of the 3D technologies in spine surgery. Investigation of these problems defined a global context regarding 3D technologies in spine surgery.

In the second and third parts of my Ph.D. work, I investigated two surgical methods the Percutaneous Cement Discoplasty (PCD) and the Closed Loop lumbopelvic reconstruction technique via the application of 3D technologies. In part two a generalizable procedure based on patient-specific 3D computational, volumetric measurements to evaluate the geometrical change of the spinal canal after PCD treatment was successfully developed. In part three a generalizable method based on patient-specific 3D geometries derived from CT scans was developed to investigate the implant construct deformation over a 6-year follow-up period for a patient who underwent sacrectomy and the Closed Loop technique for lumbopelvic reconstruction. The two methods not only provide unique information about the surgical methods which currently are not available via conventional 2D radiological methods, but it can be applied to investigate other surgical techniques as well.

The global perspective on the attitude of the spine surgeons towards the application of 3D technologies given by the survey study raises the need for strategies to implement 3D printing and finite-element analysis in the clinical environment in an affordable way. Part four of my thesis addresses the need for the application of affordable 3D printed physical models by developing a method for geometrical accuracy evaluation for different types of 3D printing technologies (Eltes et al., 2020). Part five of my thesis addresses the clinical need for the development of computer aided design and finite-element analysis combined method for affordable spine surgical navigation with a 3D printed customized drill guide to allow safe pedicle screw insertion in challenging situations.

In my thesis, I deliver in five thematic parts a detailed, comprehensive way for the aimed implementation of the In Silico Biomechanical Methods in Spine Surgery Innovations in the spirit of the Stanford Biodesign Process.

DOI:10.14753/SE.2020.2439

8. ÖSSZEFOLGALÓ

Ph.D. munkám általános célja az In Silico Biomechanikai módszerek integrálása a gerincsebészettel kapcsolatos innovációk folyamatába.

Dolgozatom első részét egy kérdőív alapú felmérésre épülő tanulmány képezi (Eltes et al., 2019) melyben egy globális kontextusban értelmezhető és azonosítható a 3D technológiák gerincsebészetben történő alkalmazásának igénye, illetve limitációja.

A dolgozat második és harmadik részében két műtéti technikát, a Perkután Cement Diszkoplasztikát (PCD) és a Closed Loop lumbopelvicus rekonstrukciós technikát vizsgáltam a 3D technológiák alkalmazásával. A második részben egy beteg-specifikus 3D-s számítógépes, volumetriai méréseken alapuló, eljárást dolgoztam ki a PCD kezelés hatására létrejövő, a gerinccsatorna geometriai változásának a meghatározására. A harmadik részben egy sacrectomián átesett beteg 6 éves után követése során készült CT-vizsgálatok felvételeit felhasználva, 3D geometriákon alapuló, módszert fejlesztettem ki a Closed Loop implantátum konstrukció deformációjának meghatározására. A két módszer nemcsak a vizsgált műtéti módszerekről ad egyedi információt, hanem alkalmazhatók más műtéti technikák vizsgálatára is.

A gerincsebészek 3D-technológiák alkalmazásával kapcsolatos hozzáállásának globális perspektívája, felhívja a figyelmet a 3D nyomtatás és a véges elem analízis klinikai környezetben történő megfizethető módon történő alkalmazásának szükségességére. Dolgozatom negyedik része a megfizethető 3D nyomtatott fizikai modellek alkalmazásának stratégiájával foglalkozik, egy geometriai pontosságot meghatározó módszer kidolgozásával, melynek segítségével különböző árkategóriajú nyomtatási technológiák hasonlíthatok össze (Eltes et al., 2020). Dolgozatom ötödik részében a számítógépes tervezés és a véges elem analízis módszerének együttes alkalmazásával létrehozott fejlesztési folyamat eredményeként megvalósuló, megfizethető, egyénre szabott gerinc műtéti navigációs 3D-s nyomtatott eszköz kerül bemutatásra, amely lehetővé teszi a transpedikuláris csavar biztonságos behelyezését kihívásokkal teli helyzetekben.

Dolgozatomban részletes, átfogó módszereket mutatok be öt tematikus részben az In Silico Biomechanikai módszerek célzott, gerincsebészeti innovációk során történő alkalmazására, a Stanford Biodesign folyamat szellemében.

9. BIBLIOGRAPHY

1. Combley R (2011) Cambridge business English dictionary. Cambridge University Press
2. Maranville S (1992) Entrepreneurship in the Business Curriculum. J Educ Bus 68:27–31. https://doi.org/10.1080/08832323.1992.10117582
3. Jarvis W (1994) Handwashing—the Semmelweis lesson forgotten? Lancet 344:1311–1312
4. Hellinger J (1973) Die Behandlung von pseudarthrosen langer röhrenknochen mit simultaner beinverlängerung. Zbl Chir 98:1272–1276
5. Radiology ES of (2011) Medical imaging in personalised medicine: a white paper of the research committee of the European Society of Radiology (ESR). Insights Imaging 2:621–630. https://doi.org/10.1007/s13244-011-0125-0
6. Rosenberg N (1986) The impact of technological innovation: a historical view. Posit sum Strateg Harnessing Technol Econ growth 17
7. Wall J, Wynne E, Krummel T (2015) Biodesign process and culture to enable pediatric medical technology innovation. Semin Pediatr Surg 24:102–106. https://doi.org/10.1053/J.SEMPEDSURG.2015.02.005
8. Yock PG, Brinton TJ, Zenios SA (2011) Teaching biomedical technology innovation as a discipline. Sci Transl Med 3:92cm18-92cm18
9. Viceconti M (2015) Biomechanics-based in silico medicine: The manifesto of a new science. J Biomech 48:193–194. https://doi.org/10.1016/j.jbiomech.2014.11.022
10. Goel VK, Nyman E (2016) Computational Modeling and Finite Element Analysis. Spine (Phila Pa 1976) 41 Suppl 7:S6-7. https://doi.org/10.1097/BRS.0000000000001421
11. Tong Y, Kaplan DJ, Spivak JM, Bendo JA (2019) Three-Dimensional Printing in Spine Surgery: A Review of Current Applications. Spine J. https://doi.org/10.1016/j.spinee.2019.11.004
12. Fagan MJ, Julian S, Mohsen AM (2002) Finite element analysis in spine research. Proc Inst Mech Eng part h J Eng Med 216:281–298
13. Xu N, Wei F, Liu X, Jiang L, Cai H, Li Z, Yu M, Wu F, Liu Z (2016) Reconstruction of the Upper Cervical Spine Using a Personalized 3D-Printed Vertebral Body in an Adolescent With Ewing Sarcoma. Spine (Phila Pa 1976) 41:E50-4. https://doi.org/10.1097/BRS.0000000000001179
14. Galbusera F, Bassani T, La Barbera L, Ottardi C, Schlager B, Brayda-Bruno M, Villa T, Wilke H-J (2015) Planning the Surgical Correction of Spinal Deformities: Toward the Identification of the Biomechanical Principles by Means of Numerical Simulation. Front Bioeng Biotechnol 3:178. https://doi.org/10.3389/fbioe.2015.00178
15. Henao J, Aubin C-É, Labelle H, Arnoux P-J (2016) Patient-specific finite element model of the spine and spinal cord to assess the neurological impact of scoliosis correction: preliminary application on two cases with and without intraoperative neurological complications. Comput Methods Biomech Biomed Engin 19:901–10. https://doi.org/10.1080/10255842.2015.1075010
16. Klein GT, Lu Y, Wang MY (2013) 3D printing and neurosurgery--ready for prime

time? World Neurosurg 80:233–5. https://doi.org/10.1016/j.wneu.2013.07.009
17. Brekelmans WA, Poort HW, Slooff TJ (1972) A new method to analyse the mechanical behaviour of skeletal parts. Acta Orthop Scand 43:301–17. https://doi.org/10.3109/17453677208998949
18. Hirai T (2017) The Human Development Index and Its Evolution. In: The Creation of the Human Development Approach. Springer, pp 73–121
19. Vos T, Flaxman AD, Naghavi M, Lozano R, Michaud C, Ezzati M, Shibuya K, Salomon JA, Abdalla S, Aboyans V, Abraham J, Ackerman I, Aggarwal R, Ahn SY, Ali MK, Alvarado M, Anderson HR, Anderson LM, Andrews KG, et al (2012) Years lived with disability (YLDs) for 1160 sequelae of 289 diseases and injuries 1990-2010: a systematic analysis for the Global Burden of Disease Study 2010. Lancet (London, England) 380:2163–96. https://doi.org/10.1016/S0140-6736(12)61729-2
20. Raciborski F, Gasik R, Kłak A (2016) Disorders of the spine. A major health and social problem. Reumatologia 54:196–200. https://doi.org/10.5114/reum.2016.62474
21. Hoy D, March L, Brooks P, Blyth F, Woolf A, Bain C, Williams G, Smith E, Vos T, Barendregt J, Murray C, Burstein R, Buchbinder R (2014) The global burden of low back pain: estimates from the Global Burden of Disease 2010 study. Ann Rheum Dis 73:968–74. https://doi.org/10.1136/annrheumdis-2013-204428
22. Hurwitz EL, Randhawa K, Yu H, Côté P, Haldeman S (2018) The Global Spine Care Initiative: a summary of the global burden of low back and neck pain studies. Eur Spine J 27:796–801. https://doi.org/10.1007/s00586-017-5432-9
23. Shapiro IM, Risbud M V. (2014) Introduction. Springer-Verlag Wien
24. Pfirrmann CWA, Metzdorf A, Zanetti M, Hodler J, Boos N (2001) Magnetic resonance classification of lumbar intervertebral disc degeneration. Spine (Phila Pa 1976) 26:1873–1878
25. Knutsson F (1942) The Vacuum Phenomenon in the Intervertebral Discs. Acta radiol 173–179. https://doi.org/10.1177/028418514202300207
26. Samuel E (1948) Vacuum Intervertebral Discs. Br J Radiol 21:337–339. https://doi.org/10.1259/0007-1285-21-247-337
27. Morishita K, Kasai Y, Uchida A (2008) Clinical symptoms of patients with intervertebral vacuum phenomenon. Neurologist 14:37–9. https://doi.org/10.1097/NRL.0b013e3180dc9992
28. Humzah MD, Soames RW (1988) Human intervertebral disc: Structure and function. Anat Rec 220:337–356. https://doi.org/10.1002/ar.1092200402
29. Inoue N, Espinoza Orías AA (2011) Biomechanics of intervertebral disk degeneration. Orthop Clin North Am 42:487–99, vii. https://doi.org/10.1016/j.ocl.2011.07.001
30. Lee SY, Kim T-H, Oh JK, Lee SJ, Park MS (2015) Lumbar Stenosis: A Recent Update by Review of Literature. Asian Spine J 9:818–28. https://doi.org/10.4184/asj.2015.9.5.818
31. Varga PP, Jakab G, Bors IB, Lazary A, Szövérfi Z (2015) Experiences with PMMA cement as a stand-alone intervertebral spacer. Percutaneous cement discoplasty in the case of vacuum phenomenon within lumbar intervertebral discs. Orthopade 44:124–131
32. Kiss L, Varga PP, Szoverfi Z, Jakab G, Eltes PE, Lazary A (2019) Indirect foraminal decompression and improvement in the lumbar alignment after percutaneous cement

discoplasty. Eur Spine J 1–7
33. Steurer J, Roner S, Gnannt R, Hodler J (2011) Quantitative radiologic criteria for the diagnosis of lumbar spinal stenosis: a systematic literature review. BMC Musculoskelet Disord 12:175. https://doi.org/10.1186/1471-2474-12-175
34. Andreisek G, Imhof M, Wertli M, Winklhofer S, Pfirrmann CWA, Hodler J, Steurer J, Zurich for the LSSOSWG (2013) A Systematic Review of Semiquantitative and Qualitative Radiologic Criteria for the Diagnosis of Lumbar Spinal Stenosis. Am J Roentgenol 201:W735–W746. https://doi.org/10.2214/AJR.12.10163
35. Yoshihara H (2017) Indirect decompression in spinal surgery. J Clin Neurosci 44:63–68. https://doi.org/10.1016/J.JOCN.2017.06.061
36. Varga PP, Bors I, Lazary A (2009) 1. Varga PP, Bors I, Lazary A. Sacral Tumors and Management. Orthop Clin North Am. 2009;40(1):105-123. doi:10.1016/J.OCL.2008.09.010Sacral Tumors and Management. Orthop Clin North Am 40:105–123. https://doi.org/10.1016/J.OCL.2008.09.010
37. Feldenzer JA, McGauley JL, McGillicuddy JE (1989) Sacral and presacral tumors: problems in diagnosis and management. Neurosurgery 25:884–91
38. Disler DG, Miklic D (1999) Imaging findings in tumors of the sacrum. AJR Am J Roentgenol 173:1699–706. https://doi.org/10.2214/ajr.173.6.10584822
39. Jo VY, Fletcher CDM (2014) WHO classification of soft tissue tumours: an update based on the 2013 (4th) edition. Pathology 46:95–104
40. Fourney DR, Rhines LD, Hentschel SJ, Skibber JM, Wolinsky J-P, Weber KL, Suki D, Gallia GL, Garonzik I, Gokaslan ZL (2005) En bloc resection of primary sacral tumors: classification of surgical approaches and outcome. J Neurosurg Spine 3:111–22. https://doi.org/10.3171/spi.2005.3.2.0111
41. Zoccali C, Skoch J, Patel AS, Walter CM, Maykowski P, Baaj AA (2016) Residual neurological function after sacral root resection during en-bloc sacrectomy: a systematic review. Eur Spine J 25:3925–3931. https://doi.org/10.1007/s00586-016-4450-3
42. Varga PP, Szövérfi Z, Fisher CG, Boriani S, Gokaslan ZL, Dekutoski MB, Chou D, Quraishi NA, Reynolds JJ, Luzzati A, Williams R, Fehlings MG, Germscheid NM, Lazary A, Rhines LD (2015) Surgical treatment of sacral chordoma: prognostic variables for local recurrence and overall survival. Eur Spine J 24:1092–1101. https://doi.org/10.1007/s00586-014-3728-6
43. Varga PP, Szoverfi Z, Lazary A (2014) Surgical resection and reconstruction after resection of tumors involving the sacropelvic region. Neurol Res 36:588–596. https://doi.org/10.1179/1743132814Y.0000000370
44. Zileli M, Hoscoskun C, Brastianos P, Sabah D (2003) Surgical treatment of primary sacral tumors: complications associated with sacrectomy. Neurosurg Focus 15:E9
45. Petrick IJ, Simpson TW (2013) 3D Printing Disrupts Manufacturing: How Economies of One Create New Rules of Competition. Res Manag 56:12–16. https://doi.org/10.5437/08956308X5606193
46. Berman B (2012) 3-D printing: The new industrial revolution. Bus Horiz 55:155–162. https://doi.org/10.1016/J.BUSHOR.2011.11.003
47. Rengier F, Mehndiratta A, von Tengg-Kobligk H, Zechmann CM, Unterhinninghofen R, Kauczor H-U, Giesel FL (2010) 3D printing based on imaging data: review of

medical applications. Int J Comput Assist Radiol Surg 5:335–341. https://doi.org/10.1007/s11548-010-0476-x
48. Wilcox B, Mobbs RJ, Wu A-M, Phan K (2017) Systematic review of 3D printing in spinal surgery: the current state of play. J Spine Surg 3:433–443. https://doi.org/10.21037/jss.2017.09.01
49. Li Z, Li Z, Xu R, Li M, Li J, Liu Y, Sui D, Zhang W, Chen Z (2015) Three-dimensional printing models improve understanding of spinal fracture—A randomized controlled study in China. Sci Rep 5:11570. https://doi.org/10.1038/srep11570
50. Bernhard J-C, Isotani S, Matsugasumi T, Duddalwar V, Hung AJ, Suer E, Baco E, Satkunasivam R, Djaladat H, Metcalfe C, Hu B, Wong K, Park D, Nguyen M, Hwang D, Bazargani ST, de Castro Abreu AL, Aron M, Ukimura O, et al (2016) Personalized 3D printed model of kidney and tumor anatomy: a useful tool for patient education. World J Urol 34:337–345. https://doi.org/10.1007/s00345-015-1632-2
51. Martelli N, Serrano C, van den Brink H, Pineau J, Prognon P, Borget I, El Batti S (2016) Advantages and disadvantages of 3-dimensional printing in surgery: A systematic review. Surgery 159:1485–1500. https://doi.org/10.1016/J.SURG.2015.12.017
52. Organization WH (2015) World report on ageing and health. World Health Organization
53. Beard JR, Officer A, de Carvalho IA, Sadana R, Pot AM, Michel J-P, Lloyd-Sherlock P, Epping-Jordan JE, Peeters GMEE (Geeske), Mahanani WR, Thiyagarajan JA, Chatterji S (2016) The World report on ageing and health: a policy framework for healthy ageing. Lancet 387:2145–2154. https://doi.org/10.1016/S0140-6736(15)00516-4
54. Ben-Ner A, Siemsen E (2017) Decentralization and Localization of Production:The Organizational and Economic Consequences of Additive Manufacturing (3D Printing). Calif Manage Rev 59:5–23. https://doi.org/10.1177/0008125617695284
55. Gaines Jr RW (2000) The use of pedicle-screw internal fixation for the operative treatment of spinal disorders. JBJS 82:1458
56. Kast E, Mohr K, Richter H-P, Börm W (2006) Complications of transpedicular screw fixation in the cervical spine. Eur spine J 15:327–334
57. Faraj AA, Webb JK (1997) Early complications of spinal pedicle screw. Eur spine J 6:324–326
58. Merloz P, Tonetti J, Pittet L, Coulomb M, Lavallee S, Troccaz J, Cinquin P, Sautot P (1998) Computer-assisted spine surgery. Comput Aided Surg Off J Int Soc Comput Aided Surg 3:297–305
59. Foley KT, Simon DA, Rampersaud YR (2001) Virtual fluoroscopy: computer-assisted fluoroscopic navigation. Spine (Phila Pa 1976) 26:347–351
60. Nolte L-P, Slomczykowski MA, Berlemann U, Strauss MJ, Hofstetter R, Schlenzka D, Laine T, Lund T (2000) A new approach to computer-aided spine surgery: fluoroscopy-based surgical navigation. Eur Spine J 9:S078–S088. https://doi.org/10.1007/PL00010026
61. Ishikawa Y, Kanemura T, Yoshida G, Matsumoto A, Ito Z, Tauchi R, Muramoto A, Ohno S, Nishimura Y (2011) Intraoperative, full-rotation, three-dimensional image (O-arm)–based navigation system for cervical pedicle screw insertion. J Neurosurg

Spine 15:472–478. https://doi.org/10.3171/2011.6.SPINE10809
62. Putzier M, Strube P, Cecchinato R, Lamartina C, Hoff EK (2017) A New Navigational Tool for Pedicle Screw Placement in Patients With Severe Scoliosis: A Pilot Study to Prove Feasibility, Accuracy, and Identify Operative Challenges. Clin spine Surg 30:E430–E439. https://doi.org/10.1097/BSD.0000000000000220
63. Jiang L, Dong L, Tan M, Qi Y, Yang F, Yi P, Tang X (2017) A Modified Personalized Image-Based Drill Guide Template for Atlantoaxial Pedicle Screw Placement: A Clinical Study. Med Sci Monit 23:1325–1333. https://doi.org/10.12659/msm.900066
64. Garg B, Gupta M, Singh M, Kalyanasundaram D (2019) Outcome and safety analysis of 3D-printed patient-specific pedicle screw jigs for complex spinal deformities: a comparative study. Spine J 19:56–64. https://doi.org/10.1016/J.SPINEE.2018.05.001
65. Cristina Mancarella AL, Roberto Delfini FG, i, Mancarella C, Gregori F, Delfini R (2015) Spinal Neuronavigation and 3D-Printed Tubular Guide for Pedicle Screw Placement: A Really New Tool to Improve Safety and Accuracy of the Surgical Technique? J Spine 04:1–3. https://doi.org/10.4172/2165-7939.1000e118
66. Guo F, Dai J, Zhang J, Ma Y, Zhu G, Shen J, Niu G (2017) Individualized 3D printing navigation template for pedicle screw fixation in upper cervical spine. PLoS One 12:e0171509. https://doi.org/10.1371/journal.pone.0171509
67. Choonara YE, du Toit LC, Kumar P, Kondiah PPD, Pillay V (2016) 3D-printing and the effect on medical costs: a new era? Expert Rev Pharmacoecon Outcomes Res 16:23–32. https://doi.org/10.1586/14737167.2016.1138860
68. Marro A, Bandukwala T, Mak W (2016) Three-Dimensional Printing and Medical Imaging: A Review of the Methods and Applications. Curr Probl Diagn Radiol 45:2–9. https://doi.org/10.1067/j.cpradiol.2015.07.009
69. Weller C, Kleer R, Piller FT (2015) Economic implications of 3D printing: Market structure models in light of additive manufacturing revisited. Int J Prod Econ 164:43–56. https://doi.org/10.1016/J.IJPE.2015.02.020
70. Sheha ED, Gandhi SD, Colman MW (2019) 3D printing in spine surgery. Ann Transl Med 0: https://doi.org/10.21037/29090
71. Castro-Mateos I, Pozo JM, Lazary A, Frangi A (2015) 3D Vertebra segmentation by feature selection active shape model. In: Recent advances in computational methods and clinical applications for spine imaging. Springer, pp 241–245
72. Rijsbergen M van, van Rietbergen B, Barthelemy V, Eltes P, Lazáry Á, Lacroix D, Noailly J, Ho Ba Tho M-C, Wilson W, Ito K (2018) Comparison of patient-specific computational models vs. clinical follow-up, for adjacent segment disc degeneration and bone remodelling after spinal fusion. PLoS One 13:e0200899. https://doi.org/10.1371/journal.pone.0200899
73. Aryanto KYE, Oudkerk M, van Ooijen PMA (2015) Free DICOM de-identification tools in clinical research: functioning and safety of patient privacy. Eur Radiol 25:3685–95. https://doi.org/10.1007/s00330-015-3794-0
74. Bozic KJ, Keyak JH, Skinner HB, Bueff HU, Bradford DS (1994) Three-dimensional finite element modeling of a cervical vertebra: an investigation of burst fracture mechanism. J Spinal Disord 7:102–110
75. Lim PH, Bagci U, Bai L, Huang J, Jian F, Wu H, Li H, Frounchi K, Briand LC, Grady L, Labiche Y, Subramanyan R, Egger J, Kapur T, Fedorov A, Pieper S, Miller J V.,

Veeraraghavan H, Freisleben B, et al (2013) Statistical Validation of Image Segmentation Quality Based on a Spatial Overlap Index. Sci Rep 3:1–7. https://doi.org/10.1016/S1076-6332(03)00671-8

76. Bharatha A, Hirose M, Hata N, Warfield SK, Ferrant M, Zou KH, Suarez-Santana E, Ruiz-Alzola J, D'Amico A, Cormack RA, Kikinis R, Jolesz FA, Tempany CMC (2001) Evaluation of three-dimensional finite element-based deformable registration of pre- and intraoperative prostate imaging. Med Phys 28:2551–2560. https://doi.org/10.1118/1.1414009
77. Cignoni P, Callieri M, Corsini M, Dellepiane M, Ganovelli F, Ranzuglia G (2008) Meshlab: an open-source mesh processing tool. In: Eurographics Italian chapter conference. pp 129–136
78. Cignoni P, Rocchini C, Scopigno R (1998) Metro: Measuring Error on Simplified Surfaces. Comput Graph Forum 17:167–174. https://doi.org/10.1111/1467-8659.00236
79. Aebi M, Gunzburg R (2011) OOT: The Open Operating Theatre. Eur Spine J 20:825–825. https://doi.org/10.1007/s00586-011-1832-4
80. Varga PP, Lazary A (2010) Chordoma of the sacrum: "en bloc" total sacrectomy and lumbopelvic reconstruction. Eur Spine J 19:1039–1040. https://doi.org/10.1007/s00586-010-1460-4
81. Kikinis R, Pieper SD, Vosburgh KG (2014) 3D Slicer: A Platform for Subject-Specific Image Analysis, Visualization, and Clinical Support. In: Intraoperative Imaging and Image-Guided Therapy. Springer New York, New York, NY, pp 277–289
82. Couteau B, Hobatho M-C, Darmana R, Brignola J-C, Arlaud J-Y (1998) Finite element modelling of the vibrational behaviour of the human femur using CT-based individualized geometrical and material properties. J Biomech 31:383–386
83. Rho J-Y, Hobatho MC, Ashman RB (1995) Relations of mechanical properties to density and CT numbers in human bone. Med Eng Phys 17:347–355
84. Charriere E, Sirey F, Zysset PK (2003) A finite element model of the L5-S1 functional spinal unit: development and comparison with biomechanical tests in vitro. Comput Methods Biomech Biomed Eng 6:249–261
85. Kopperdahl DL, Morgan EF, Keaveny TM (2002) Quantitative computed tomography estimates of the mechanical properties of human vertebral trabecular bone. J Orthop Res 20:801–805
86. Welsch G, Boyer R, Collings EW (1993) Materials properties handbook: titanium alloys. ASM international
87. Webb PA (2000) A review of rapid prototyping (RP) techniques in the medical and biomedical sector. J Med Eng Technol 24:149–153. https://doi.org/10.1080/03091900050163427
88. Matsumoto JS, Morris JM, Foley TA, Williamson EE, Leng S, McGee KP, Kuhlmann JL, Nesberg LE, Vrtiska TJ (2015) Three-dimensional Physical Modeling: Applications and Experience at Mayo Clinic. RadioGraphics 35:1989–2006. https://doi.org/10.1148/rg.2015140260
89. Holly LT, Foley KT (2003) Intraoperative Spinal Navigation. Spine (Phila Pa 1976) 28:S54–S61. https://doi.org/10.1097/01.BRS.0000076899.78522.D9
90. Gibson I, Rosen DW, Stucker B (2014) Additive manufacturing technologies.

Springer
91. Yao J, Burns JE, Forsberg D, Seitel A, Rasoulian A, Abolmaesumi P, Hammernik K, Urschler M, Ibragimov B, Korez R, Vrtovec T, Castro-Mateos I, Pozo JM, Frangi AF, Summers RM, Li S (2016) A multi-center milestone study of clinical vertebral CT segmentation. Comput Med Imaging Graph 49:16–28. https://doi.org/10.1016/j.compmedimag.2015.12.006
92. Hayashi T, Chen H, Miyamoto K, Zhou X, Hara T, Yokoyama R, Kanematsu M, Hoshi H, Fujita H (2011) A computerized scheme for localization of vertebral bodies on body CT scans. In: Medical Imaging 2011: Image Processing. International Society for Optics and Photonics, p 796238
93. Evans JD (1996) Straightforward statistics for the behavioral sciences. Thomson Brooks/Cole Publishing Co
94. Koo TK, Li MY (2016) A Guideline of Selecting and Reporting Intraclass Correlation Coefficients for Reliability Research. J Chiropr Med 15:155–63. https://doi.org/10.1016/j.jcm.2016.02.012
95. van Eijnatten M, van Dijk R, Dobbe J, Streekstra G, Koivisto J, Wolff J (2018) CT image segmentation methods for bone used in medical additive manufacturing. Med Eng Phys 51:6–16. https://doi.org/10.1016/J.MEDENGPHY.2017.10.008
96. George E, Liacouras P, Rybicki FJ, Mitsouras D (2017) Measuring and Establishing the Accuracy and Reproducibility of 3D Printed Medical Models. RadioGraphics 37:1424–1450. https://doi.org/10.1148/rg.2017160165
97. Lang G, Perrech M, Navarro-Ramirez R, Hussain I, Pennicooke B, Maryam F, Avila MJ, Härtl R (2017) Potential and Limitations of Neural Decompression in Extreme Lateral Interbody Fusion—A Systematic Review. World Neurosurg 101:99–113. https://doi.org/10.1016/J.WNEU.2017.01.080
98. Navarro-Ramirez R, Berlin C, Lang G, Hussain I, Janssen I, Sloan S, Askin G, Avila MJ, Zubkov M, Härtl R (2018) A New Volumetric Radiologic Method to Assess Indirect Decompression After Extreme Lateral Interbody Fusion Using High-Resolution Intraoperative Computed Tomography. World Neurosurg 109:59–67. https://doi.org/10.1016/J.WNEU.2017.07.155
99. Sato J, Ohtori S, Orita S, Yamauchi K, Eguchi Y, Ochiai N, Kuniyoshi K, Aoki Y, Nakamura J, Miyagi M, Suzuki M, Kubota G, Inage K, Sainoh T, Fujimoto K, Shiga Y, Abe K, Kanamoto H, Inoue G, et al (2017) Radiographic evaluation of indirect decompression of mini-open anterior retroperitoneal lumbar interbody fusion: oblique lateral interbody fusion for degenerated lumbar spondylolisthesis. Eur Spine J 26:671–678. https://doi.org/10.1007/s00586-015-4170-0
100. Ostelo RWJG, Deyo RA, Stratford P, Waddell G, Croft P, Von Korff M, Bouter LM, de Vet HC (2008) Interpreting change scores for pain and functional status in low back pain: towards international consensus regarding minimal important change. Spine (Phila Pa 1976) 33:90–4. https://doi.org/10.1097/BRS.0b013e31815e3a10
101. Smith JA, Tuchman A, Huoh M, Kaiser AM, Schooler WG, Hsieh PC (2014) Locomotor biomechanics after total sacrectomy: a case report. Spine (Phila Pa 1976) 39:E1481–E1487
102. Clark AJ, Tang JA, Leasure JM, Ivan ME, Kondrashov D, Buckley JM, Deviren V, Ames CP (2014) Gait-simulating fatigue loading analysis and sagittal alignment

failure of spinal pelvic reconstruction after total sacrectomy: comparison of 3 techniques. J Neurosurg Spine 20:364–370
103. Frost HM (1998) From Wolff's law to the mechanostat: a new "face" of physiology. J Orthop Sci 3:282–286
104. Frost HM (2000) The Utah paradigm of skeletal physiology: an overview of its insights for bone, cartilage and collagenous tissue organs. J Bone Miner Metab 18:305–316
105. Perren SM (2002) Evolution of the internal fixation of long bone fractures: the scientific basis of biological internal fixation: choosing a new balance between stability and biology. J Bone Joint Surg Br 84:1093–1110
106. Bottlang M, Doornink J, Lujan TJ, Fitzpatrick DC, Marsh JL, Augat P, von Rechenberg B, Lesser M, Madey SM (2010) AAOS Supplement Selected Scientific Exhibits: Effects of Construct Stiffness on Healing of Fractures Stabilized with Locking Plates. J Bone Jt Surgery Am Vol 92:12
107. Potter BK (2016) From Bench to Bedside: How stiff is too stiff? Far-cortical locking or dynamic locked plating may obviate the question. Clin Orthop Relat Res 474:1571–1573
108. Henderson CE, Lujan TJ, Kuhl LL, Bottlang M, Fitzpatrick DC, Marsh JL (2011) 2010 mid-America Orthopaedic Association Physician in Training Award: healing complications are common after locked plating for distal femur fractures. Clin Orthop Relat Res 469:1757–1765
109. Holzman MA, Hanus BD, Munz JW, O'Connor DP, Brinker MR (2016) Addition of a medial locking plate to an in situ lateral locking plate results in healing of distal femoral nonunions. Clin Orthop Relat Res 474:1498–1505
110. Rodriguez EK, Zurakowski D, Herder L, Hall A, Walley KC, Weaver MJ, Appleton PT, Vrahas M (2016) Mechanical construct characteristics predisposing to non-union after locked lateral plating of distal femur fractures. J Orthop Trauma 30:403–408
111. Yoshihara H (2013) Rods in spinal surgery: a review of the literature. Spine J 13:1350–1358
112. Craven TG, Carson WL, Asher MA, Robinson RG (1994) The effects of implant stiffness on the bypassed bone mineral density and facet fusion stiffness of the canine spine. Spine (Phila Pa 1976) 19:1664–1673
113. Benzel EC (2012) Spine Surgery 2-Vol Set E-Book: Techniques, Complication Avoidance, and Management (Expert Consult-Online). Elsevier Health Sciences
114. Le Navéaux F, Aubin C-E, Parent S, Newton PO, Labelle H (2017) 3D rod shape changes in adolescent idiopathic scoliosis instrumentation: how much does it impact correction? Eur Spine J 26:1676–1683
115. Cidambi KR, Glaser DA, Bastrom TP, Nunn TN, Ono T, Newton PO (2012) Postoperative changes in spinal rod contour in adolescent idiopathic scoliosis: an in vivo deformation study. Spine (Phila Pa 1976) 37:1566–1572
116. Huang S, Ji T, Guo W (2019) Biomechanical comparison of a 3D-printed sacrum prosthesis versus rod-screw systems for reconstruction after total sacrectomy: A finite element analysis. Clin Biomech 70:203–208
117. Viceconti M, Henney A, Morley-Fletcher E (2016) In silico clinical trials: how computer simulation will transform the biomedical industry. Int J Clin Trials 3:37.

https://doi.org/10.18203/2349-3259.ijct20161408
118. Evangelisti G, Fiore MR, Bandiera S, Brodano GB, Terzi S, Girolami M, Pipola V, Righi A, Nanni C, Fanti S (2019) Carbon ions therapy as single treatment in chordoma of the sacrum. Histologic and metabolic outcome studies. Eur Rev Med Pharmacol Sci 23:4002–4009
119. Magnaghi P, Salom B, Cozzi L, Amboldi N, Ballinari D, Tamborini E, Gasparri F, Montagnoli A, Raddrizzani L, Somaschini A (2018) Afatinib is a new therapeutic approach in chordoma with a unique ability to target EGFR and brachyury. Mol Cancer Ther 17:603–613
120. Zheng Y, Yu D, Zhao J, Wu Y, Zheng B (2016) 3D Printout Models vs. 3D-Rendered Images: Which Is Better for Preoperative Planning? J Surg Educ 73:518–523. https://doi.org/10.1016/J.JSURG.2016.01.003
121. Kadoury S, Labelle H, Paragios N (2011) Automatic inference of articulated spine models in CT images using high-order Markov Random Fields. Med Image Anal 15:426–437. https://doi.org/10.1016/J.MEDIA.2011.01.006
122. Radermacher K, Portheine F, Anton M, Zimolong A, Kaspers G, Rau G, Staudte H-W (1998) Computer assisted orthopaedic surgery with image based individual templates. Clin Orthop Relat Res 354:28–38
123. Birnbaum K, Schkommodau E, Decker N, Prescher A, Klapper U, Radermacher K (2001) Computer-assisted orthopedic surgery with individual templates and comparison to conventional operation method. Spine (Phila Pa 1976) 26:365–370
124. Shao Z-X, Wang J-S, Lin Z-K, Ni W-F, Wang X-Y, Wu A-M (2017) Improving the trajectory of transpedicular transdiscal lumbar screw fixation with a computer-assisted 3D-printed custom drill guide. PeerJ 5:e3564. https://doi.org/10.7717/peerj.3564
125. Sugawara T, Kaneyama S, Higashiyama N, Tamura S, Endo T, Takabatake M, Sumi M (2018) Prospective Multicenter Study of a Multistep Screw Insertion Technique Using Patient-Specific Screw Guide Templates for the Cervical and Thoracic Spine. Spine (Phila Pa 1976) 43:1685–1694. https://doi.org/10.1097/BRS.0000000000002810
126. Fan Y, Du J, Zhang J, Liu S, Xue X, Huang Y, Zhang J, Hao D (2017) Comparison of accuracy of pedicle screw insertion among 4 guided technologies in spine surgery. Med Sci Monit Int Med J Exp Clin Res 23:5960
127. Van den Abbeele M, Valiadis J-M, Lima LVPC, Khalifé P, Rouch P, Skalli W (2018) Contribution to FE modeling for intraoperative pedicle screw strength prediction. Comput Methods Biomech Biomed Engin 21:13–21
128. Von Strempel A, Trenkmann S, Krönauer I, Kirsch L, Sukopp C (1998) The stability of bone screws in the os sacrum. Eur Spine J 7:313–320
129. Zhu Q, Lu WW, Holmes AD, Zheng Y, Zhong S, Leong JCY (2000) The effects of cyclic loading on pull-out strength of sacral screw fixation: an in vitro biomechanical study. Spine (Phila Pa 1976) 25:1065–1069
130. Kato M, Taneichi H, Suda K (2015) Advantage of Pedicle Screw Placement Into the Sacral Promontory (Tricortical Purchase) on Lumbosacral Fixation. J Spinal Disord Tech 28:E336–E342. https://doi.org/10.1097/BSD.0b013e31828ffc70
131. Sabry FF, Xu R, Nadim Y, Ebraheim NA (2001) Bone Density of the First Sacral Vertebra in Relation to Sacral Screw Placement: A Computed Tomography Study.

Orthopedics 24:475–477. https://doi.org/10.3928/0147-7447-20010501-15
132. Misch CE (2004) Dental Implant Prosthetics-E-Book. Elsevier Health Sciences
133. Bhaskaran E, Azhagarasan NS, Miglani S, Ilango T, Krishna GP, Gajapathi B (2013) Comparative evaluation of marginal and internal gap of Co–Cr copings fabricated from conventional wax pattern, 3D printed resin pattern and DMLS tech: an in vitro study. J Indian Prosthodont Soc 13:189–195
134. Wang D, Wang Y, Wang J, Song C, Yang Y, Zhang Z, Lin H, Zhen Y, Liao S (2016) Design and fabrication of a precision template for spine surgery using selective laser melting (SLM). Materials (Basel) 9:608
135. Sallent A, Ramírez M, Catalá J, Rodríguez-Baeza A, Bagó J, de Albert M, Vélez R (2019) precision and safety of Multilevel cervical transpedicular Screw Fixation with 3D Patient-Specific Guides; A cadaveric Study. Sci Rep 9:1–7
136. Eltes PE, Kiss L, Bartos M, Gyorgy ZM, Csakany T, Bereczki F, Lesko V, Puhl M, Varga PP, Lazary A (2020) Geometrical accuracy evaluation of an affordable 3D printing technology for spine physical models. J Clin Neurosci
137. Gertzbein SD, Robbins SE (1990) Accuracy of pedicular screw placement in vivo. Spine (Phila Pa 1976) 15:11–14
138. Fisher CG, Schouten R, Versteeg AL, Boriani S, Varga PP, Rhines LD, Kawahara N, Fourney D, Weir L, Reynolds JJ, Sahgal A, Fehlings MG, Gokaslan ZL (2014) Reliability of the Spinal Instability Neoplastic Score (SINS) among radiation oncologists: an assessment of instability secondary to spinal metastases. Radiat Oncol 9:69. https://doi.org/10.1186/1748-717X-9-69
139. Versteeg AL, Verlaan J-J, Sahgal A, Mendel E, Quraishi NA, Fourney DR, Fisher CG (2016) The Spinal Instability Neoplastic Score. Spine (Phila Pa 1976) 41:S231–S237. https://doi.org/10.1097/BRS.0000000000001822
140. Costa MC, Eltes P, Lazary A, Varga PP, Viceconti M, Dall'Ara E (2019) Biomechanical assessment of vertebrae with lytic metastases with subject-specific finite element models. J Mech Behav Biomed Mater 98:268–290. https://doi.org/10.1016/J.JMBBM.2019.06.027

10. LIST OF OWN PUBLICATIONS

11.1. Publications that formed the basis of the dissertation:

1. **Eltes, P. E**., Kiss, L., Bartos, M., Eösze, Z., Szövérfi, Z., Varga, P. P., & Lazáry, Á. (2019). Attitude of spine surgeons towards the application of 3D technologies-a survey of AOSpine members. *Ideggyogyaszati szemle*, *72*(7-8), 227-235.
2. Costa, M. C., **Eltes, P**., Lazary, A., Varga, P. P., Viceconti, M., & Dall'Ara, E. (2019). Biomechanical assessment of vertebrae with lytic metastases with subject-specific finite element models. *Journal of the mechanical behavior of biomedical materials*, *98*, 268-290.
3. **P. E. Eltes**, Kiss, L., Bartos, M., Gyorgy, Z. M., Csakany, T., Bereczki, F., ... & Lazary, A. (2020). Geometrical accuracy evaluation of an affordable 3D printing technology for spine physical models. Journal of Clinical Neuroscience, 72, 438-446.

11.2 Publication in the field of In Silico Medicine/ Musculoskeletal modelling as co author

1. van Rijsbergen, M., van Rietbergen, B., Barthelemy, V., **Eltes, P**., Lazáry, Á., Lacroix, D., Noailly J, Ho Ba Tho MC., Wilson W., Ito, K. (2018). Comparison of patient-specific computational models vs. clinical follow-up, for adjacent segment disc degeneration and bone remodelling after spinal fusion. *PloS one*, *13*(8), e0200899.

2. Dao, T. T., Pouletaut, P., Charleux, F., Lazáry, Á., **Eltes, P**., Varga, P. P., & Tho, M. C. H. B. (2015). Multimodal medical imaging (CT and dynamic MRI) data and computer-graphics multi-physical model for the estimation of patient specific lumbar spine muscle forces. *Data & Knowledge Engineering*, *96*, 3-18.

3. Castro-Mateos, I., Pozo, J. M., **Eltes, P. E**., Del Rio, L., Lazary, A., & Frangi, A. F. (2014). 3D segmentation of annulus fibrosus and nucleus pulposus from T2-weighted magnetic resonance images. *Physics in Medicine & Biology*, *59*(24), 7847.

11.2.1. Book chapter

1. Dao, T. T., Pouletaut, P., Charleux, F., Lazáry, Á., **Eltes, P**., Varga, P. P., & Tho, M. C. H. B. (2014). Estimation of patient specific lumbar spine muscle forces using multi-physical musculoskeletal model and dynamic MRI. In *Knowledge and Systems Engineering* (pp. 411-422). Springer, Cham.

11.3. Publication in the field of spine surgery as co author

1. Kiss, L., Varga, P. P., Szoverfi, Z., Jakab, G., **Eltes, P. E**., & Lazary, A. (2019). Indirect foraminal decompression and improvement in the lumbar alignment after percutaneous cement discoplasty. *European Spine Journal*, 1-7.

2. Klemencsics, I., Lazary, A., Szoverfi, Z., Bozsodi, A., **Eltes, P**., & Varga, P. P. (2016). Risk factors for surgical site infection in elective routine degenerative lumbar surgeries. *The Spine Journal*, *16*(11), 1377-1383.

3. Klemencsics, I., Lazary, A., Valasek, T., Szoverfi, Z., Bozsodi, A., **Eltes, P**., ... & Varga, P. P. (2016). Cross-cultural adaptation and validation of the Hungarian version of the Core Outcome Measures Index for the back (COMI Back). *European Spine Journal*, *25*(1), 257-264.

4. Valasek, T., Varga, P. P., Klemencsics, I., Szövérfi, Z., Bozsódi, Á., **Éltes, P. E**., & Lazáry, Á. (2015). Measuring the functional impairment of the lumbar spine. *Ideggyogyaszati szemle*, *68*(3-4), 135-141.

5. Szövérfi, Z., Lazary, A., Bozsódi, Á., Klemencsics, I., **Éltes, P. E**., & Varga, P. P. (2014). Primary Spinal Tumor Mortality Score (PSTMS): a novel scoring system for predicting poor survival. *The Spine Journal*, *14*(11), 2691-2700.

DOI:10.14753/SE.2020.2439

11. ACKNOWLEDGMENTS

I would like to thank my supervisor, Dr. Áron Lazáry for the opportunity to study and work in such a stimulating, persevering environment such as the National Center for Spinal Disorders, R&D department. I would like to thank my supervisor for allowing me the space and freedom I needed to work and for continued support and guidance from day one.

I would like to thank for Dr. Péter Pál Varga for his patient guidance, motivation and encouragement over the years. I am indebted to Prof. Dr. Damien Lacroix from the University of Sheffield, Insigneo Institute for In Silico Medicine who not only introduced me to the beauty of In Silico Medicine over the MySpine project, but also gave advice and support for my projects.

I express my gratitude to Máte Turbucz, Benjámin Hajnal, Ágoston Pokorni, Bereczki Ferenc, Kiss László, Jannifer Fayad from the In Silico Biomechanics Laboratory for their constant support, inspiring discussions and for the pleasant working atmosphere.

I am grateful for all former and current members of the National Center for Spinal Disorders, R&D department; Julia Szita, Dr. István Klemencsics, Dr. Zsolt Szővérfi.

I would like to acknowledge my spine surgeon colleagues from the National Center for Spinal Disorders for their assistance and patience; Dr. Balázs Szöllősi, Dr. Bánk András, Dr. Zoltán Magor György, Dr. Miklós Agócs, Dr. István Tóth, Dr. Gábor Jakab.

I would also like to thank to my previous supervisors during my undergraduate years: Prof. Dr. Edit Gogolák, Prof. Dr. Lőrinczi Zoltán from University of Medicine and Pharmacy Tirgu Mures, for introducing me to the beautiful field of musculoskeletal anatomy and biomechanics.

Last but not least I am grateful to my friends, family and my wife, Tímea for their patience, understanding and support throughout the years, and I would like to dedicate this work to Tímea, the only person who really knows how much fight, frustration, motivation, desperation, laughs, anger, happiness, and fulfilment is behind every phrase of the presented thesis.